universe

MDPI

Article

A Catalog of 73 B-Type Stars and Their Brightness Variation from K2 Campaign 13–18

Bergerson V. H. V. da Silva [1,†,‡], Jéssica M. Eidam [2,‡], Alan W. Pereira [1,‡], M. Cristina Rabello-Soares [3,‡], Eduardo Janot-Pacheco [4,‡], Laerte Andrade [5,‡] and Marcelo Emilio [1,2,*,‡]

[1] Department of Geosciences, State University of Ponta Grossa, Ponta Grossa 84030-900, PR, Brazil; bvhvsilva@uem.br (B.V.H.V.d.S.); alan.pereira@uepg.br (A.W.P.)
[2] National Observatory, MCTI, Rio de Janeiro 20921-400, RJ, Brazil; jessyeidam@gmail.com
[3] W. W. Hansen Experimental Physics Laboratory, Stanford University, Stanford, CA 94305, USA; cristina.rabello.soares@stanford.edu
[4] Institute of Astronomy, Geophysics and Atmospheric Sciences, University of São Paulo, São Paulo 05509-090, SP, Brazil; eduardo.janot@iag.usp.br
[5] National Laboratory for Astrophysics, Rua Estados Unidos 154, Itajubá 37504-364, MG, Brazil; landrade@lna.br
* Correspondence: memilio@uepg.br
† Current address: Departament of Physics, State University of Maringá, Maringá 87020-900, PR, Brazil.
‡ These authors contributed equally to this work.

Abstract

The variability of B-type stars offers valuable insights into the interiors of stars and the processes that drive pulsation and rotation in massive stars. In this study, we present the classification of the variability of 197 B-type stars observed in various *Kepler*/K2 campaigns, including 73 newly classified stars from Campaigns 13–18. For these stars, we derived atmospheric and evolutionary parameters using space-based photometry and ground-based spectroscopy. We obtained spectroscopic data for 34 targets with high-resolution instruments at OPD/LNA, which were supplemented by archival LAMOST spectra. After correcting for instrumental systematics, we analyzed the light curves using Fourier transforms and wavelet decomposition to identify both periodic and stochastic signals. The identified variability types included SPB stars, β Cephei/SPB hybrids, fast-rotating pulsators, stochastic low-frequency variables, eclipsing binaries, and rotational variables. We also revised classifications of misidentified stars using *Gaia* astrometry, confirming the main-sequence nature of objects once considered subdwarfs. Our results indicate that hot-star variability exists along a continuum shaped by mass, rotation, and internal mixing rather than distinct instability domains. This study enhances our understanding of B-type star variability and supports future asteroseismic modeling with missions like *PLATO*.

Keywords: B-type stars; space-based photometry; spectroscopic analysis; stellar variability

check for updates

Academic Editor: Vikram Dwarkadas

Received: 30 June 2025
Revised: 18 August 2025
Accepted: 28 August 2025
Published: 3 September 2025

Citation: Silva, B.V.H.V.d.; Eidam, J.M.; Pereira, A.W.; Rabello-Soares, M.C.; Janot-Pacheco, E.; Andrade, L.; Emilio, M. A Catalog of 73 B-Type Stars and Their Brightness Variation from K2 Campaign 13–18. *Universe* **2025**, *11*, 301. https://doi.org/10.3390/universe11090301

Copyright: © 2025 by the authors. Licensee MDPI, Basel, Switzerland. This article is an open access article distributed under the terms and conditions of the Creative Commons Attribution (CC BY) license (https://creativecommons.org/licenses/by/4.0/).

1. Introduction

Understanding the evolution of massive stars is fundamental to several fields in astrophysics, including the chemical enrichment of galaxies, the formation and evolution of stellar clusters, supernova mechanisms, and the origin of compact object populations [1]. Despite continuous theoretical and observational progress, the evolutionary paths of these stars remain challenging to model due to the interplay of factors such as metallicity, rotation, binarity, magnetic fields, and mass loss (e.g., [2]). Among these massive stars,

Slowly Pulsating B-type (SPB) stars are of particular interest because they exhibit high-order gravity-mode pulsations. These modes are uniquely sensitive to near-core physical processes such as internal rotation, mixing, and chemical gradients, making SPB stars powerful probes of the deep stellar interior and valuable benchmarks for testing stellar evolution models.

Over the past decades, advances in space-based photometry have significantly improved our understanding of stellar interiors. Missions such as MOST [3], CoRoT [4], *Kepler* [5], *Kepler*/K2 [6], and *TESS* [7] have delivered long-duration, high-precision time-series data, allowing asteroseismology to become a key tool for probing the internal structure and evolutionary stages of stars. This technique has revolutionized our ability to infer fundamental stellar parameters such as mass, radius, age, and internal rotation.

In this context, B-type stars, slowly pulsating B stars (SPB) in particular and their more massive counterparts, the β Cephei variables, have emerged as prime targets for asteroseismic studies (see [8] and the references therein). These stars exhibit rich frequency spectra dominated by non-radial pulsations, providing insights into core mixing, angular momentum transport, and envelope dynamics. The combination of space photometry with spectroscopic and astrometric data has enabled a detailed classification of the variability among B stars, refining theoretical models and improving the empirical mapping of the instability strip.

Following the failure of the second reaction wheel in 2013, the *Kepler* spacecraft transitioned into the K2 mission, which observed fields along the ecliptic plane using a new pointing strategy based on solar radiation pressure and thruster corrections [6]. Despite their shorter duration and increased sensitivity to systematics, K2 campaigns provided access to a wider variety of stellar populations by targeting diverse galactic environments.

Our research group has previously employed *CoRoT* and K2 data to investigate hot-star variability (e.g., [9–11]). Building on our previous study of 122 B-type stars in K2 Campaign 11 [12], this paper presents the variability classification for additional stars from Campaigns 13–18, thereby expanding our sample for statistical study. We also include new spectroscopic analysis to derive atmospheric and evolutionary properties. These results contribute to a broader view of the variability landscape among B-type stars, add to the empirical basis for pulsation studies, and provide complementary data that may be useful for future comparative work across different galactic environments.

This paper is organized as follows. Section 2 describes the sample selection, photometric and astrometric data from the *Kepler* and *Gaia* missions, and spectroscopic follow-up. Section 3 details the light curve processing and frequency analysis. Section 4 presents the spectroscopic data reduction and atmospheric modeling in our study. Section 5 outlines the variability classification criteria. Section 6 discusses the main findings, and Section 7 highlights the implications for stellar evolution theory.

2. Sample Selection and Data Collection

2.1. Sample Selection

Following our earlier K2 studies [11,12], we proposed additional observations of B-star candidates during the later stages of the mission (Campaigns 13–18). Our strategy prioritized stars bright enough to permit meaningful ground-based follow-up while maximizing the number of targets within the spacecraft's limited pixel and memory budgets. Unlike modern surveys, such as *TESS*, which provide full-frame images with a regular cadence, *Kepler* could only downlink data from pre-selected pixel masks, especially for bright stars, because they consumed a large portion of the available resources.

Campaign 11, which targeted dense stellar fields toward the Galactic center, allowed observations of more than one hundred B stars. Campaign 13, by contrast, pointed near the

Galactic anti-center at the intersection with the ecliptic plane, yielding an initial list of 68 B-star candidates. The subsequent campaigns sampled fields farther from the Galactic plane, spanning sparser regions between the constellations of Scorpius and Cancer. Accordingly, fewer targets satisfied our original brightness and classification criteria.

Given this limitation, we adopted less restrictive selection criteria for Campaigns 14 through 18. The revised criteria allowed the inclusion of stars within the B-type temperature range that had uncertain or poorly established classifications, such as hot subdwarf candidates and other faint objects. While some Be stars were observed during Campaigns 13–18, we chose to exclude them from this work and treat their complex photometric and spectral variability in a dedicated future study. Therefore, the 73 stars presented in this paper do not appear as Be stars in the literature. Furthermore, our analysis of the available spectra for 55 of these targets shows no evidence of Hydrogen line emission, indicating the absence of a circumstellar disk at the time of observation.

All stars analyzed in this study are listed in Table A1 (Appendix A), and they are identified by their EPIC ID, SIMBAD identifier, sky coordinates, apparent magnitude, and spectral type. The subset for which spectroscopic follow-up was obtained (see Section 6) reflects a combination of factors, including visual brightness, observability from our primary site (see Section 2.4), telescope availability, and weather conditions.

2.2. Kepler/K2 Photometric Observations

The data were collected using a single wide-bandpass filter (420–900 nm) and primarily in long-cadence mode (∼30 min exposures), with a smaller subset of targets in short-cadence mode (∼1 min exposures). The B-type stars in our sample were observed in K2 Campaigns 13 and 15–18 under Guest Observer programs GO13127, GO15099, GO16099, GO17012, and GO18012 (Principal Investigator: Marcelo Emilio). Campaign 13 (March–May 2017) targeted a region near the Hyades and Taurus constellations; Campaign 15 (August–November 2017) observed a field in Scorpius; Campaigns 16 (December 2017–February 2018) and 18 (May–July 2018) both covered a region in Cancer containing the open clusters M44 and M67; and Campaign 17 (March–May 2018) focused on Virgo. No targets were proposed for Campaign 14 because its field of view near the North Galactic Cap has a low density of bright B-type stars, which limits the feasibility of variability studies.

The publicly available light curves used in this work have been processed through the K2 pipeline, which aims to remove these instrumental trends, resulting in Pre-search Data Conditioning (PDC) light curves. All observation times are provided according to Barycentric Julian Date (BJD), which accounts for the spacecraft's motion relative to the solar system's barycenter.

Several campaigns encountered specific anomalies that required careful consideration. During Campaign 13, the bright star Aldebaran ($V \approx 0.85$) caused significant saturation on CCD channel 73 and adjacent parts of channel 74, leading to residual instrumental errors in the light curves of nearby targets. In Campaign 15, a series of powerful solar flares and coronal mass ejections between September 6 and 10, 2017, caused a noticeable increase in the dark current across all CCD channels. Campaign 16 was affected by the Earth passing through the field of view, while Campaign 17 experienced scattered light from the bright star Spica ($V \approx 0.97$). While most of our targets were not located in the most severely affected CCD regions, we accounted for these events in our analysis to ensure the robustness of the resulting photometric interpretations.

2.3. Gaia Data

In Figure 1, we present the color–absolute-magnitude diagram (caMD) for our K2 sample, which was derived from data in Data Release 3 (DR3) of the *Gaia* mission [13,14].

The G-band absolute magnitude was computed using the standard distance modulus defined as follows:

$$M_G = G + 5 - 5\log_{10} r - A_G,$$

where G is the apparent G-band magnitude, r is the photogeometric distance, and A_G is the extinction in the G band. Distances were taken from [15], which provides Bayesian estimates based on *Gaia EDR3* parallaxes and photometry.

To determine extinction, we used 3D reddening maps accessed via the GALExtin service [16], employing the coordinates, distance, and associated uncertainties for each target. For most targets, extinction values were obtained from the map provided by [17]. For stars not covered in that dataset, we used the map by [18], applying the authors' coefficients to convert Pan-STARRS1-based extinction to the *Gaia* photometric system. In a few remaining cases, we adopted the A_G values directly from *Gaia DR2*.

In Figure 1, colored symbols denote the variability types described in Section 5. For reference, the background shows a density plot of 200,000 stars observed by both *Gaia* and *Kepler*, which outlines the positions of the main sequence and the red clump. We also include evolution tracks from the `MIST`, along with the position of the Sun [19].

The location of most targets is consistent with spectral types ranging from B to A and luminosity classes I through V. This astrometric analysis was crucial for confirming the evolutionary status of our sample and refining the selection criteria. Three hot subdwarf candidates are located in the lower-left region of the diagram, consistent with the subdwarf sequence, and are denoted by black dots. These objects fall outside the scope of this study, which is focused on main-sequence B-type stars, and were excluded from further analysis. Interestingly, two additional objects previously flagged as hot subdwarfs were revealed to lie within the main-sequence band. As discussed in Section 5.1, our photometric analysis indicates that these stars exhibit SPB-type variability.

2.4. Spectroscopic Observations

To determine the fundamental atmospheric properties of our targets, we conducted spectroscopic follow-up observations between March 2017 and June 2021 at the Pico dos Dias Observatory (OPD), operated by the National Laboratory of Astrophysics (LNA) in Brazópolis, Minas Gerais, Brazil. These observations were carried out using the 1.6 m PerkinElmer Ritchey–Chrétien telescope. For most targets, it was equipped with the Cassegrain spectrograph and an Ikon 2048 × 2048 pixel CCD detector, a combination that yielded a spectral resolution of $R \approx 9600$–$12{,}000$ and typical signal-to-noise ratios (S/N) around 100. Additional higher-resolution observations ($R \approx 25,000$) were conducted using the Coudé spectrograph.

We employed two primary wavelength configurations. The first, optimized for atmospheric parameter determination, covered the blue spectral range (3990–5110 Å), including key diagnostic lines of Hydrogen, neutral Helium (He I), and Magnesium (Mg II). Our OPD observations yielded blue-region spectra for 29 targets. The second configuration focused on the red region (6040–6950 Å) to detect Hα emission. Hα spectra were obtained for 45 targets in total (including 28 of the stars also observed in the blue plus 17 others observed only in the red). Wavelength calibration for these setups was performed using Helium–Argon (He–Ar), Neon–Argon (Ne–Ar), and Thorium–Argon (Th–Ar) lamps.

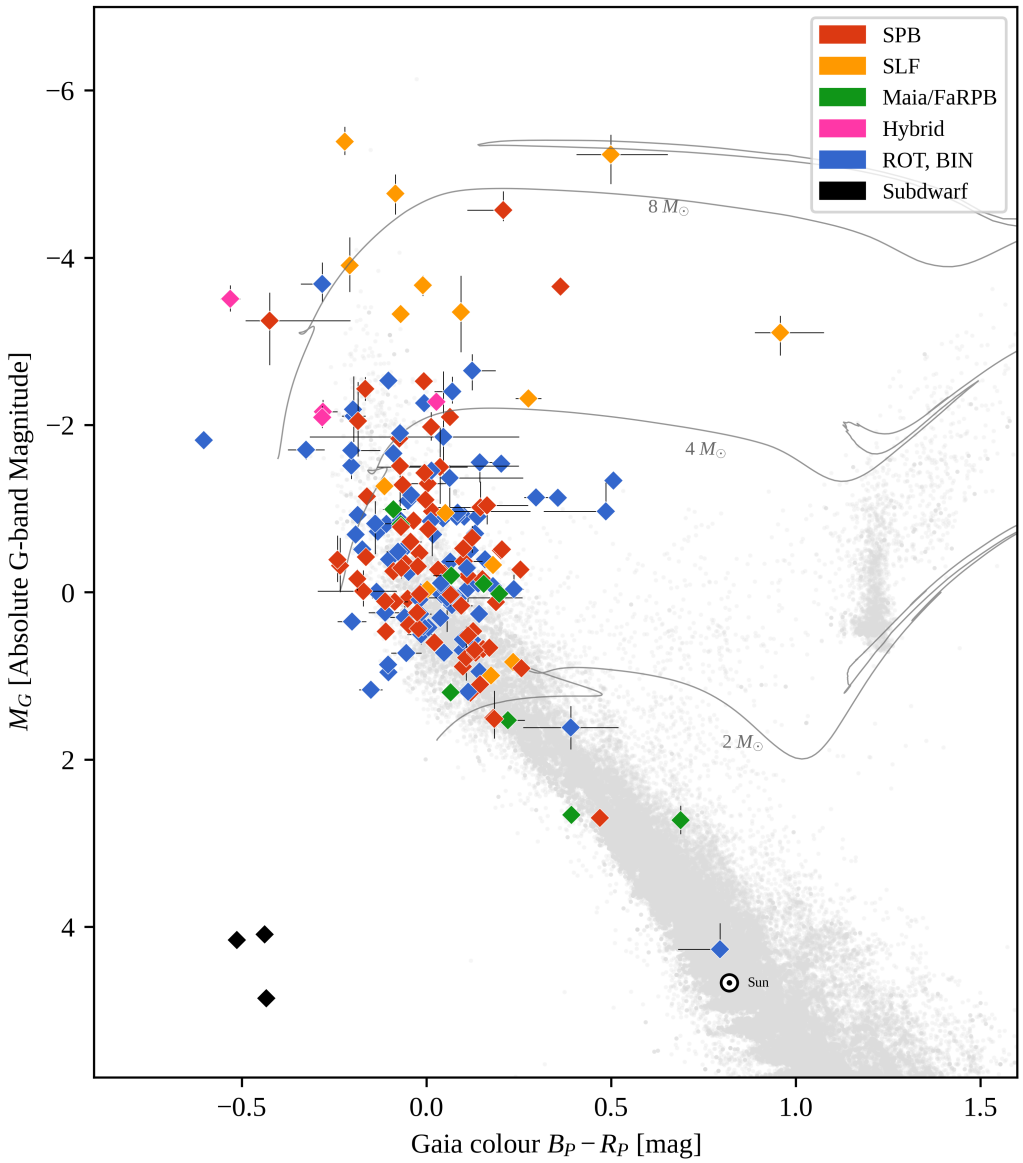


Figure 1. Color–absolute-magnitude diagram (caMD) derived from *Gaia DR3* for OBA stars observed during K2 Campaigns 11–18. Distinct variability types are indicated with different colors, as shown in the legend. Horizontal error bars reflect uncertainties in reddening derived from 3D extinction maps [16], and vertical error bars combine uncertainties in distance [15] and extinction. The background is populated with 200,000 reference stars that define the main sequence and red clump regions, utilizing data from [20]. Evolution tracks from `MIST` are shown for stellar masses of 2, 4, and 8 $M_\odot$, along with the Sun's position [21].

For an additional nine targets where OPD observations were not feasible, we incorporated publicly available spectra from the Large Sky Area Multi-Object Fiber Spectroscopic Telescope (LAMOST, [22]) Data Release 5 (DR5). Although these spectra have a lower resolution ($R \approx 1800$), their broad wavelength coverage (3700–9000 Å) enabled preliminary characterization of those stars and also include Hα. In total, this combination of data provided spectra suitable for atmospheric parameter determination for 34 objects.

3. Light Curves and Frequency Analysis

The raw photometric observations for our targets were processed through the official *Kepler* Science Pipeline (KSP), a sophisticated system designed to convert pixel-level data into calibrated time-series light curves suitable for scientific analysis [23]. Below, we

briefly summarize the key stages of the KSP pipeline, highlighting their role in delivering high-quality photometric time series.

The pipeline begins with the Calibration (CAL) module, which is responsible for fundamental pixel-level corrections. These corrections involve removing electronic bias and dark current and applying flat-fielding to account for pixel-to-pixel sensitivity variations and non-uniform illumination. Given *Kepler*'s shutterless design, this module also corrects for image smear caused by stars drifting across the CCD during readout [24].

Following calibration, the Photometric Analysis (PA) module performs several key tasks. It identifies and removes transient artifacts such as cosmic ray hits and estimates and subtracts the background flux, which may be influenced by scattered light. The core function of the PA module is to perform optimal aperture photometry, determining the ideal set of pixels for each target to maximize the signal-to-noise ratio (S/N). The flux within this optimal aperture is summed to produce the Simple Aperture Photometry (SAP) light curve.

The final stage of the KSP is the Pre-search Data Conditioning (PDC) module. Its goal is to eliminate residual systematics that affect many stars simultaneously, such as those due to thermal fluctuations, pointing drift, or spacecraft events. The PDC-MAP algorithm employs a Bayesian framework to "cotrend" each light curve against a basis of systematic trends derived from neighboring stars, effectively preserving astrophysical signals while removing instrumental noise. The resulting product is the corrected PDC light curve, which serves as the starting point for our analysis [25].

Despite the robustness of the KSP, the K2 mission's unique operating mode introduced dominant systematic effects. Periodic thruster firings conducted every six hours were necessary to maintain pointing stability using solar radiation pressure. These maneuvers introduced a characteristic sawtooth-like signal in the photometry, with a dominant frequency around $\sim$4 d^{-1} and its harmonics. Although the PDC pipeline mitigates this signal, residuals often remain.

To further refine the light curves and suppress K2-specific systematics, we employed the `k2sc` software (version 2.0) package [26]. This tool uses a Gaussian Process model to explicitly decorrelate stellar flux from the spacecraft's position on the CCD, effectively removing roll-angle artifacts while preserving intrinsic stellar variability. For a small number of targets where standard apertures led to contamination from nearby stars, we used the `PyKE` (version 1.1.1) toolset to define custom apertures and re-extract cleaned light curves from the Target Pixel Files (TPFs).

The temporal analysis of the corrected light curves was conducted using the `cleanest` algorithm [27], which is based on the Lomb–Scargle periodogram. This technique fits sinusoidal models using least squares and is well suited for detecting periodic signals in unevenly sampled data.

We identified pulsation frequencies using an iterative prewhitening procedure using tools from the `ivs` Python package (version 3.6) [28]. The highest amplitude frequency is identified in the initial periodogram, and a corresponding sinusoid is fitted to the light curve. This signal is then subtracted, and the process is repeated on the residuals. After each iteration, all identified frequencies are simultaneously re-fitted to the original data. The iterative process is repeated until the signal-to-noise ratio (S/N) of the highest remaining peak drops below 5, which is the conservative threshold established in previous K2 asteroseismic studies [29].

To confirm the temporal stability of detected frequencies over each $\sim$80-day campaign, we performed wavelet analysis using the `scaleogram` Python package (version 0.9.5), which implements the continuous wavelet transform from `PyWavelet` (version 1.5.0) [30]. Time–frequency diagrams were generated to examine how frequency power evolves, distin-

guishing stable, coherent pulsation modes from transient or unstable behaviors. Together, the frequency extraction and wavelet validation ensure a comprehensive characterization of both stable and transient variability in our B-type star sample. The resulting light curves, frequency spectra, and wavelet transforms for each target are presented in Appendix D.

4. Data Reduction and Spectral Analysis

4.1. Data Reduction

All raw spectroscopic data were reduced using standard procedures from the Image Reduction and Analysis Facility (version 2.16) (`iraf`) software package [31]. The reduction process began with basic CCD corrections, including the creation of a master bias frame from zero-exposure images (*Zerocombine*) and a master flat-field frame from uniformly illuminated screens (*Flatcombine*). Each science and calibration frame was then bias-subtracted and flat-fielded to correct for electronic offsets and pixel-to-pixel sensitivity variations (*CCDPROC*). After these corrections, one-dimensional spectra were extracted from the two-dimensional images using the *Apall* task.

Wavelength calibration was performed using a high-order polynomial solution derived from arc lamp exposures (He–Ar or Ne–Ar), applying the *Identify* and *Reidentify* tasks, followed by wavelength mapping with *Dispcor*. Finally, the continuum of each spectrum was modeled and removed using the *Continuum* task, producing normalized spectra. This step is crucial for isolating line profiles from the underlying stellar and instrumental continua, thereby enabling precise atmospheric analysis.

4.2. Determination of Atmospheric Parameters

We derived the atmospheric parameters of our B-type targets by fitting normalized spectra in the blue region (3990–5110 Å) with synthetic models using the *Spectroscopy Made Easy* (`sme`) software package (version 423) [32]. Written in the Interactive Data Language (`idl`), `sme` applies a Levenberg–Marquardt non-linear least-squares algorithm to optimize the fit between observed and synthetic spectra iteratively. The selected spectral region includes key diagnostic lines: the wings of hydrogen Balmer lines (e.g., Hγ) are sensitive to surface gravity ($\log g$). At the same time, the neutral helium line (He I 4471 Å) and helium (He II 4481 Å) serve as an effective indicator of temperature ($T_{\rm eff}$). Synthetic spectra were computed assuming Local Thermodynamic Equilibrium (LTE) using the *Kurucz* ATLAS12 model atmosphere grid [33] and atomic data from the VALD3 database [34]. Input parameters included initial estimates of $T_{\rm eff}$, $\log g$, [M/H], radial velocity ($V_{\rm rad}$), projected rotational velocity ($v \sin i$), and micro/macroturbulent velocities ($V_{\rm mic}$, $V_{\rm mac}$), along with the instrumental spectral resolution.

Our fitting strategy followed a sequential, iterative procedure. We first determined $V_{\rm rad}$ by fitting the entire spectrum with fixed atmospheric parameters. Then, $T_{\rm eff}$ and $\log g$ were refined using selected diagnostic lines. Next, $v \sin i$ and $V_{\rm mic}$ (initialized at 2 km s^{-1}) were adjusted. Attempts to fit $V_{\rm mac}$ yielded unphysically high values and were therefore excluded from the final analysis [35]. In the final step, all parameters were fitted simultaneously to obtain the best global solution.

To enhance the fit and reduce errors from local normalization artifacts, the procedure was applied to smaller segments of the spectrum (typically $\sim$200 Å). This segmented approach yielded lower final χ^2 values and more reliable parameter estimates.

4.3. Projected Rotational Velocity Determination via FWHM

Because the $v \sin i$ values derived from global `sme` fits may degenerate with other broadening mechanisms, we employed an independent method to estimate the projected rotational velocity. We measured the Full-Width at Half-Maximum (FWHM) of two isolated

and rotation-sensitive spectral lines: the He I line at 4471 Å and the Mg II line at 4481 Å. The FWHM is defined as the width of a spectral line measured at half the depth between the line core and the continuum level.

Each FWHM value was obtained by fitting a Gaussian profile to the corresponding line. To account for instrumental broadening, we measured the FWHM of unblended emission lines in the He–Ar arc lamp spectra recorded during the same observing runs. The intrinsic stellar FWHM was then computed by subtracting the instrumental contribution in quadrature as follows:

$$\mathrm{FWHM}_{\mathrm{corr}} = \sqrt{\mathrm{FWHM}^2_{\mathrm{obs}} - \mathrm{FWHM}^2_{\mathrm{inst}}}. \quad (1)$$

Although this method does not disentangle rotational broadening from other effects, such as macroturbulence, it provides a robust and consistent empirical estimate of total line broadening, which is dominated by rotation in most B-type stars. We therefore adopted the $v \sin i$ values derived from the FWHM analysis as our final rotational velocity estimates for all targets with spectra obtained at OPD.

4.4. Uncertainty Estimation

The formal errors obtained from χ^2 minimization in `sme` are known to underestimate the true parameter uncertainties. To derive more reliable estimates, we implemented a Monte Carlo approach. For each star, we performed 100 simulations in which the atmospheric parameters were perturbed randomly within a 5% range around the best-fit values.

The adopted parameter for each star corresponds to the robust mean of the resulting distribution, while the associated uncertainty is represented by the standard deviation (1σ) of that distribution. This procedure provides a more realistic assessment of the uncertainties by accounting for local variations in the parameter space and the potential degeneracies among model parameters. The distributions of the Monte Carlo simulations used to estimate the uncertainties of the atmospheric parameters are presented in Appendix C for two of our targets.

4.5. Evolution Tracks

To estimate key stellar properties—mass ($M/M_\odot$), radius ($R/R_\odot$), luminosity ($L/L_\odot$), and age—we computed a dense grid of stellar evolutionary models using the *Modules for Experiments in Stellar Astrophysics* (`mesa`) software suite, version r10398 [36]. `mesa` is an open-source, one-dimensional stellar evolution code that numerically solves the equations of stellar structure and chemical composition. For this study, we adopted a simplified approach by computing all models in the non-rotating regime and neglecting mass loss.

We constructed pre-main-sequence models using OPAL Type II opacity tables [37], which account for local variations in the chemical composition, such as changes in the hydrogen and helium mass fractions. These tables were computed with a base metallicity of Z = 0.02. The models were evolved until the Zero-Age Main Sequence (ZAMS). The grid spanned stellar masses from 1.8 to 12 $M_\odot$, with a variable mass resolution of 0.02 $M_\odot$ for models up to 4.0 $M_\odot$ and 0.05 $M_\odot$ for higher masses. Each evolution track began at the Zero-Age Main Sequence (ZAMS), defined by a central hydrogen fraction $X_c \approx 1.0$, and extended to the Terminal-Age Main Sequence (TAMS), where $X_c \approx 0.001$.

Based on this grid, we interpolated fundamental stellar parameters for each star in our sample. Using a custom Python script (with the Pandas library), we matched each spectroscopically derived pair of T_{eff} and $\log g$ values to the closest model track. We interpolated along it to estimate the corresponding mass, radius, luminosity, and age.

To quantify the uncertainties, we propagated the 1σ errors in $T_{\rm eff}$ and $\log g$ through the same interpolation routine. For each star, we repeated the procedure using the upper and lower error bounds of the input parameters. The uncertainty on each derived parameter was then taken as the maximum deviation from the nominal value obtained with the best-fit inputs.

5. B-Type Stars Variability

The full methodology and decision criteria used to assign each star to a specific variability class are described in detail in Section 4 of [12]. To ensure consistency with our previous work, we followed the same approach here. Our classifications were derived through a multi-step process that combined (i) visual inspection of K2 light curves, (ii) frequency analysis using iterative prewhitening, and (iii) cross-validation with the stars' positions in the *Gaia* H–R diagram. Literature records from SIMBAD and VizieR were also consulted to complement the classification. Different team members independently reviewed the light curves, and any disagreements were resolved through discussion.

The quantitative criteria adopted to distinguish the main classes (frequency ranges, amplitude regimes, and light-curve morphology) follow the definitions of Balona et al. [38], McNamara et al. [39], and the GCVS [40], as discussed in detail by Pereira et al. [12]. For clarity, the subsections below present each variability type with its defining frequency ranges and representative examples (Sections 5.1–5.5). This ensures that the classification is reproducible and not based on visual inspection alone.

This framework encompasses classical pulsator types, such as slowly pulsating B-type (SPB) stars, which exhibit low-frequency g-mode oscillations, and β Cephei stars, characterized by high-frequency p-modes. Stars showing both mode types are classified as hybrid pulsators. Additionally, our scheme incorporates more recently defined classes, including Stochastic Low-Frequency (SLF) variables and Maia/Fast-Rotating Pulsating B (FaRPB) stars, as well as non-pulsational categories encompassing rotational variables and binary systems.

The variability classes identified are described in the following subsections.

5.1. SPB Stars

Slowly pulsating B-type (SPB) stars form a class of multi-periodic pulsating variables originally described by Waelkens [41]. They are less massive than β Cephei stars, typically ranging from 3 to 7 $M_\odot$, and span spectral types B2 to B9, corresponding to effective temperatures between 11,000 and 22,000 K. These stars occupy the upper main sequence region in the H–R diagram and pulsate in high-order gravity modes (g-modes), where buoyancy acts as the restoring force. Because gravity modes in SPB stars are susceptible to the near-core regions, they provide powerful constraints on the chemical composition gradient beyond the convective core and on processes such as mixing, diffusion, and core overshooting [42–47].

The pulsation frequencies of SPB stars generally lie within the range $0.5\ \mathrm{d}^{-1} < f < 3.5\ \mathrm{d}^{-1}$. However, due to the photometric overlap between SPB and Be stars [48], we adopted an extended upper limit of $5\ \mathrm{d}^{-1}$ to account for potential contributions from pulsations in rapidly rotating objects.

Theoretical models attribute the excitation of SPB pulsations to the κ-mechanism, which is driven by an opacity bump caused by iron-group elements at temperatures of around 200,000 K. This mechanism is capable of exciting multiple non-radial g-modes (e.g., [49,50]).

SPB stars are often found as slow to moderate rotators, with many showing projected rotational velocities $v \sin i \lesssim 100\ \mathrm{km\,s^{-1}}$ [51,52]. However, both observational and

modeling studies have demonstrated that their rotation rates span a much wider range, from nearly non-rotating stars up to ∼0.9 of the critical velocity [45,47,53–56]. This diversity in rotation makes SPB stars particularly valuable for asteroseismic investigations of angular momentum transport and internal mixing in intermediate-mass stars.

The star EPIC 212431975 appears in Simbad as a hot subdwarf candidate with a spectral type of B4 [57]. However, our analysis of its K2 light curve reveals a different nature. The frequency spectrum, presented in Figure 2a, clearly shows a set of low-frequency pulsations that are characteristic of a slowly pulsating B-type (SPB) variable. This new classification is further supported by *Gaia* parallax data, which place the star firmly on the main sequence in a color-magnitude diagram, contradicting the subdwarf hypothesis. Similarly, EPIC 212450527 was also listed in Simbad as a hot subdwarf candidate with a B7 spectral type. Our photometric analysis revealed that it also exhibits pulsation frequencies consistent with the SPB instability strip. Although a dedicated spectrum could not be obtained for these faint targets (V > 12.6) with the available telescope time, the position of EPIC 212450527 on the *Gaia* color-magnitude diagram also confirms a main-sequence nature. Based on this combined photometric and astrometric evidence, we reclassified both EPIC 212431975 and EPIC 212450527 as SPB stars.

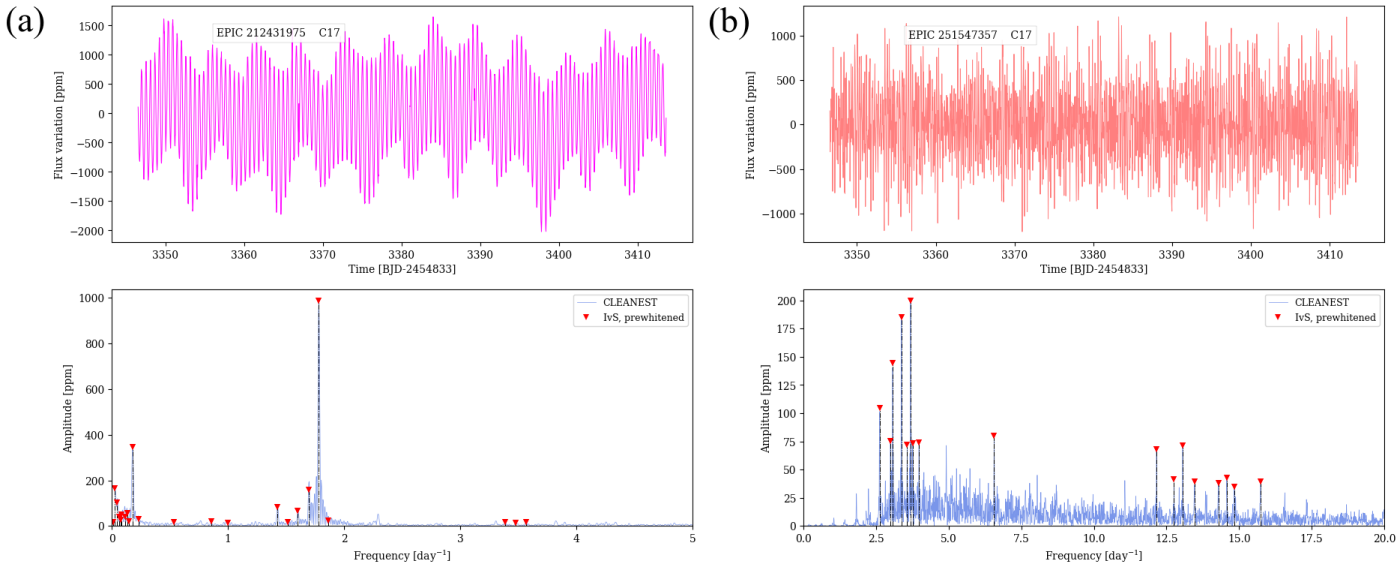


Figure 2. (**a**) K2 light curve and frequency spectrum of EPIC 212431975 (EC 13318−1356) observed during Campaign 17. The lower panel displays the frequency spectrum, revealing multiple low-frequency peaks consistent with SPB-type gravity-mode pulsations. (**b**) The same for EPIC 251547357 (HD 120086), also from Campaign 17. The lower panel shows both low-frequency *g*-modes, typical of SPB stars, and high-frequency *p*-modes characteristic of β Cephei pulsators, confirming its hybrid nature. In both frequency spectra, the blue line shows the result of the `cleanest` algorithm [27], while red triangles mark significant frequencies ($S/N \geq 5$) identified with the IVS-KULeuven iterative prewhitening routine [28].

5.2. β Cephei/SPB Hybrid Stars

The β Cephei variables are hot, luminous blue stars that occupy the upper-left region of the H–R diagram. This class encompasses early B-type stars of luminosity classes III, IV, and V, with effective temperatures between 18,000 and 30,000 K and masses from 7 to 20 $M_{\odot}$ [58]. These stars are characterized by pulsations in the range of $3.5 < f < 20\ \mathrm{d}^{-1}$. They primarily exhibit non-radial pressure modes (*p*-modes) of pulsation, which are driven by the κ-mechanism. These surface pulsations produce rapid brightness variations with amplitudes typically ranging from 0.01 to 0.3 in magnitude over periods of 0.1 to 0.3 days [59].

The pulsations are driven by the so-called "Fe bump" or "Z bump", which entails an increase in opacity caused by iron-group elements in the stellar interior at a temperature of approximately 200,000 K [60]. This opacity increase traps energy, raises the pressure, and pushes the stellar layers outward, repeating on timescales of a few hours. According to [50], the driving of pulsations via the κ-mechanism can only occur if specific criteria are met: (1) the pulsation period must be on the same order as, or shorter than, the local thermal timescale, and (2) the pressure variation must be considerable and vary slowly within the driving region. In β Cephei stars, this opacity increase is located in a relatively shallow layer, where the thermal timescale is well under one day, satisfying the conditions for driving low-order radial p-modes and high-order g-modes with low angular degrees ($\ell < 6$).

A class of hybrid pulsators, known as β Cephei/SPB stars, has also been identified in the literature [61,62]. In addition to the characteristic high-frequency pulsations of β Cephei stars, these hybrids also exhibit low-frequency pulsations typically found in slowly pulsating B-type (SPB) stars. In the H–R diagram, these hybrid stars are located at the intersection of the β Cephei and SPB instability strips [63] and exhibit pulsation frequencies spanning the combined range of 0.5 to 20 d^{-1}.

The star EPIC 251547357 (HD 120086), observed during Campaign 17, has been classified as a hybrid SPB/β Cephei (HYB) pulsator. It is a main-sequence star with a V magnitude of 7.82. Our spectral analysis of its blue-region spectrum yielded an effective temperature of $T_{\mathrm{eff}} = 20,500 \pm 800$ K and a surface gravity of $\log g = 4.3 \pm 0.1$ dex. By placing these parameters on stellar evolution tracks computed with `mesa`, we derived a mass of $M = 6.9^{+0.9}_{-0.6}\ M_{\odot}$, a radius of $R = 3.3^{+0.7}_{-0.2}\ R_{\odot}$, and a luminosity of $L = 1700^{+1200}_{-400}\ L_{\odot}$. These properties are consistent with its B2V spectral type from the Simbad database [64] and place the star in the H–R diagram at the intersection of the SPB and β Cephei instability strips. The hybrid nature of EPIC 251547357 has been confirmed by its frequency spectrum, which is shown in Figure 2b. The analysis reveals the presence of two distinct groups of pulsation modes. The first group consists of low-frequency modes, characteristic of SPB variables, which are driven by gravity (g-modes). The second group comprises high-frequency modes, typical of β Cephei stars, which are driven by pressure (p-modes). The simultaneous detection of both types of pulsation is the defining characteristic of a hybrid pulsator, making this star an excellent laboratory for studying the coexistence of different oscillation mechanisms.

5.3. SLF Stars

Stochastic Low-Frequency (SLF) variability was first reported by [65], who identified an excess of low-frequency, low-amplitude signal—termed "red noise"—in the periodograms of three young O-type stars observed by the CoRoT mission. Since then, SLF variability has been detected in a wide range of hot and luminous stars, including Wolf–Rayet (WR) stars; Luminous Blue Variables (LBVs); and main-sequence O-, B-, A-, and F-type stars [66]. This type of variability, occurring at frequencies between 0.1 and 10 d^{-1}, is typically attributed to internal gravity waves (IGWs). The precision of space-based photometry missions such as CoRoT, *Kepler*, K2, and *TESS* has dramatically enhanced the detection and characterization of this phenomenon [8].

Two main mechanisms have been proposed to explain SLF variability. The first attributes it to IGWs excited by turbulent core convection in massive stars, which can transport angular momentum and affect the internal rotation profile [67]. The second mechanism proposes that sub-photospheric convection generates surface turbulence and stochastic brightness variations [68]. While initially associated with very luminous O- and

B-type stars, SLF signatures have also been observed in less-luminous B-, A-, and F-type stars, making this a dynamic and evolving area of research.

The star EPIC 247935687 (GSC 01834-00273), observed during Campaign 13, is a B9 star with a *Gaia* magnitude of 12.2. As shown in Figure 3, the light curve (top panel) does not reveal the coherent, multi-periodic oscillations that are characteristic of SPB stars. Instead, the corresponding power spectrum (bottom panel) displays a red-noise profile: The highest amplitudes are found at low frequencies, and the amplitudes of the significant peaks identified by the IVS prewhitening algorithm decrease steadily toward higher frequencies. This behavior is consistent with the definition of SLF variability, supporting the classification of this target as a stochastic pulsator.

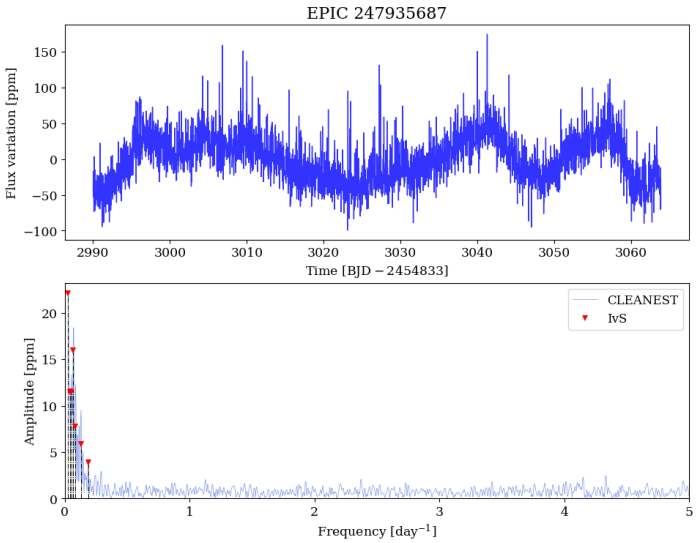


Figure 3. K2 light curve and frequency spectrum of EPIC 247935687, observed during Campaign 13. This star is classified as an SLF variable, a class characterized by an excess of power in the low-frequency region and a stochastic nature.

5.4. Maia Variables or Fast-Rotating Pulsating B

The existence of a distinct class of variable stars, with spectral types ranging from B7 III to A2 V-II and exhibiting short-period variations of 0.1 to 0.3 days, was first proposed by [69]. This class was named "Maia variables" after its prototype, the Pleiades cluster member known as Maia. They were considered high-frequency pulsators: too hot to be classified as δ Scuti stars and too cool to be classified as β Cephei variables. However, ref. [70] later retracted this proposal after concluding that Maia itself did not exhibit short-period variability in either luminosity or radial velocity but rather showed non-periodic variations in the strength and width of its helium lines. Despite this retraction, the concept of a Maia variable class persisted in the literature.

The existence of Maia variables has been a subject of debate. Subsequent research by [71] failed to find periodicities in the proposed range. Ref. [72] argued that a separate class for Maia variables was unnecessary, suggesting that any star matching the description could be a rapidly rotating, slowly pulsating B-type (SPB) star whose gravity modes have been shifted to higher frequencies by the Coriolis force [73]. As an alternative mechanism, ref. [74] investigated Rossby waves, which can also be excited in rotating SPB star models.

With the advent of high-precision space-based photometry, new insights have been gained into this topic. Using K2 data, ref. [75] determined Maia to be a rotational variable with 10 days but found no evidence of high-frequency pulsations, though [76] later reported rapid variations in its far-ultraviolet luminosity. Meanwhile, studies using CoRoT [77] and the Swiss Euler telescope [78] identified B-type pulsators located between the SPB and δ

Scuti instability strips that exhibit a wide range of pulsation frequencies. Ref. [79] found that most of these pulsators in the cluster NGC 3766 are fast rotators ($v \sin i > 200$ km s^{-1}) and termed them fast-rotating pulsating B-type (FaRPB) stars. Ref. [80] has argued that the properties of these FaRPB stars are analogous to those historically attributed to Maia variables. Subsequently, a population of Maia candidates has been identified and classified using data from the *Kepler*, *TESS*, and *Gaia* missions [81–83].

Recent analyses by [80] of hundreds of Maia variables observed by *TESS* characterize them as a group of main-sequence stars with effective temperatures ranging from 10,000 to 18,000 K (spectral types A0–B5). The study suggests that distinct instability strips, as predicted by models, may not exist. Instead, the pulsation properties appear to merge smoothly from β Cephei to Maia variables and then to δ Scuti stars at high frequencies, with a similar blurring of boundaries between SPB, A-type, and γ Doradus stars at low frequencies. Consequently, it becomes difficult to establish well-defined temperature or frequency boundaries for these classes. Ref. [80] also argues that current pulsation models are unable to explain the highest observed frequencies and that other mechanisms, such as convection or starspots, may play a driving role.

One example of this class is the star EPIC 247273628, which was observed during Campaign 13. As shown in Figure 4a, its photometric characteristics are consistent with a Maia classification. Its light curve (top panel) displays a distinctly irregular pattern of variability, which is a hallmark of the Maia class. The photometric flux varies between approximately −5000 and +5000 ppm throughout the observational campaign. This complex, non-sinusoidal pattern contrasts with the more regular variability seen in purely rotational or binary systems. The frequency spectrum (bottom panel of Figure 4a) reveals the hybrid nature of its pulsations. A total of 96 significant frequencies were detected. The main frequency spectrum shows a concentration of frequencies around 2 d^{-1}. However, the inset reveals numerous pulsation signals at higher frequencies, extending up to the detection threshold, with the strongest amplitude observed at 15 d^{-1}. This combination of pulsation modes and its B9 spectral type places EPIC 247273628 in the Maia variable class.

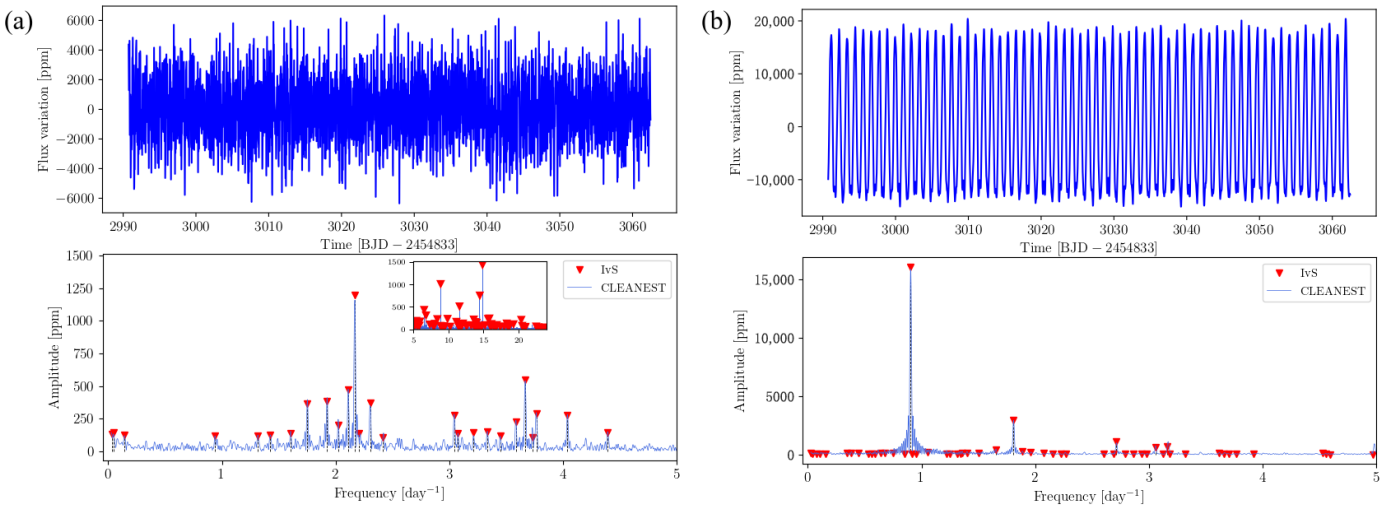


Figure 4. (**a**) Frequency spectrum of EPIC 247273628 observed during Campaign 13. The star is classified as a Maia variable based on the detection of both low-frequency *g*-mode and high-frequency pulsations. (**b**) Frequency spectrum of the star EPIC 246970807, also observed during Campaign 13, classified as a ROT/BIN variable. ROT/BIN variables are characterized by a regular fluctuations in the flux level of a star a constant average amplitude or a steady beat pattern.

5.5. Binary and Rotation Modulation Stars

Not all photometric variability observed in stars is attributable to stellar pulsations. Other standard mechanisms include binarity and rotation (classified as ROT/BIN). In binary systems, variability can arise from a variety of proximity effects, including mutual eclipses of the components, reflection, and tidal or ellipsoidal distortion [55]. Additionally, rotational modulation can be caused by an inhomogeneous stellar atmosphere, such as the presence of surface spots [38]. These non-pulsational phenomena typically produce smoother, semi-sinusoidal light curves and are characterized in the frequency spectrum by a fundamental frequency and its associated harmonics. In contrast, variability driven by pressure or gravity waves generally results in a richer and more complex frequency spectrum.

Distinguishing between these different sources of variability can be challenging from photometry alone, particularly between slowly pulsating B-type (SPB) stars and rotational variables. The complexity increases, as these phenomena can coexist; for example, B-type stars in binary systems can also exhibit pulsations, resulting in a diverse spectrum of frequencies from both pulsation and orbital or rotational effects [84]. Furthermore, beating patterns in the light curve can be caused by differential rotation, which can be mistaken for pulsation [12]. Therefore, the primary tool for classification in this work is the analysis of the frequency spectrum. The presence of a dominant frequency with a clear harmonic structure is a strong indicator of binarity or rotation, whereas a rich spectrum of independent frequencies is characteristic of pulsations. While an optical spectrum, when available, can resolve this ambiguity, a careful analysis of the frequency content is essential in its absence, with eclipsing binaries representing the most straightforward cases to classify.

An example of a rotational variable (ROT/BIN class) in our sample is EPIC 246970807, whose light curve and frequency analysis are presented in Figure 4b. Its light curve (top panel) exhibits a regular, smooth, semi-sinusoidal modulation with a peak-to-peak flux variation of approximately 30,000 ppm. This stable, periodic pattern is characteristic of rotational variability, likely caused by large-scale surface features or ellipsoidal deformation, with negligible influence from pulsations. The regularity of the light curve clearly distinguishes it from the complex, multi-periodic patterns observed in pulsating stars. The frequency spectrum of EPIC 246970807 (bottom panel of Figure 4b) supports this classification. It is dominated by a strong fundamental frequency near $\nu \approx 1$ d^{-1}, which we interpret as the rotational frequency and its associated harmonics. This structure is distinctly different from the rich spectra of independent pulsation modes seen in SPB or Maia variables. Although the prewhitening process revealed several other low-amplitude signals, particularly above 5 d^{-1} (shown in the inset), their very low power relative to the fundamental frequency suggests they are likely instrumental artifacts or noise rather than evidence of pulsations. Our spectral analysis classifies this star as a B6IV-V type.

6. Results

The results of our photometric analysis for the stars in K2 Campaigns 13 and 15–18 are summarized in Table 1. SPB denotes slowly pulsating B-type stars (Section 5.1), while HYB refers to hybrid pulsators exhibiting both β Cephei and SPB frequencies (Section 5.2). The MAIA class includes Maia variables and fast-rotating SPB stars. Additionally, we identify stars with Stochastic Low-Frequency variability as SLF (Section 5.3). Non-pulsational variability (Section 5.5) is categorized as ROT (rotational modulation), BIN (binary effects), or EBIN (eclipsing binaries). Targets in which no significant periodic signal was detected above our signal-to-noise threshold, or those showing only erratic behavior, are classified as Aperiodic (AP). In some instances, the designation AP may reflect signals of instrumental origin rather than genuine stellar variability.

Table 1. Distribution of variability classes among the observed B-type stars K2 Campaigns 11 [12], and 13 through 18.

Variability Class	Campaign 11	Campaigns 13–18	Total
SPB	39	31	70
ROT/BIN	53	19	72
SLF	13	2	15
MAIA	5	9	14
EBIN	9	3	12
HYB	3	1	4
AP (Aperiodic)	–	8	8
Total	122	73	195

Table A2 presents the final variability classification for each star, along with key parameters derived from the frequency analysis: the total number of significant frequencies detected ($N_{freq.}$), the frequency of maximum amplitude ($\nu_{A_{max}}$), and its corresponding amplitude value (A_{max}). These parameters were extracted from the K2 light curves using the methods described in Sections 3 and 5. In many cases, both in our current and previous work, a star was assigned multiple classifications, reflecting the coexistence of different physical mechanisms causing variability. This finding aligns with other extensive studies of O- and B-type stars from K2 and *TESS*, which also report a high fraction of objects with multiple variability types [85–87].

To increase the statistical significance of our sample and place our new findings in a broader context, we combined the results from Campaigns 13–18 with our previous analysis of B-type stars from Campaign 11 [12]. To contextualize our findings, we compared the distribution of variability classes in this combined sample with the results from the comprehensive study of B-type stars by [81], which analyzed data from the original *Kepler* mission and K2 Campaign 0. This comparison is illustrated in Figure 5. A notable similarity between the two studies is the prevalence of rotational variables and SPB stars, which together constitute over 50% of the classified objects in both samples. Our analysis identified 72 stars exhibiting dominant rotational modulation and 70 SPB stars compared to 45 rotational variables and 36 SPB stars found by [81].

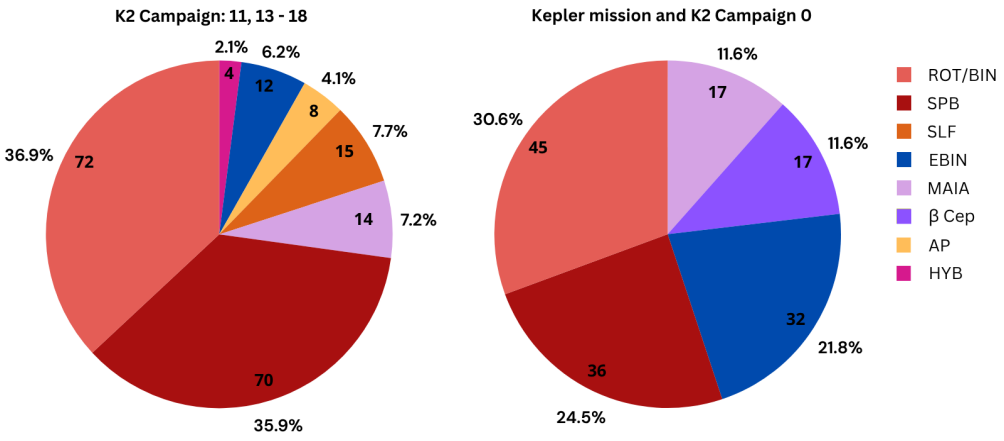


Figure 5. Comparison of the distribution of variability classes, represented by colors, of the target stars observed during Campaigns 11, 13, and 15–18 of the K2 mission, according to the analysis carried out by our research group (**left**), and the distribution of variability classes obtained by [81] for stars observed during the *Kepler* mission and in Campaign 0 of the K2 mission (**right**).

Table 2 presents the physical stellar parameters derived from our spectroscopic analysis (see Section 4.2), including effective temperature ($T_{\rm eff}$), surface gravity ($\log g$), and projected rotational velocity ($v \sin i$). Appendix E presents the observed spectrum and the final fit obtained from the analysis. The $T_{\rm eff}$ and $\log g$ values obtained via the `sme/monte carlo` procedure were used as input for a Python routine to determine fundamental stellar parameters by interpolating within the evolutionary grids generated with the `mesa` code. The resulting output parameters include stellar mass, radius, luminosity, and age. Accordingly, Table 2 also presents the values for the mass ($M/M\odot$), radius ($R/R\odot$), and luminosity ($L/L\odot$) values for the stars with spectroscopic measurements. The evolution tracks were calculated for non-rotating models without any mass loss (see Section 4.5). Finally, the table also lists the variability classification for each star.

Table 2. Physical stellar parameters of 34 stars derived from the spectra by the methodology described in Section 4. The SIMBAD identifier of HQ Lib appears as "V* HQ Lib", where "V*" denotes a variable star.

Camp.	SIMBAD ID	EPIC	$T_{\rm eff}$ (K)	$\log g$ (dex)	$v \sin i$ (km s^{-1})	$\log(L/L_\odot)$	$M/M_\odot$	$R/R_\odot$	Class
13	HD 28436	210650598	11,300 ± 300	4.0 ± 0.1	120 ± 30	2.1 ± 0.1	3.2 ± 0.2	3.0 ± 0.4	SPB
	HD 285777	210671425	10,500 ± 400	4.2 ± 0.2	110 ± 30	1.9 ± 0.2	2.8 ± 0.3	2.7 ± 0.7	AP
	HD 27877	210737173	11,600 ± 400	3.6 ± 0.2	95 ± 40	2.8 ± 0.3	4.3 ± 0.7	6 ± 2	SPB/SLF
	HD 28304	210853356	13,500 ± 300	3.8 ± 0.1	110 ± 30	2.8 ± 0.1	4.5 ± 0.3	4.5 ± 0.6	SPB
	HD 27742	210873575	13,100 ± 200	3.8 ± 0.1	160 ± 40	2.7 ± 0.1	4.3 ± 0.2	4.4 ± 0.6	MAIA
	HD 31747	246698204	13,400 ± 200	3.9 ± 0.1	150 ± 40	2.7 ± 0.1	4.2 ± 0.2	3.9 ± 0.5	EBIN
	HD 33402	246970807	14,400 ± 400	4.4 ± 0.1	130 ± 40	2.4 ± 0.1	4.0 ± 0.2	2.6 ± 0.2	ROT/BIN
	HD 28867	247031423	10,900 ± 300	4.0 ± 0.2	180 ± 50	2.1 ± 0.2	3.1 ± 0.3	3.1 ± 0.8	SPB/BIN
	HD 284634	247211157	9400 ± 400	3.5 ± 0.2	100 ± 60	2.4 ± 0.3	3.4 ± 0.5	6 ± 2	MAIA/SLF
	HD 34133	247234723	17,800 ± 500	4.3 ± 0.1	100 ± 30	3.0 ± 0.1	5.7 ± 0.3	3.3 ± 0.4	SPB/SLF
	HD 32481	247430338	16,900 ± 400	3.4 ± 0.1	135 ± 40	3.9 ± 0.2	8.3 ± 0.8	10 ± 2	SPB/BIN
	HD 284993	247495377	15,000 ± 300	4.1 ± 0.1	170 ± 70	2.7 ± 0.1	4.6 ± 0.3	3.2 ± 0.4	ROT/BIN
	HD 32641	247612547	13,900 ± 300	3.6 ± 0.1	145 ± 40	3.1 ± 0.1	5.2 ± 0.4	6.1 ± 0.9	EBIN
	HD 284941	247682580	10,500 ± 400	4.0 ± 0.1	240 ± 40	2.0 ± 0.2	2.9 ± 0.2	2.9 ± 0.4	MAIA/SLF
	HD 30122	247688426	13,900 ± 600	3.4 ± 0.1	110 ± 30	3.4 ± 0.2	6.2 ± 0.7	9 ± 2	ROT/BIN
	HD 285127	247695418	11,900 ± 400	4.0 ± 0.1	220 ± 120	2.3 ± 0.1	3.4 ± 0.2	3.2 ± 0.5	ROT/BIN
	HD 285124	247696147	11,300 ± 400	4.2 ± 0.1	240 ± 30	1.9 ± 0.1	2.9 ± 0.2	2.4 ± 0.3	MAIA/SLF
	HD 284119	247757517	11,000 ± 500	3.8 ± 0.2	350 ± 140	2.4 ± 0.3	3.4 ± 0.5	4 ± 1	SPB
	HD 284045	247759652	9500 ± 400	3.8 ± 0.2	160 ± 90	2.0 ± 0.3	2.8 ± 0.4	3.8 ± 1.1	ROT/BIN
	GSC 01829-00022	247774959	10,500 ± 300	3.6 ± 0.1	180 ± 30	2.4 ± 0.1	3.5 ± 0.3	5.0 ± 0.8	ROT/BIN
15	HD 143567	204525956	10,700 ± 300	4.1 ± 0.1	190 ± 10	1.9 ± 0.1	2.8 ± 0.2	2.6 ± 0.4	AP
	HD 141774	204848812	11,100 ± 300	4.1 ± 0.1	150 ± 30	2.0 ± 0.1	3.0 ± 0.2	2.6 ± 0.4	SPB
	HD 139094	249135451	13,400 ± 100	4.3 ± 0.1	150 ± 10	2.3 ± 0.1	3.7 ± 0.2	2.6 ± 0.3	SPB
	HD 138343	249481830	11,300 ± 400	4.2 ± 0.1	230 ± 50	1.9 ± 0.1	2.9 ± 0.2	2.4 ± 0.3	ROT/BIN
	HD 139486	249661590	9900 ± 500	4.1 ± 0.2	180 ± 30	1.8 ± 0.2	2.6 ± 0.3	2.7 ± 0.7	AP
	V* HQ Lib	249811956	13,700 ± 100	4.2 ± 0.1	40 ± 20	2.4 ± 0.1	3.8 ± 0.2	2.7 ± 0.3	EBIN
	HD 134796	249919216	10,600 ± 400	4.0 ± 0.2	100 ± 20	2.0 ± 0.2	3.0 ± 0.3	3.1 ± 0.8	AP
	BD-13 4202	250131922	14,600 ± 100	4.3 ± 0.1	120 ± 30	2.5 ± 0.1	4.3 ± 0.2	2.9 ± 0.4	SPB
17	EC 15103-1557	212744655	15,800 ± 100	4.5 ± 0.1	100 ± 30	2.6 ± 0.1	4.5 ± 0.1	2.5 ± 0.1	SPB
	HD 118246	251547357	20,600 ± 800	4.3 ± 0.1	110 ± 20	3.4 ± 0.1	7.3 ± 0.5	3.8 ± 0.4	HYB
18	HD 120086	211404031	11,410 ± 100	4.4 ± 0.1	170 ± 20	1.9 ± 0.1	2.9 ± 0.1	2.2 ± 0.2	AP
	HD 73046	211712203	11,700 ± 200	3.8 ± 0.1	170 ± 30	2.4 ± 0.1	3.6 ± 0.2	4.0 ± 0.5	SLF
	HD 75750	211941698	15,100 ± 100	3.4 ± 0.1	180 ± 20	3.6 ± 0.1	6.9 ± 0.6	9 ± 1	SPB/SLF
	HD 71052	211996306	11,500 ± 200	4.0 ± 0.1	130 ± 30	2.2 ± 0.1	3.2 ± 0.2	3.1 ± 0.4	SPB

With these fundamental parameters established, we further investigated the pulsational properties of our targets by placing them on an H–R diagram, using the effective temperatures derived from our `sme` analysis and luminosities from the `mesa` evolution tracks (Figure 6). While our analysis did not identify any pure β Cephei candidates, it did reveal one hybrid (HYB) star, EPIC 251547357. As shown in the figure, the observed pulsational behavior of this star aligns excellently with its location at the intersection of the theoretical instability strips for β Cephei (blue dashed lines) and SPB stars (red dashed lines), as calculated by [88]. This observation provides strong validation for its classification

as a hybrid pulsator. The second group of high-frequency pulsating stars is identified as Maia/FaRPB types, located well below the β Cephei instability strip. EPIC 247211157 appearappears to begin its evolution outside the main sequence. Stars classified as SPB fall within the expected instability region. In the upper region of the diagram, we observe one case (EPIC 247430338) positioned near the border of the instability strip, within the uncertainty limits. Based on its light curve, this object exhibits typical SPB pulsations. However, we also suspect it to be part of a binary system. If confirmed, the presence of a companion could account for its more evolved position in the diagram. Additionally, we observe an SLF pulsator located in the region associated with late-type main-sequence B stars, which is consistent with recent findings for this class of object.

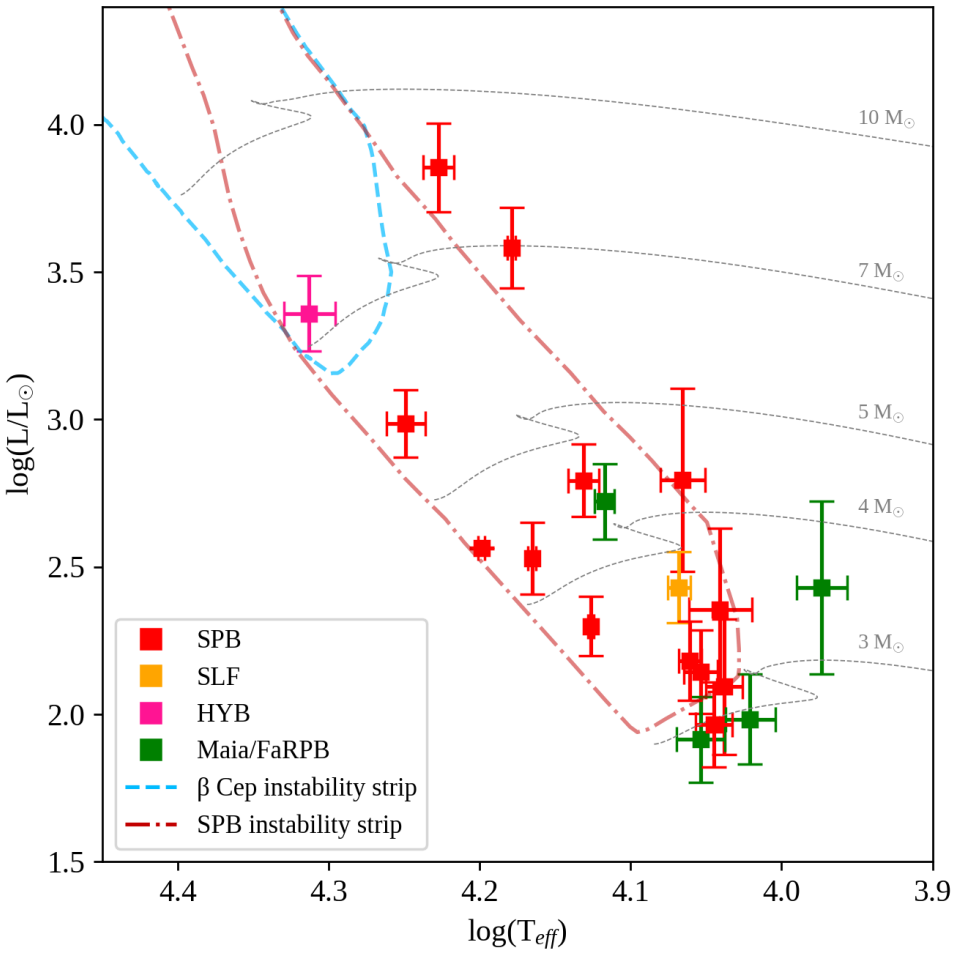


Figure 6. H–R diagram for the pulsating B stars observed in K2 Campaigns 13 through 18. The effective temperatures were obtained from the analysis of blue-region spectra using the `sme` package. At the same time, the luminosities were determined by placing the stars on evolution tracks calculated with `mesa` (see Section 4). The points are color-coded according to their variability class. The theoretical instability strips for β Cephei and SPB stars from [88] are also shown, along with the underlying `mesa` evolution tracks (gray lines).

7. Discussion

This study provides a detailed characterization of the photometric and spectroscopic variability of B-type stars observed during K2 Campaigns 13–18. By combining space-based photometry, ground-based spectroscopy, and comparisons with stellar evolutionary tracks to estimate fundamental parameters, we expand on previous work and offer new insight into the diversity of variability mechanisms in these stars.

Our findings reinforce the view that variability classes in B-type stars are better described as a continuum influenced by rotation, binarity, and other factors, rather than by sharply bounded instability strips. These results highlight the need for a multidimensional, physically motivated framework for classifying variability in B-type stars.

A large fraction of our sample shows SPB-type variability, and their locations in the H–R diagram align well with theoretical predictions. A hybrid pulsator, such as EPIC 251547357, combines SPB-like *g*-modes with high-frequency *p*-modes, supporting the growing evidence that such mixed behavior is more common than previously assumed. Several targets exhibit the broad frequency spectra typical of Maia/FaRPB variables. Instead of revisiting the extensive historical debate, we emphasize that our results support the interpretation of these objects as part of a continuum of pulsational behavior modulated by rapid rotation, rather than as a distinct class.

We also found stars with Stochastic Low-Frequency (SLF) signatures in the SPB region that lack coherent modes, which suggests a shift or competition between stochastic and coherent pulsational states. The presence of SLF signatures shows the need to investigate internal gravity waves in hot stars.

Detecting rotational modulation and eclipsing binaries (ROT/BIN) meets our expectations for spotted stars and close binary interactions. In some systems, pulsational signals co-occur with binary signatures, underscoring the diagnostic potential of asteroseismology, even in complex situations.

Although some Be stars were observed in K2 Campaigns 13–18, we chose not to include those known cases in this analysis. We plan to handle them in a future study. However, we recognize that, without complete spectral coverage, we cannot completely rule out the presence of undetected Be stars. These stars might coexist with other types of photometric variables, like SPB stars, in the same part of the main sequence. Both Be and SPB stars can show low-order *g*-mode pulsations. Groups of closely spaced frequencies are often reported in classical Be stars. However, we also see these patterns in SPB stars that lack evidence of a circumstellar disk. Currently, only 22 stars in our sample lack sufficient spectral data to definitively confirm or exclude Be characteristics.

Changing the classification of some stars from hot subdwarfs to main-sequence SPB stars shows how important it is to bring together *Gaia*'s precise measurements with photometric and spectroscopic data. Using multiple data sources helps resolve classification uncertainties and track stellar evolution more accurately.

In the coming years, missions like *PLATO* will provide much richer datasets, enabling the creation of more detailed models of hybrid and SPB stars. Working together with coordinated observations, such as combining spectroscopy with polarimetry, will be crucial to gaining a deeper understanding of how pulsation, rotation, and magnetic fields interact and evolve in these stars.

Author Contributions: Conceptualization, methodology, validation, formal analysis, investigation, and writing—review and editing, all authors; software and data curation, B.V.H.V.d.S., A.W.P., and J.M.E.; resources, supervision, project administration, and funding acquisition, M.E., M.C.R.-S., and E.J.-P.; writing—original draft preparation and visualization, all authors; observation of stellar spectra at OPD, B.V.H.V.d.S., A.W.P., L.A., M.E., and J.M.E. All authors have read and agreed to the published version of the manuscript.

Funding: This study was financed in part by the Coordenação de Aperfeiçoamento de Pessoal de Nível Superior—Brazil (CAPES)—Finance Code 001, by the Fundação de Amparo à Pesquisa do Estado de São Paulo (FAPESP) through grant 2016/13750-6, and by the State Secretariat of Science, Technology, and Higher Education of Paraná (SETI–Fundo Paraná, grant 031/2024), with the explicit acknowledgement: "Project funded with resources from the State Secretariat of Science, Technology,

and Higher Education–SETI–Fundo Paraná." M.E. gratefully acknowledges the financial support of the "Fenômenos Extremos do Universo" project, Fundação Araucária, grant 348/2024.

Data Availability Statement: The K2 data presented in the study are openly available in the Mikulski Archive for Space Telescopes (MAST), which can be found at https://archive.stsci.edu/missions-and-data/k2 (accessed on 10 June 2025). This work has made use of data from the European Space Agency (ESA) mission *Gaia*, which can be found at https://gea.esac.esa.int/archive/ (accessed on 10 June 2025).

Acknowledgments: This paper includes data collected by the K2 mission. Funding for the K2 mission was provided by NASA's Science Mission Directorate. This paper is also based on observations obtained at the Pico dos Dias Observatory/LNA/MCTI. This work has made use of the VALD database, which is operated at Uppsala University, the Institute of Astronomy RAS in Moscow, and the University of Vienna. This work makes use of spectroscopic data from the Large Sky Area Multi-Object Fiber Spectroscopic Telescope (LAMOST) Survey.

Conflicts of Interest: The authors declare no conflicts of interest.

Appendix A. List of Targets

Table A1 presents a list of the target stars from K2 Campaigns 13 and 15–18 that have been analyzed in this work. For each star, the table lists its respective K2 campaign number, EPIC identifier, primary Simbad identifier, right ascension and declination, V-band magnitude, and the spectral type—as recorded in the Simbad database. In SIMBAD identifiers, "V*" denotes a variable star. The target selection methodology follows the doctoral theses of Silva (Campaign 13) [89] and Eidam (Campaigns 15–18) [90].

Table A1. Catalogue of targets observed in Campaigns 13–18.

Camp.	EPIC ID	Simbad ID	RA (J2000)	DEC (J2000)	Mag V	Spec. Type (Simbad)
13	210650598	HD 28436	04:29:48	+17:40:39	7.8	B7V
13	210671425	HD 285777	04:25:25	+17:57:45	10.5	B8
13	210737173	HD 27877	04:24:42	+18:54:47	7.4	B8V
13	210853356	HD 28304	04:28:42	+20:40:38	7.7	B8
13	210873575	HD 27742	04:23:32	+20:58:55	6.0	B8IV-V
13	246698204	HD 31747	04:58:57	+14:32:58	7.6	B6V
13	246704649	HD 286109	04:51:29	+14:37:53	11.0	B9
13	246788829	HD 31708	04:58:31	+15:37:11	8.9	B9
13	246820783	HD 28868	04:33:25	+15:57:39	9.1	B8
13	246968117	HD 286146	04:54:04	+17:24:49	10.5	B9
13	246970807	HD 33402	05:10:39	+17:26:24	7.9	B8
13	246988320	HD 286141	04:55:36	+17:36:35	10.5	B9
13	247031423	HD 28867	04:33:32	+18:01:00	7.0	B9IVn
13	247131891	HD 286010	04:44:30	+18:58:26	10.2	B8
13	247146962	BD+18 708	04:45:42	+19:07:07	10.4	B8
13	247147343	HD 285995	04:46:00	+19:07:18	9.6	B9
13	247147476	BD+18 701	04:45:15	+19:07:23	9.9	B8
13	247148453	HD 285993	04:45:14	+19:07:57	11.6	B5
13	247153152	HD 285996	04:45:58	+19:10:39	9.3	B9
13	247160983	HD 284732	04:44:29	+19:15:06	9.8	B8
13	247164195	HD 284841	04:45:48	+19:16:56	9.3	B9II

Table A1. *Cont.*

Camp.	EPIC ID	Simbad ID	RA (J2000)	DEC (J2000)	Mag V	Spec. Type (Simbad)
13	247169375	HD 285097	04:56:54	+19:9:51	10.9	B
13	247192878	HD 284828	04:49:37	+19:33:24	10.0	B5
13	247211157	HD 284634	04:37:12	+19:43:50	10.2	B9
13	247234723	HD 34133	05:15:50	+19:57:14	8.1	B8
13	247264203	HD 284914	04:55:08	+20:13:37	10.6	B8
13	247273628	HD 285065	04:55:56	+20:18:46	10.8	B9
13	247278704	HD 284820	04:48:45	+20:21:34	10.1	B9
13	247430338	HD 32481	05:04:22	+21:38:36	8.0	B3V
13	247457814	HD 285174	05:03:58	+21:51:51	10.9	B9
13	247495377	HD 284993	04:57:12	+22:09:34	10.3	B9
13	247551785	HD 31856	05:00:09	+22:35:33	8.7	B9
13	247554799	HD 31916	05:00:33	+22:36:56	9.1	B8
13	247559520	HD 29450	04:39:13	+22:39:08	8.6	B9
13	247612547	V* V1154 Tau	05:05:37	+23:03:39	6.8	B5
13	247682580	HD 284941	04:58:41	+23:35:06	11.4	B9
13	247688426	HD 30122	04:45:42	+23:37:40	6.3	B5III
13	247692420	BD+23 817	05:03:31	+23:39:25	10.6	B9
13	247695418	HD 285127	05:03:32	+23:40:46	9.7	B9
13	247696147	HD 285124	05:03:57	+23:41:06	11.0	B9
13	247698073	HD 284937	05:01:44	+23:41:56	9.6	B9
13	247705729	HD 285118	05:04:55	+23:45:11	10.7	B9
13	247709560	HD 284935	05:01:27	+23:46:49	9.1	B9
13	247714018	HD 285117	05:04:45	+23:48:43	10.4	B9
13	247714396	HD 285109	05:03:23	+23:48:53	10.6	B9
13	247742016	HD 31353	04:56:07	+24:00:16	8.2	B8
13	247757517	HD 284119	05:03:38	+24:06:55	10.2	B9
13	247759652	HD 284045	05:00:14	+24:07:48	10.6	B9
13	247774959	GSC 01829-00022	04:33:53	+24:14:08	12.5	B8
13	247786632	HD 32247	05:02:45	+24:19:00	8.6	B9
13	247806245	GSC 01833-01018	04:35:32	+24:27:06	13.0	B8
13	247889905	HD 284091	05:02:30	+25:01:24	11.1	B9
13	247895553	GSC 01849-00811	05:02:27	+25:03:43	13.5	B9
13	247935687	GSC 01834-00273	04:39:39	+25:20:34	∼	B9
13	248064520	HD 284006	04:58:07	+26:17:54	9.8	B9
13	248150769	HD 283800	04:43:27	+27:01:37	9.8	B8
13	248227339	HD 283845	04:47:52	+27:44:40	9.6	B9
15	204525956	HD 143567	16:01:55	+21:58:49	7.2	B9 V
15	204848812	HD 141774	15:51:30	−20:35:14	7.7	B9 V
15	249135451	HD 139094	15:37:07	−26:29:33	7.4	B8 IV/V
15	249481830	HD 138343	15:32:10	−21:58:01	7.2	B9 V
15	249661590	HD 139486	15:39:00	−19:43:57	7.6	B9 V
15	249811956	V* HQ Lib	15:38:55	−17:44:35	10.7	B7
15	249919216	HD 134796	15:12:21	−16:24:40	7.4	B9 V
15	250131922	EC 15327-1341	15:35:30	−13:51:51	11.0	B6
17	212431975	EC 13318-1356	13:34:28	−14:11:45	12.7	B4
17	212450527	EC 13211-1331	13:23:46	−13:47:26	12.7	B7
17	212744655	TYC 4973-1471-1	13:46:47	−07:07:32	11.8	B
17	251547357	HD 120086	13:47:19	−02:26:37	7.8	B2 IV
18	211404031	HD 73046	08:36:31	+11:42:13	8.1	B9
18	211712203	HD 68903	08:14:59	+16:04:43	7.3	B8
18	211941698	HD 75750	08:52:20	+19 21 03	8.5	B5
18	211996306	HD 71052	08:25:59	+20:11:36	8.5	B9

Appendix B. Table with the Variability Classification

The following table summarizes the results of the photometric analysis for each star observed in K2 Campaigns 13 and 15–18. For each target, we list its final variability classification, and, when relevant, the total number of significant frequencies identified ($N_{freq.}$), as well as the frequency ($\nu_{A_{max}}$) and amplitude (A_{max}) of the dominant mode. The methodologies used for the frequency extraction and classification are detailed in Sections 3 and 5 of the text. The variability class symbols are as follows: SPB for slowly pulsating B-type stars; HYB for stars exhibiting both β Cephei and SPB frequencies; MAIA for Maia variables or fast-rotating SPB stars; ROT and BIN for stars with rotational or binary signatures; EBIN for eclipsing binaries; and SLF for Stochastic Low-Frequency variability. See Section 5 for further details. AP stands for Aperiodic, referring to targets in which no significant variability was detected above our signal-to-noise threshold or which exhibit erratic behavior. Spectral types assigned by us based on blue spectra are marked with a †. Classifications marked with a '?' indicate limited confidence due to ambiguous or marginal signals. The designation 'Instr.?' in Notes is used when the observed variability could plausibly be attributed to instrumental effects.

Table A2. Photometric information for all campaigns.

Camp.	EPIC	Class	N_{tot}	$\nu_{A_{max}}$ (d^{-1})	A_{max} (ppm)	Spectral Type	Notes
13	210650598	SPB	8	2.32	399	B9IV-V †	Instr.?
13	210671425	AP	–	–	–	B8IV †	–
13	210737173	SPB/SLF	8	3.97	–	B9IV-V †	Instr.?
13	210853356	SPB	23	1.06	855	B9V †	–
13	210873575	MAIA	13	1.17	25	B7IV †	–
13	246698204	EBIN	–	–	–	B6V	–
13	246704649	SPB/SLF	23	0.14	–	B9	–
13	246788829	ROT/BIN	–	–	–	B9	–
13	246820783	ROT/BIN	–	–	–	B8	–
13	246968117	SPB?	15	0.29	3.45	B9	–
13	246970807	ROT/BIN	–	–	–	B6IV-V †	–
13	246988320	AP	–	–	–	B9	–
13	247031423	SPB/BIN	45	–	–	B9 IV	–
13	247131891	SPB	24	2.01	174	B8	–
13	247146962	AP	–	–	–	B8	–
13	247147343	ROT/BIN	–	–	–	B9	–
13	247147476	SPB/SLF?	15	–	–	B8	–
13	247148453	SPB/SLF	11	2.78	–	B5	–
13	247153152	SPB/SLF	20	1.35	68	B9	–
13	247160983	SPB/SLF	19	1.90	–	B8	–
13	247164195	SPB/SLF	18	1.20	–	B9II	–
13	247169375	ROT/BIN	–	–	–	B	Spots
13	247192878	ROT/BIN	–	–	–	B5	–
13	247211157	MAIA/SLF	24	0.12	–	B9-A0V †	–
13	247234723	SPB/SLF	61	3.50	–	B3V †	–
13	247264203	SPB/SLF	54	0.90	–	B8	–
13	247273628	MAIA	96	2.00	–	B9	–
13	247278704	ROT/BIN	–	–	–	B9	–
13	247430338	SPB/BIN?	86	–	–	B3V	–

Table A2. *Cont.*

Camp.	EPIC	Class	N_{tot}	$\nu_{A_{max}}$ (d^{-1})	A_{max} (ppm)	Spectral Type	Notes
13	247457814	ROT/BIN	–	–	–	B9	–
13	247495377	ROT/BIN	–	1.73	4630	B5V †	–
13	247551785	ROT/BIN	–	–	–	B9	–
13	247554799	MAIA	130	–	–	B8	–
13	247559520	ROT/BIN	–	–	–	B9	–
13	247612547	EBIN	–	–	–	B5V †	–
13	247682580	MAIA/SLF	14	–	–	B9V †	–
13	247688426	ROT/BIN	–	–	–	B5III	–
13	247692420	AP	–	–	–	B9	–
13	247695418	ROT/BIN	–	–	–	B8IV †	–
13	247696147	MAIA/SLF	16	–	–	B9V †	–
13	247698073	ROT/BIN	–	–	–	B9	–
13	247705729	SPB/SLF	13	2.14	105	B9	–
13	247709560	ROT/BIN/SLF	–	–	–	B9	–
13	247714018	ROT/BIN/SLF	–	–	–	B9	–
13	247714396	SPB	9	2.22	33	B9	–
13	247742016	SPB/SLF	20	1.40	–	B8	–
13	247757517	SPB	11	2.00	62	B9V †	–
13	247759652	ROT/BIN	–	–	–	B9V †	–
13	247774959	ROT/BIN	–	–	–	B9II-III †	Spots
13	247786632	MAIA	23	–	–	B9	–
13	247806245	MAIA	131	–	–	B8	–
13	247889905	SPB	14	1.98	48	B9	–
13	247895553	MAIA	82	–	–	B9	–
13	247935687	SLF	7	0.25	22	B9	–
13	248064520	SPB	57	2.33	4140	B9	–
13	248150769	SPB	65	0.98	964	B8	–
13	248227339	SPB/SLF	77	0.42	1104	B9	–
15	204525956	AP	–	–	–	B9 V †	–
15	204848812	SPB	3	1.16	24	B9 V †	
15	249135451	SPB	30	0.68	50,400	B6 V †	–
15	249481830	ROT/BIN	–	–	–	B9 V	–
15	249661590	AP	–	–	–	A0 V †	–
15	249811956	EBIN	–	–	–	B7 V †	–
15	249919216	AP	–	–	–	B9 V †	–
15	250131922	SPB	29	0.33	576	B5 V †	–
17	212431975	SPB	23	1.78	986	B4	–
17	212450527	SPB	19	0.73	90	B7	–
17	212744655	SPB	48	0.82	1280	B5 V †	–
17	251547357	HYB	17	3.69	199	B2 V †	–
18	211404031	AP	–	–	–	B9 V †	–
18	211712203	SLF	4	0.23	857	B9 V †	–
18	211941698	SPB/SLF	10	1.03	11,300	B5 III †	–
18	211996306	SPB	2	0.63	1850	B9 III †	–

Appendix C. Examples of Monte Carlo Distributions of Atmospheric Parameters

The uncertainties of the stellar atmospheric parameters were estimated using a Monte Carlo approach. Since the formal errors from χ^2 minimization in `sme` tend to underestimate the correct values, we generated 100 realizations for each star by randomly perturbing the

best-fit parameters within a 5% range. The final parameter values correspond to the robust mean of these distributions, and the 1σ scatter provides the adopted uncertainties. This method yields a more realistic estimate by accounting for local parameter-space variations and possible degeneracies.

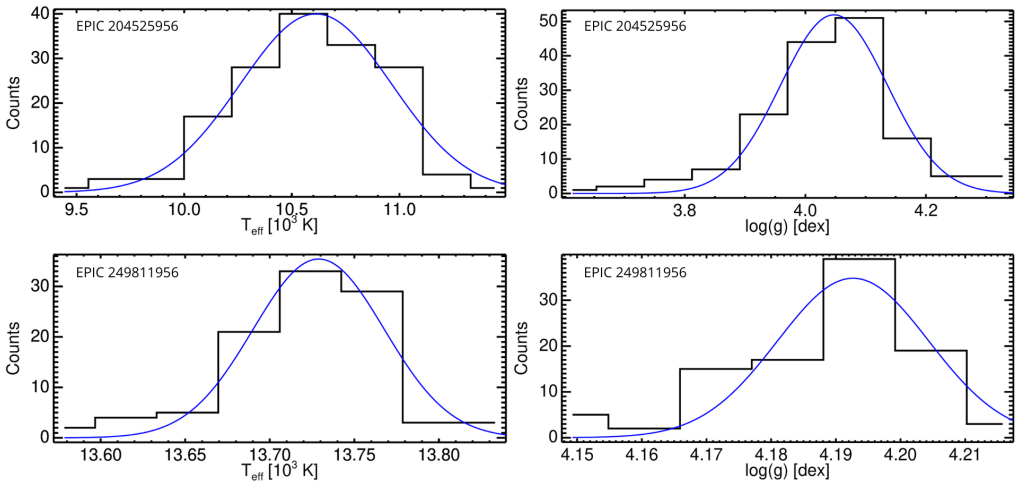


Figure A1. Monte Carlo distributions of the stellar atmospheric parameters for EPIC 204525956—obtained from χ^2 minimization with `sme`—used to estimate the associated uncertainties.

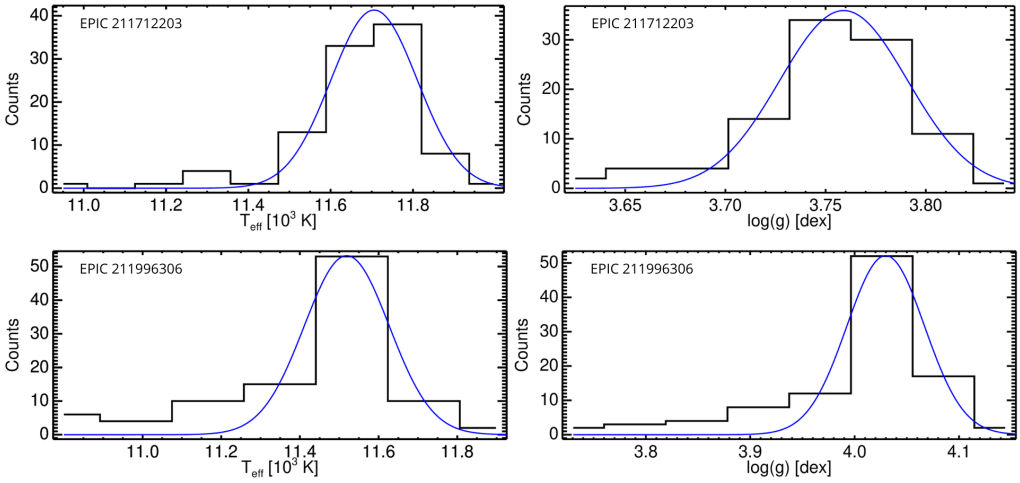


Figure A2. Monte Carlo distributions of the stellar atmospheric parameters for EPIC 211712203—obtained from χ^2 minimization with `sme`—used to estimate the associated uncertainties.

Appendix D. Light Curves and Frequency Spectra

The upper panel displays the light curve of the star, which is identified by its EPIC number. The middle panel shows the frequency spectrum of the star, with the blue line derived from the `cleanest` algorithm [27], while red triangles and dashed lines mark significant frequencies ($S/N \geq 5$) identified using the IVS-KULeuven iterative prewhitening routine [28]. The lower panel presents the wavelet transform of the light curve.

Appendix D.1. SPB

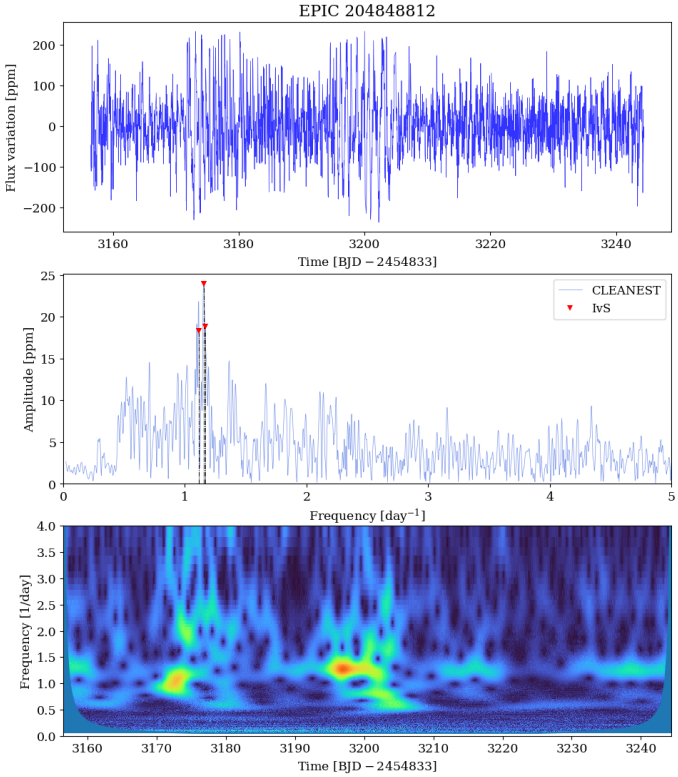


Figure A3. K2 light curve and frequency spectrum of EPIC 204848812, observed during Campaign 15. We classify this star as "SPB".

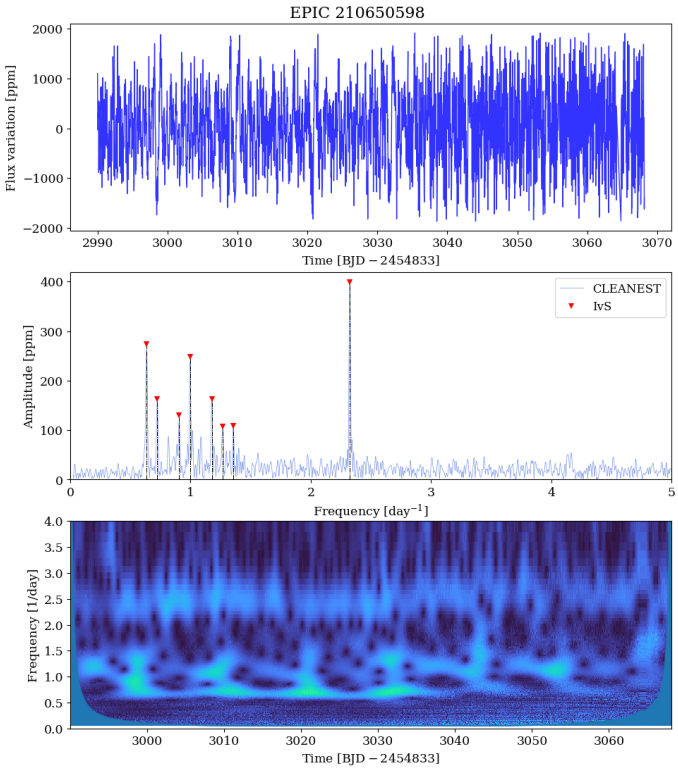


Figure A4. K2 light curve and frequency spectrum of EPIC 210650598 observed during Campaign 13. We classify this star as "SPB".

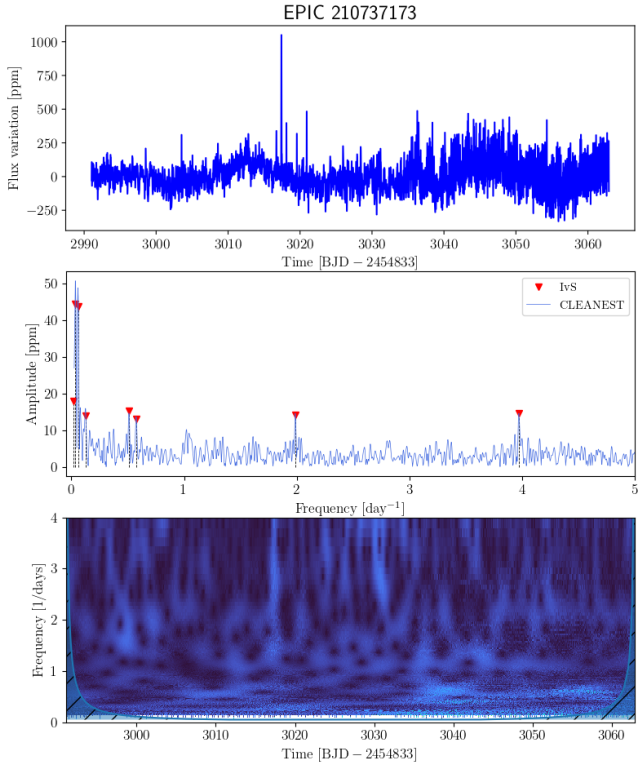


Figure A5. K2 light curve and frequency spectrum of EPIC 210737173 observed during Campaign 13. We classify this star as "SPB/SLF".

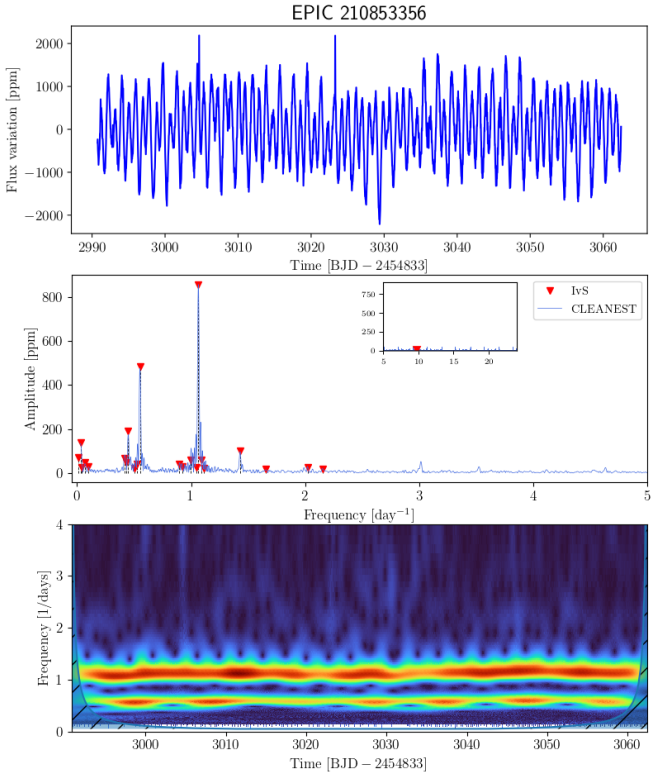


Figure A6. K2 light curve and frequency spectrum of EPIC 210853356 observed during Campaign 13. We classify this star as "SPB".

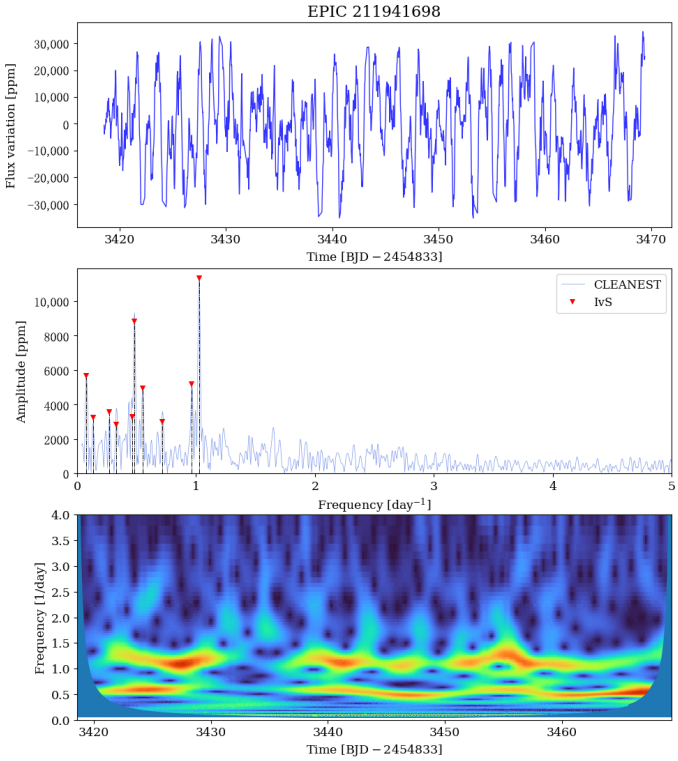


Figure A7. K2 light curve and frequency spectrum of EPIC 211941698 observed during Campaign 18. We classify this star as "SPB/SLF".

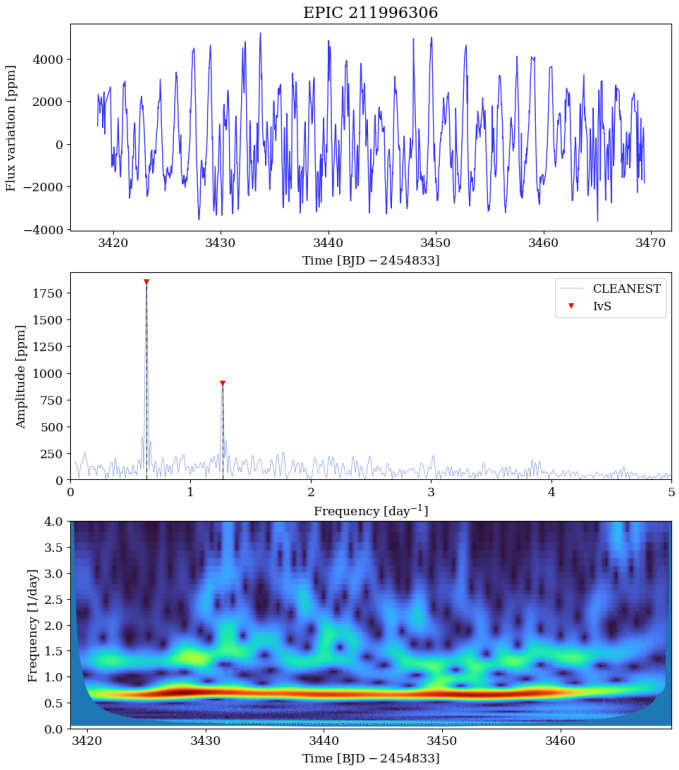


Figure A8. K2 light curve and frequency spectrum of EPIC 211996306 observed during Campaign 18. We classify this star as "SPB".

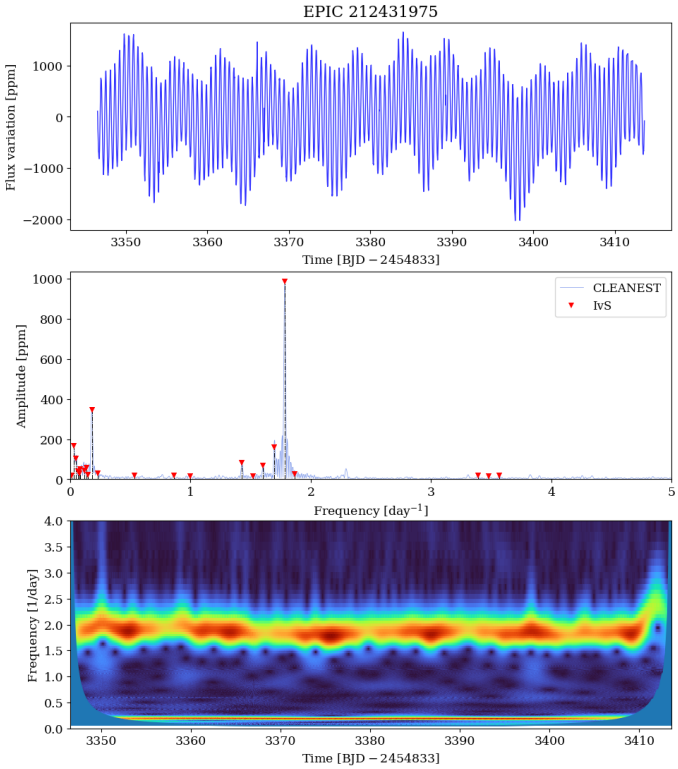


Figure A9. K2 light curve and frequency spectrum of EPIC 212431975 observed during Campaign 17. We classify this star as "SPB".

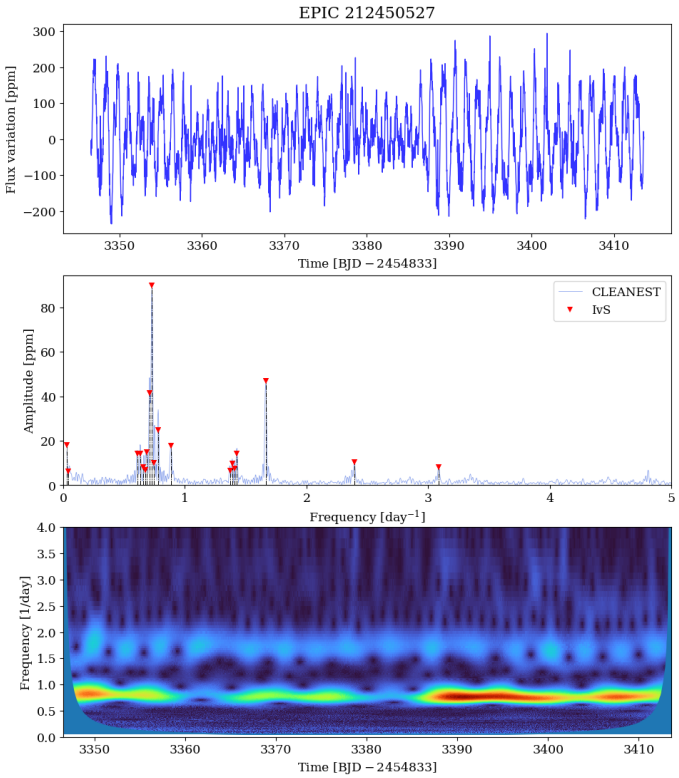


Figure A10. K2 light curve and frequency spectrum of EPIC 212450527 observed during Campaign 17. We classify this star as "SPB".

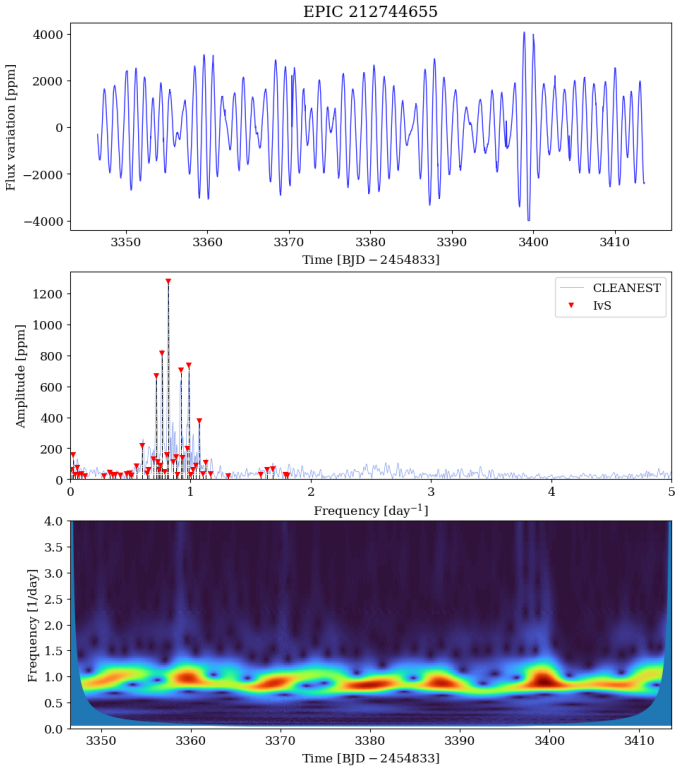


Figure A11. K2 light curve and frequency spectrum of EPIC 212744655 observed during Campaign 17. We classify this star as "SPB".

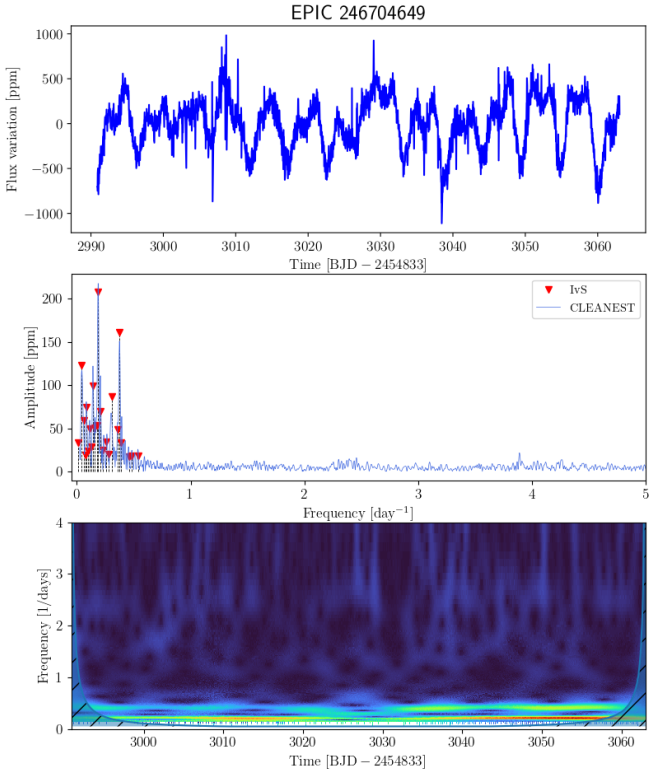


Figure A12. K2 light curve and frequency spectrum of EPIC 246704649 observed during Campaign 13. We classify this star as "SPB/SLF".

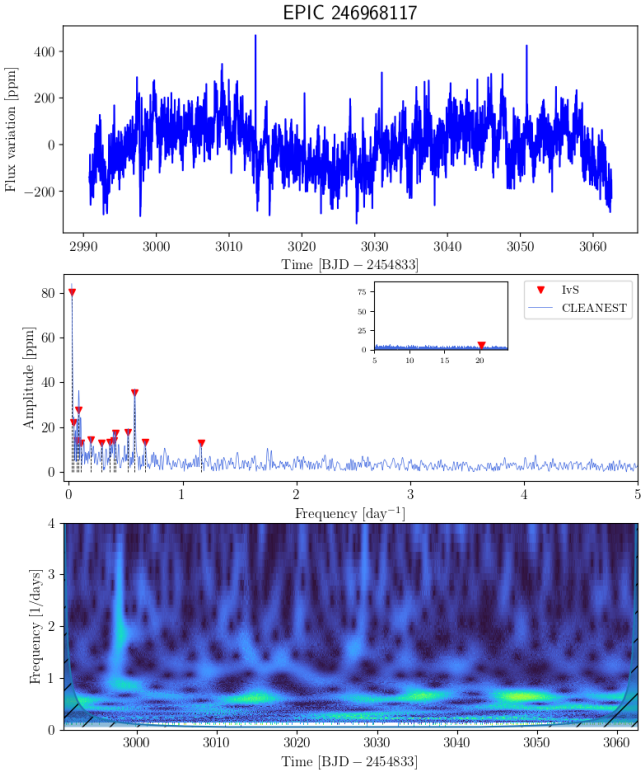


Figure A13. K2 light curve and frequency spectrum of EPIC 246968117 observed during Campaign 13. We classify this star as "SPB?".

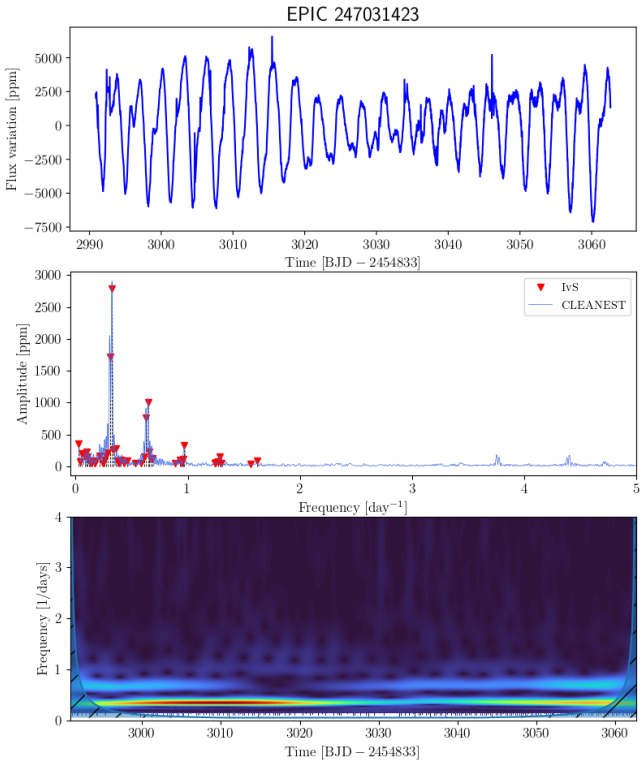


Figure A14. K2 light curve and frequency spectrum of EPIC 247031423 observed during Campaign 13. We classify this star as "SPB/BIN".

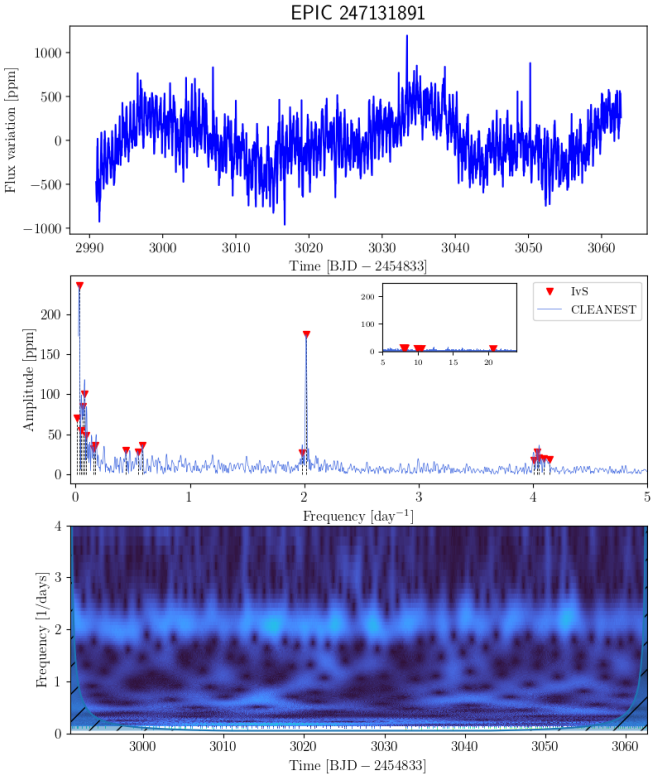


Figure A15. K2 light curve and frequency spectrum of EPIC 247131891 observed during Campaign 13. We classify this star as "SPB".

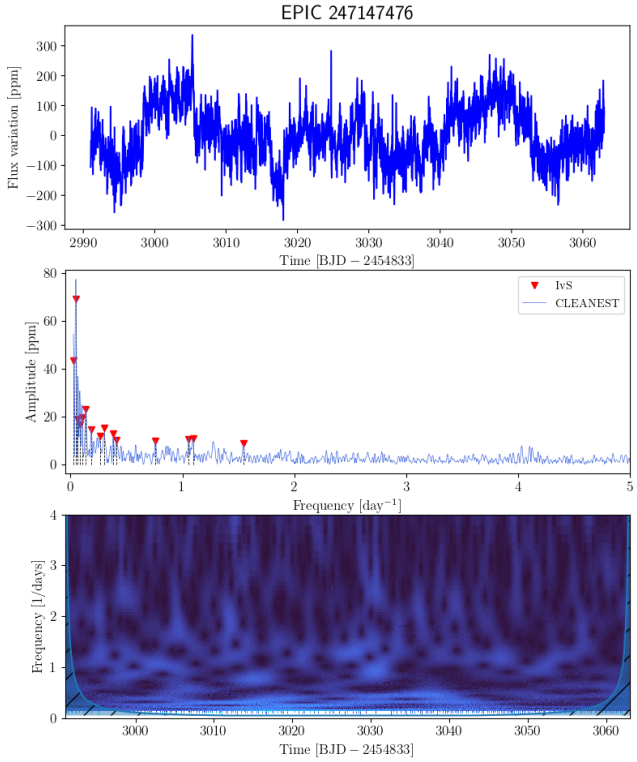


Figure A16. K2 light curve and frequency spectrum of EPIC 247147476 observed during Campaign 13. We classify this star as "SPB/SLF?".

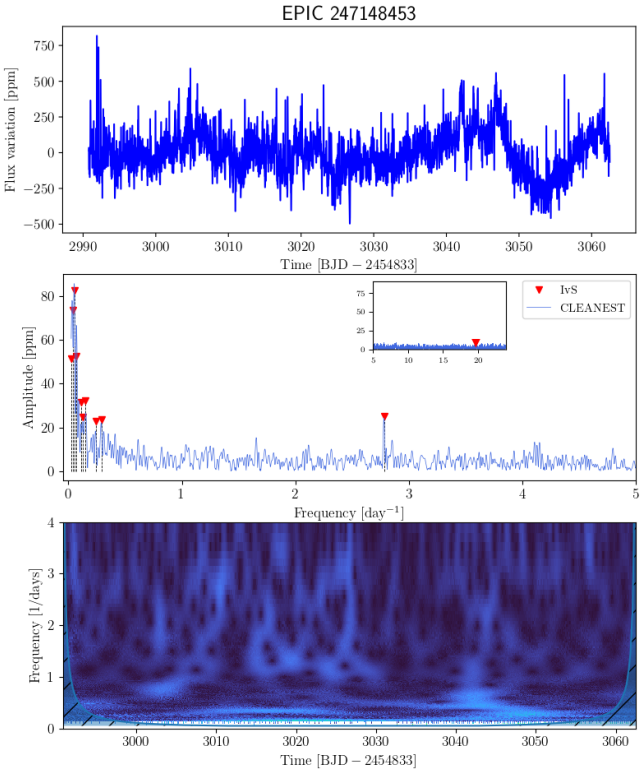


Figure A17. K2 light curve and frequency spectrum of EPIC 247148453 observed during Campaign 13. We classify this star as "SPB/SLF".

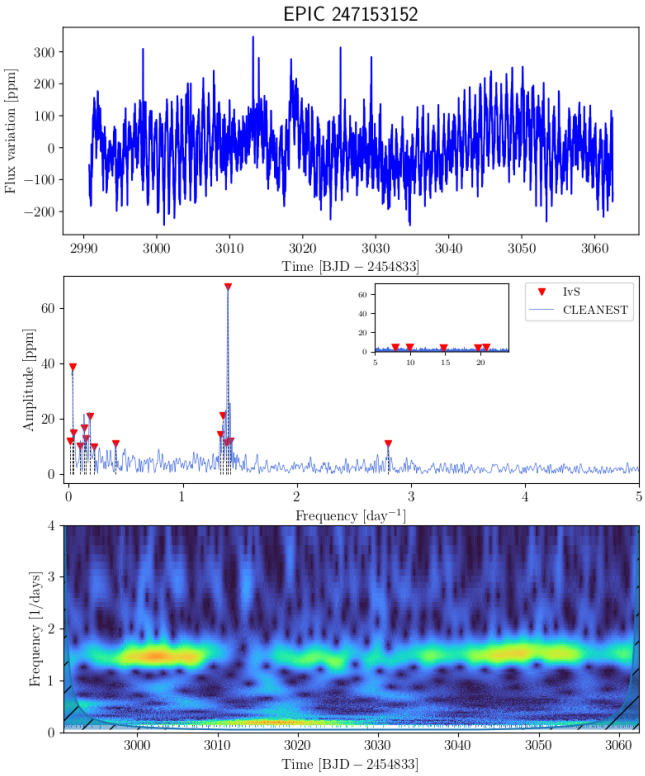


Figure A18. K2 light curve and frequency spectrum of EPIC 247153152 observed during Campaign 13. We classify this star as "SPB/SLF".

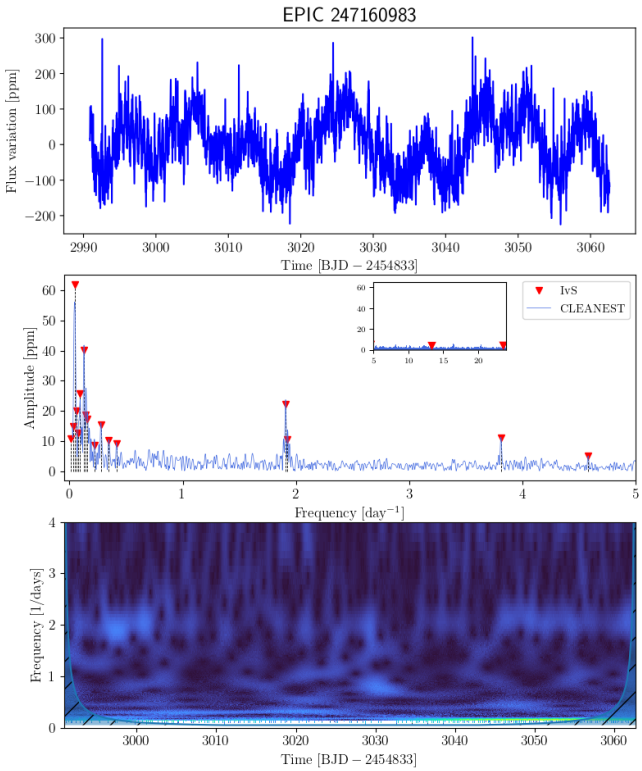


Figure A19. K2 light curve and frequency spectrum of EPIC 247160983 observed during Campaign 13. We classify this star as "SPB/SLF".

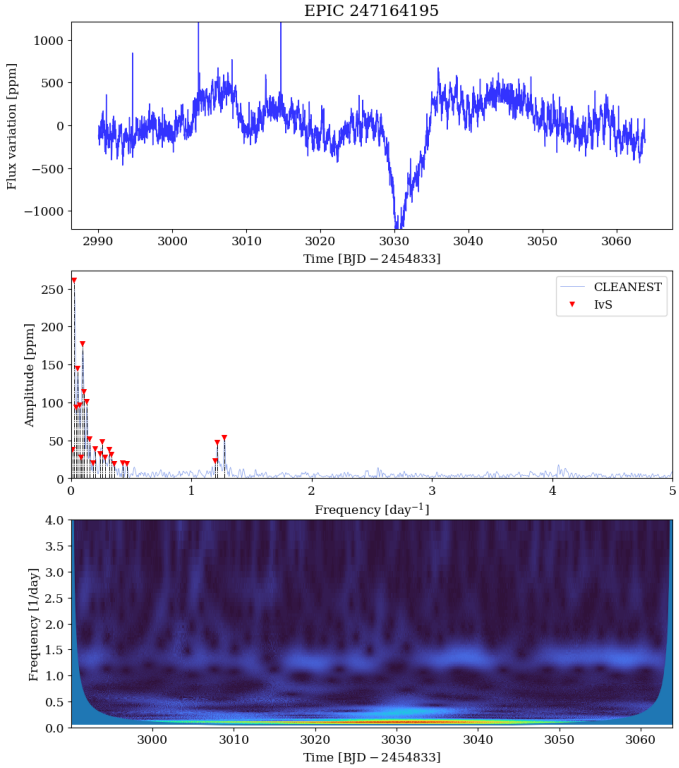


Figure A20. K2 light curve and frequency spectrum of EPIC 247164195 observed during Campaign 13. We classify this star as "SPB/SLF".

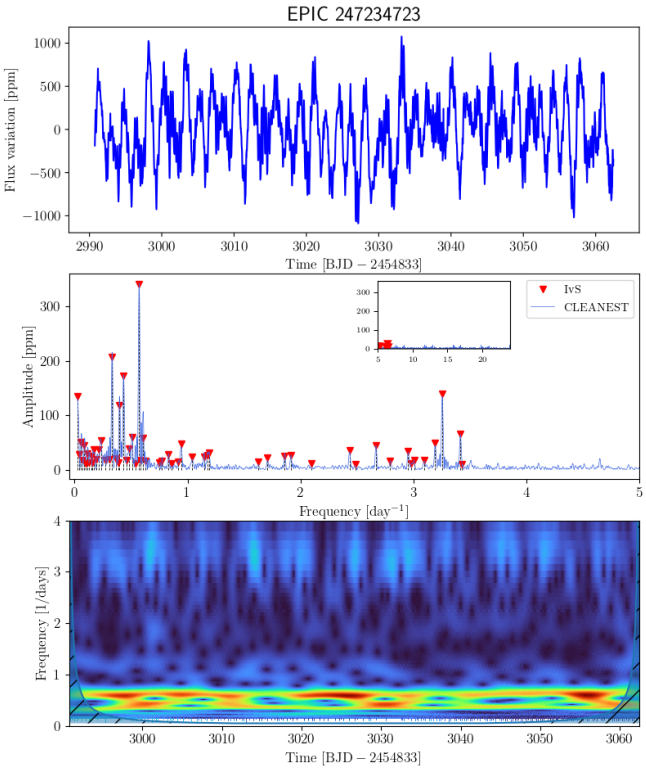


Figure A21. K2 light curve and frequency spectrum of EPIC 247234723 observed during Campaign 13. We classify this star as "SPB/SLF".

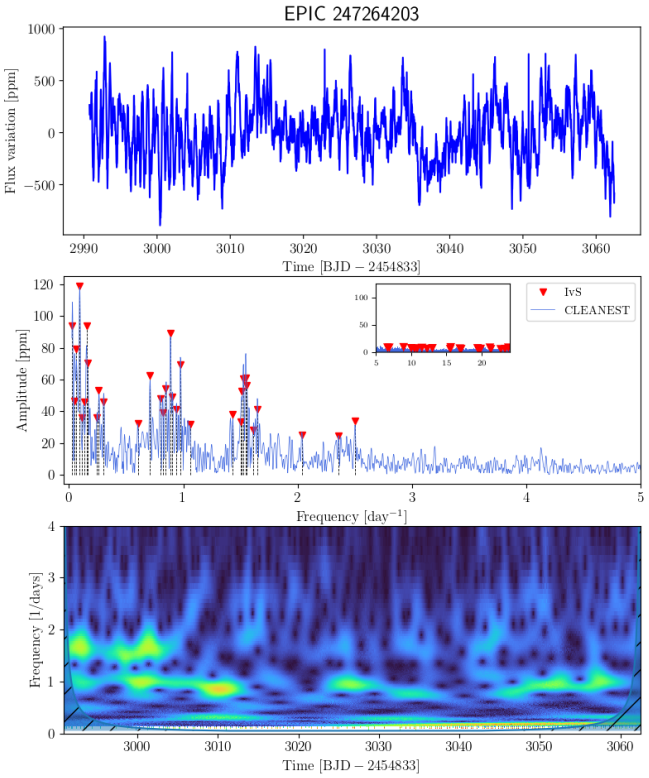


Figure A22. K2 light curve and frequency spectrum of EPIC 247264203 observed during Campaign 13. We classify this star as "SPB/SLF".

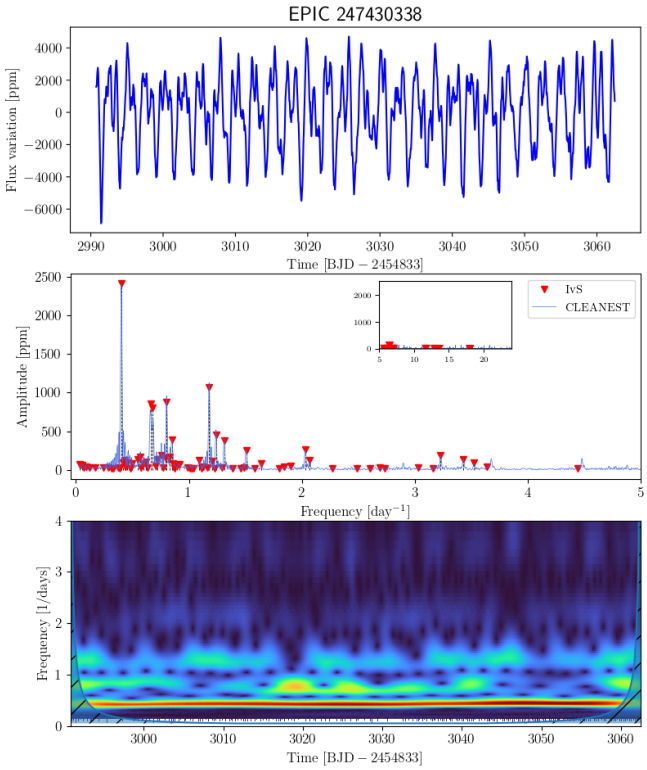


Figure A23. K2 light curve and frequency spectrum of EPIC 247430338 observed during Campaign 13. We classify this star as "SPB/BIN?".

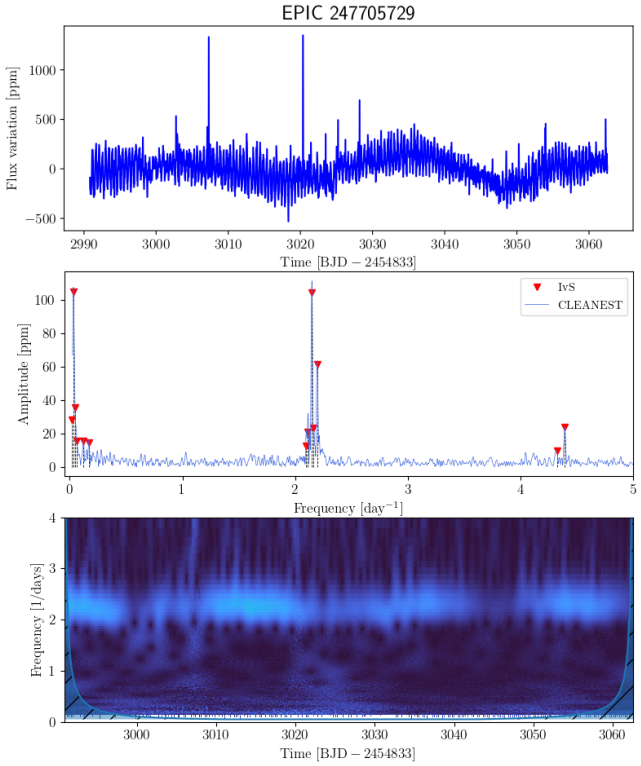


Figure A24. K2 light curve and frequency spectrum of EPIC 247705729 observed during Campaign 13. We classify this star as "SPB/SLF".

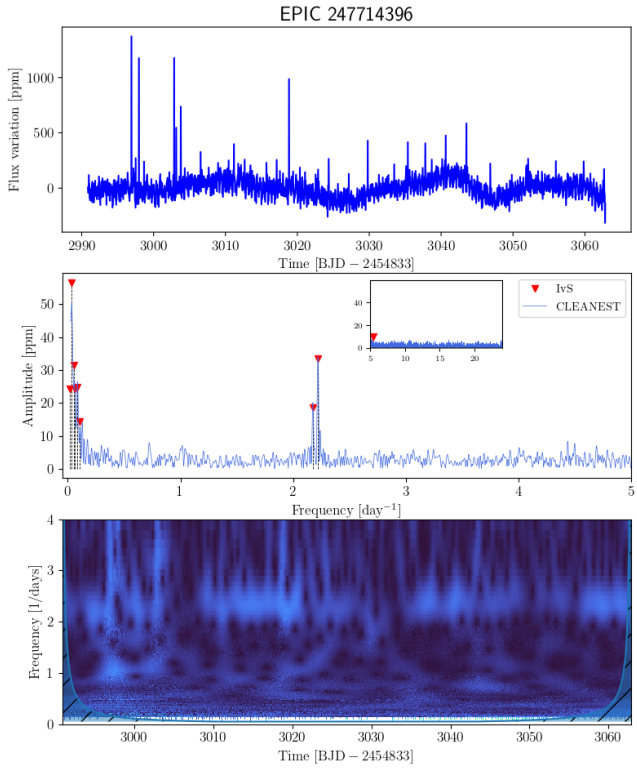


Figure A25. K2 light curve and frequency spectrum of EPIC 247714396 observed during Campaign 13. We classify this star as "SPB".

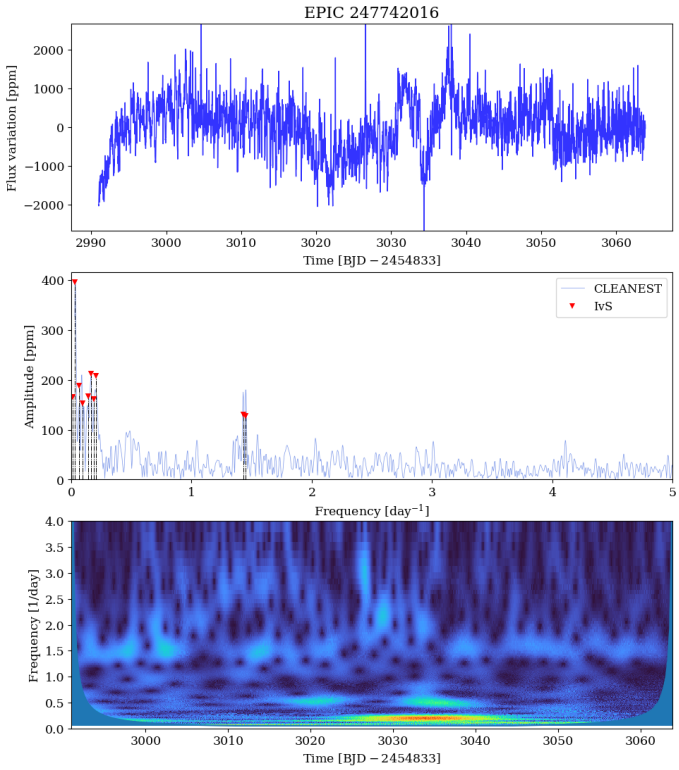


Figure A26. K2 light curve and frequency spectrum of EPIC 247742016 observed during Campaign 13. We classify this star as "SPB/SLF".

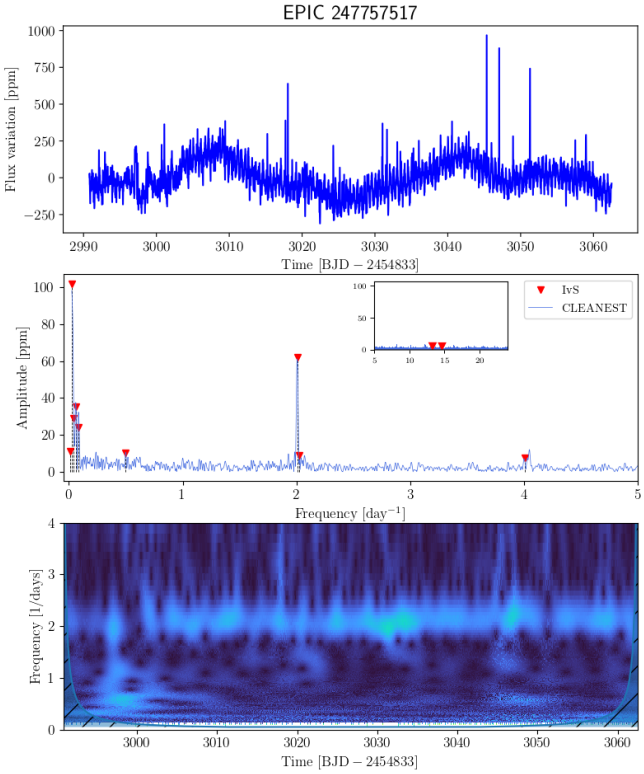


Figure A27. K2 light curve and frequency spectrum of EPIC 247757517 observed during Campaign 13. We classify this star as "SPB".

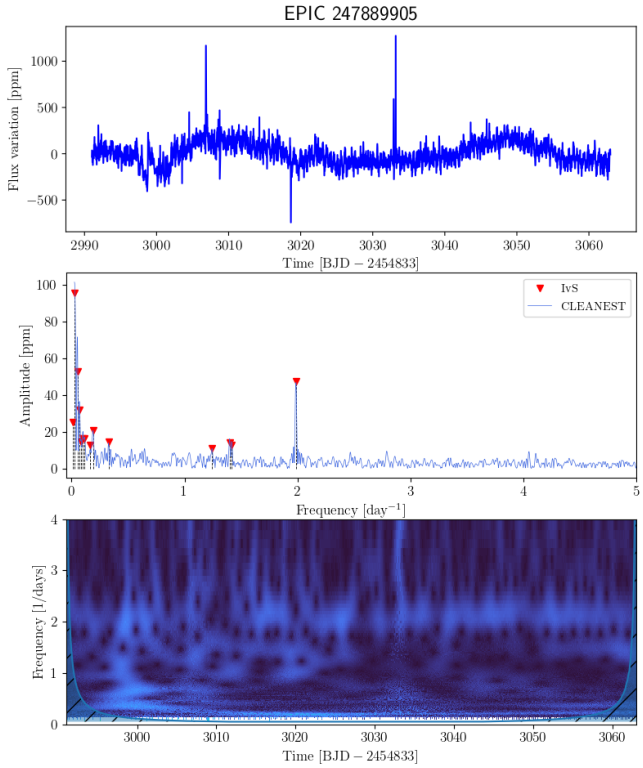


Figure A28. K2 light curve and frequency spectrum of EPIC 247889905 observed during Campaign 13. We classify this star as "SPB".

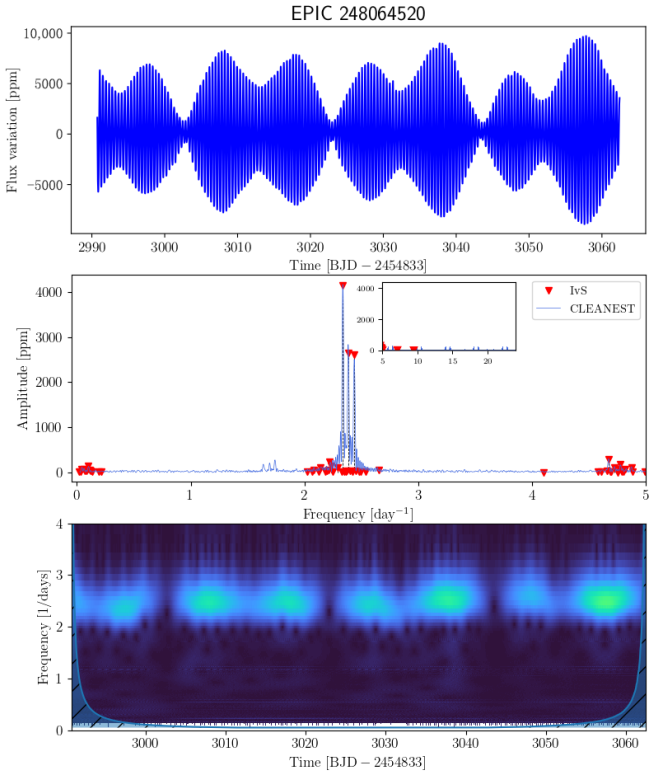


Figure A29. K2 light curve and frequency spectrum of EPIC 248064520 observed during Campaign 13. We classify this star as "SPB".

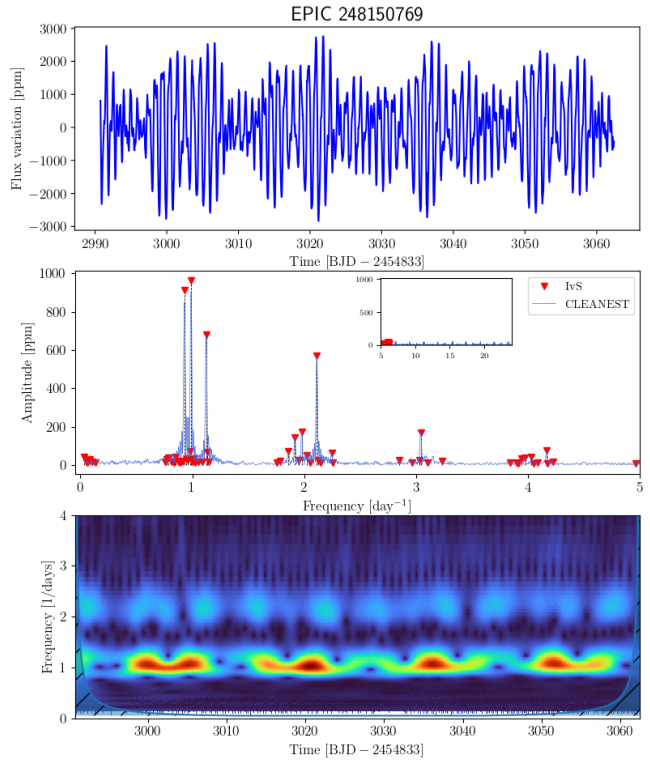


Figure A30. K2 light curve and frequency spectrum of EPIC 248150769 observed during Campaign 13. We classify this star as "SPB".

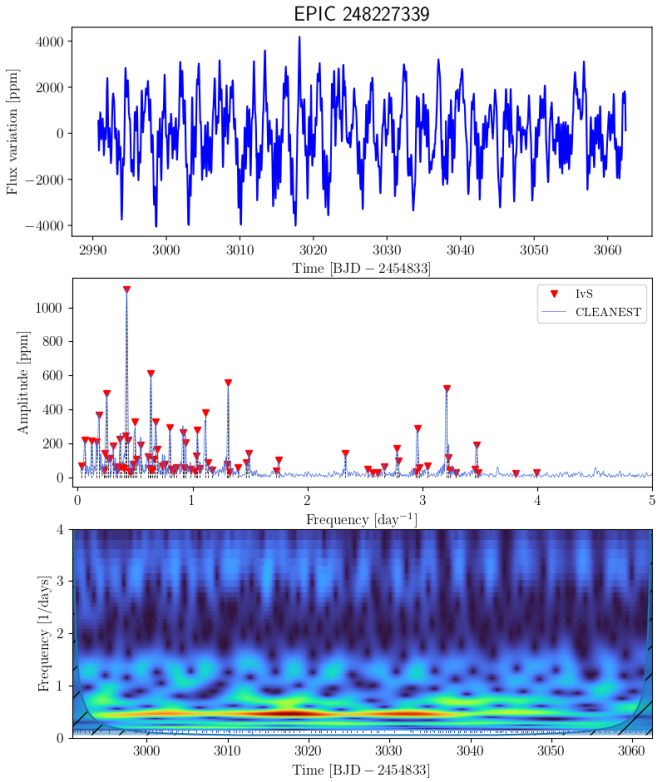


Figure A31. K2 light curve and frequency spectrum of EPIC 248227339 observed during Campaign 13. We classify this star as "SPB/SLF".

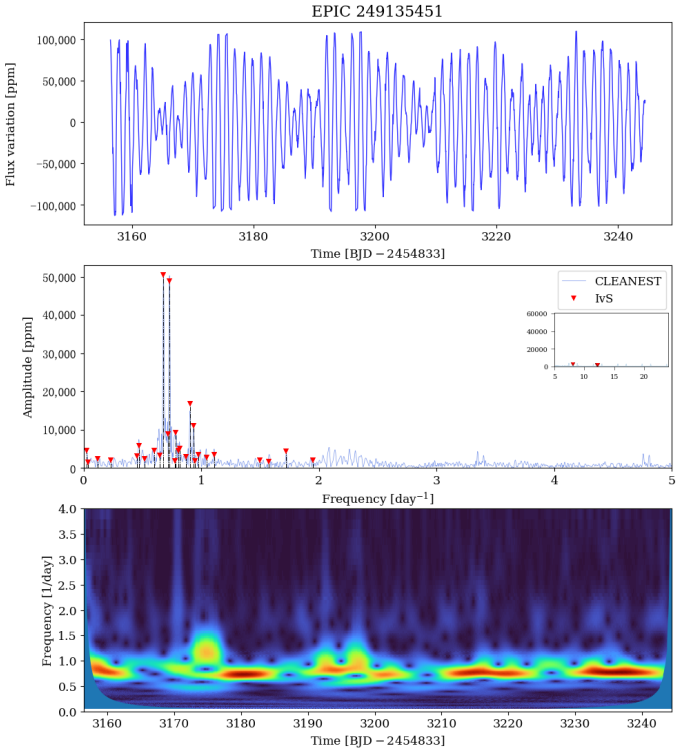


Figure A32. K2 light curve and frequency spectrum of EPIC 249135451 observed during Campaign 15. We classify this star as "SPB".

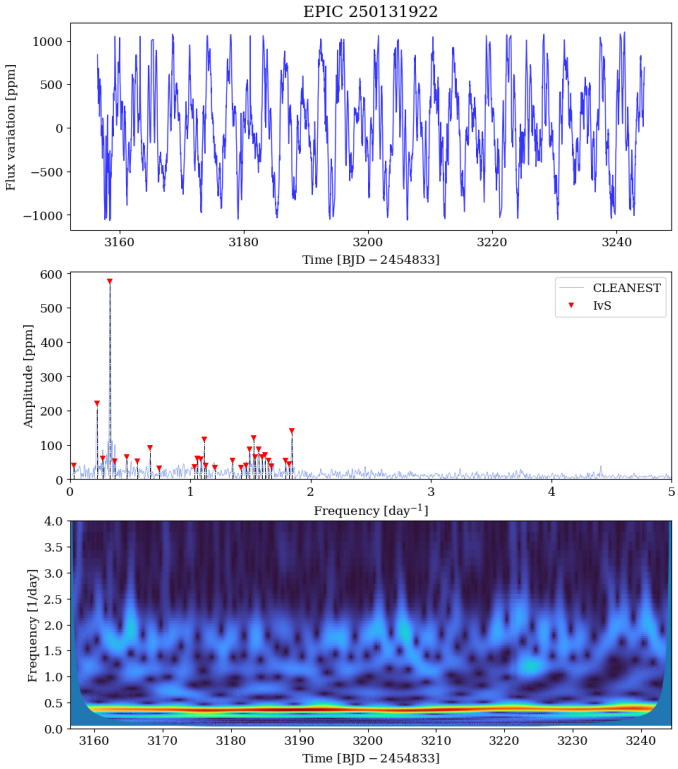


Figure A33. K2 light curve and frequency spectrum of EPIC 250131922 observed during Campaign 15. We classify this star as "SPB".

Appendix D.2. MAIA

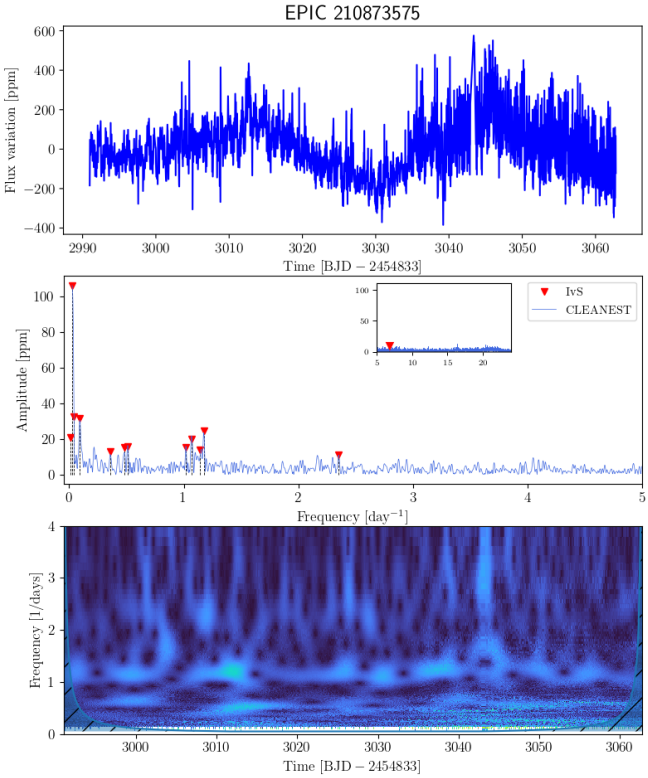


Figure A34. K2 light curve and frequency spectrum of EPIC 210873575 observed during Campaign 13. We classify this star as "MAIA".

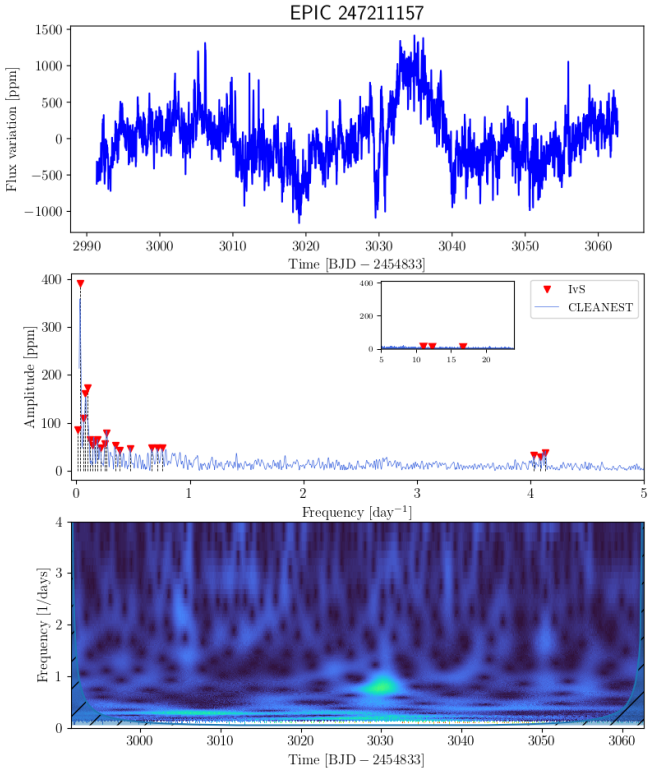


Figure A35. K2 light curve and frequency spectrum of EPIC 247211157 observed during Campaign 13. We classify this star as "MAIA/SLF".

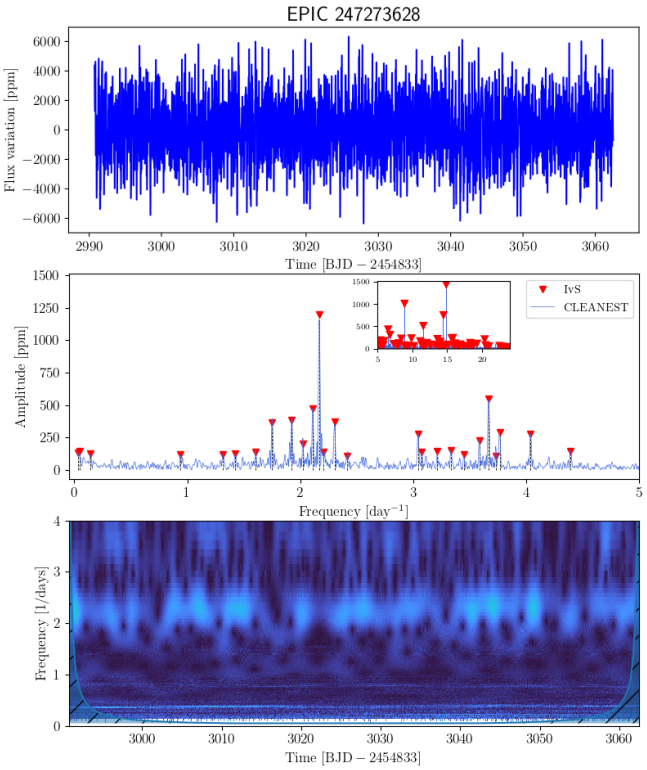


Figure A36. K2 light curve and frequency spectrum of EPIC 247273628 observed during Campaign 13. We classify this star as "MAIA".

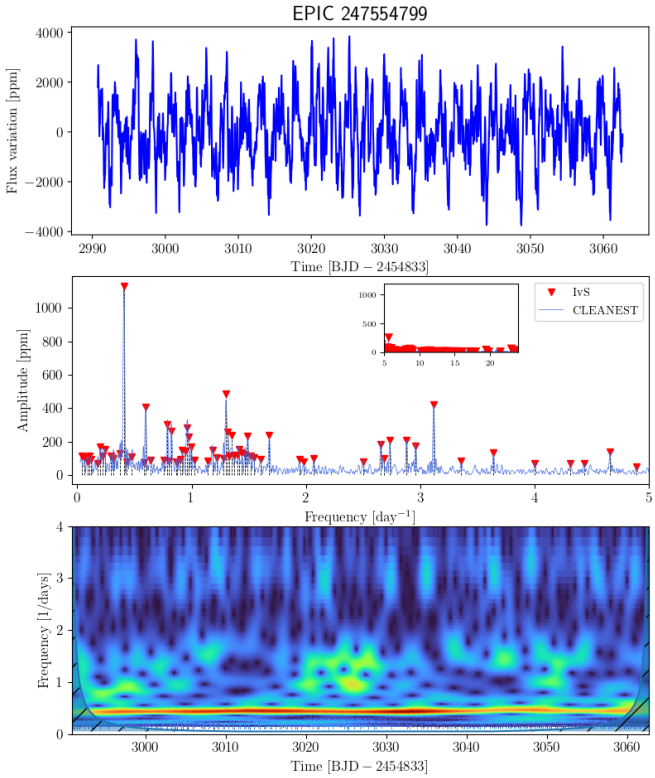


Figure A37. K2 light curve and frequency spectrum of EPIC 247554799 observed during Campaign 13. We classify this star as "MAIA".

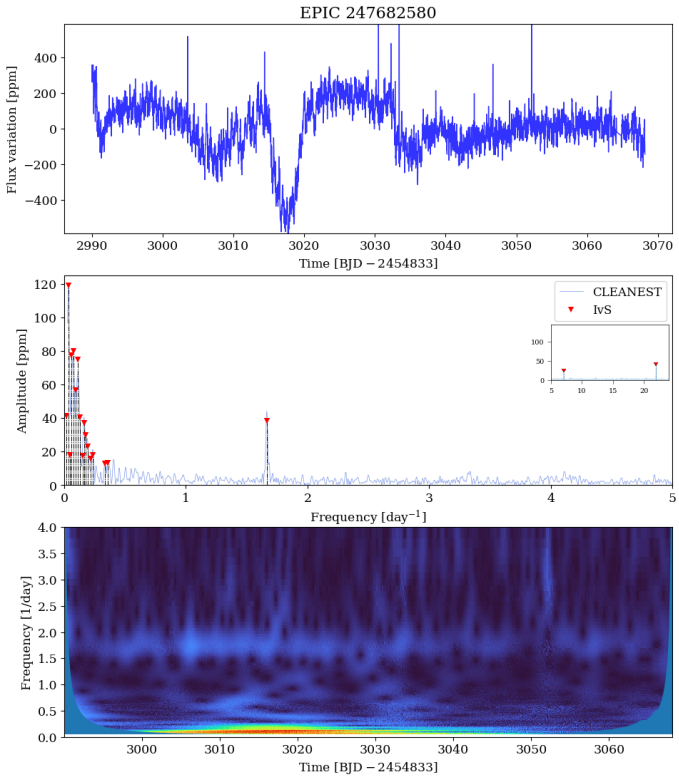


Figure A38. K2 light curve and frequency spectrum of EPIC 247682580 observed during Campaign 13. We classify this star as "MAIA/SLF".

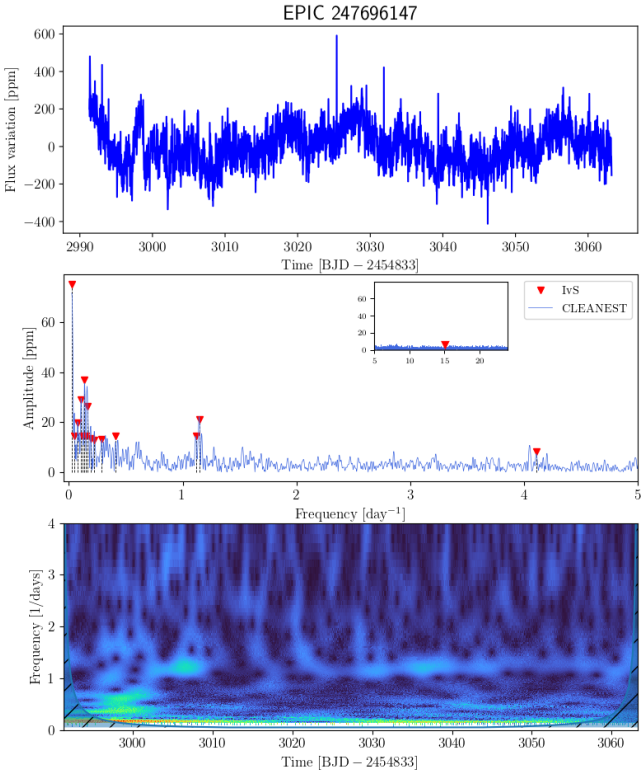


Figure A39. K2 light curve and frequency spectrum of EPIC 247696147 observed during Campaign 13. We classify this star as "MAIA/SLF".

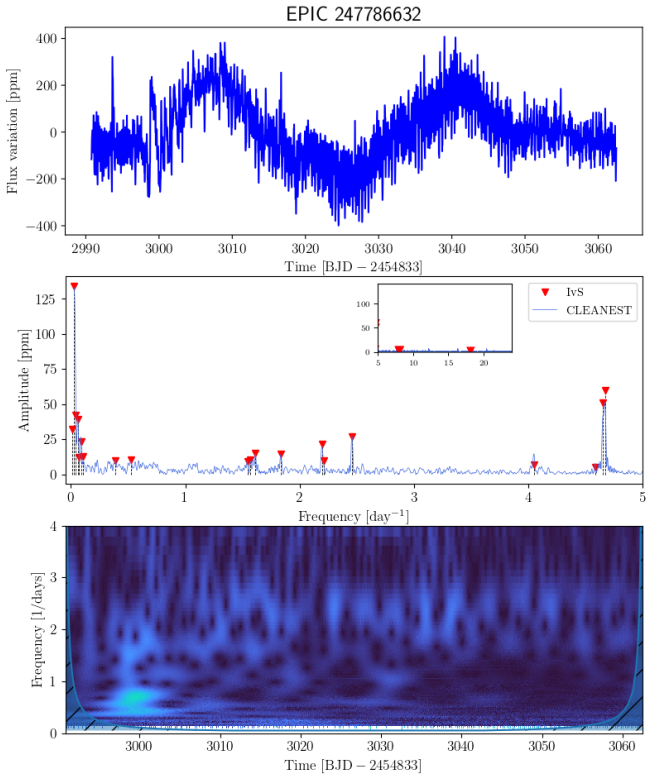


Figure A40. K2 light curve and frequency spectrum of EPIC 247786632 observed during Campaign 13. We classify this star as "MAIA".

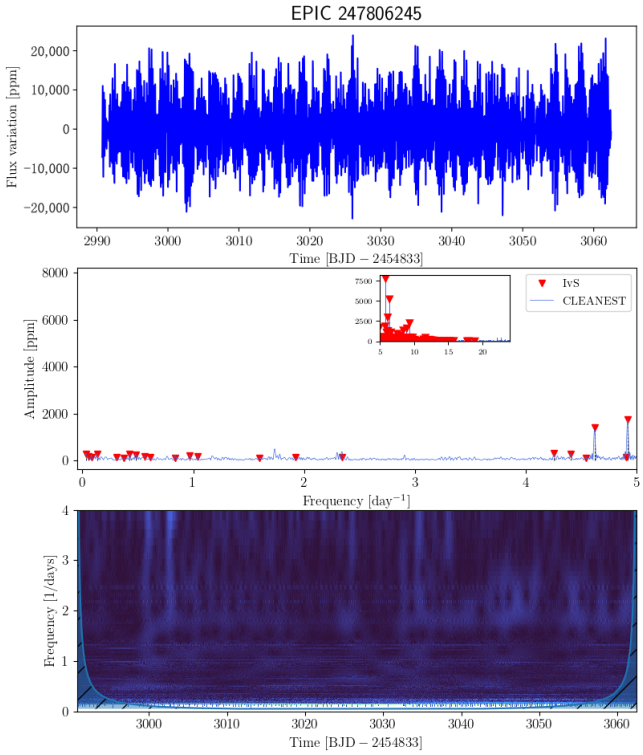


Figure A41. K2 light curve and frequency spectrum of EPIC 247806245 observed during Campaign 13. We classify this star as "MAIA".

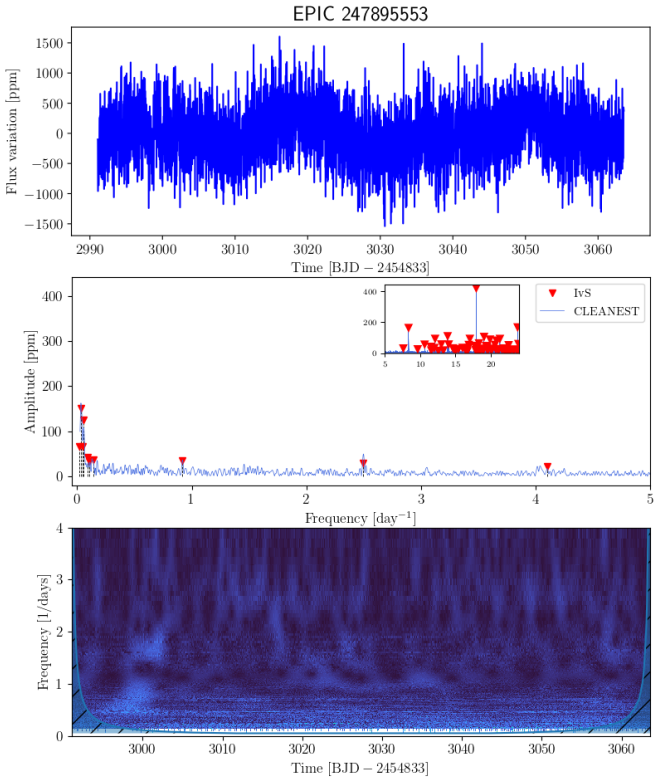


Figure A42. K2 light curve and frequency spectrum of EPIC 247895553 observed during Campaign 13. We classify this star as "MAIA".

Appendix D.3. AP

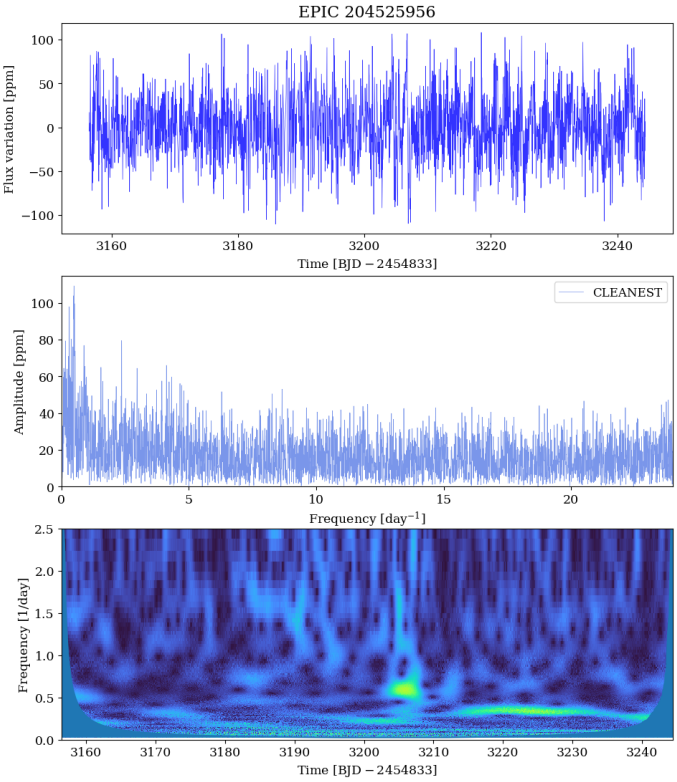


Figure A43. K2 light curve and frequency spectrum of EPIC 204525956 observed during Campaign 15. We classify this star as "AP".

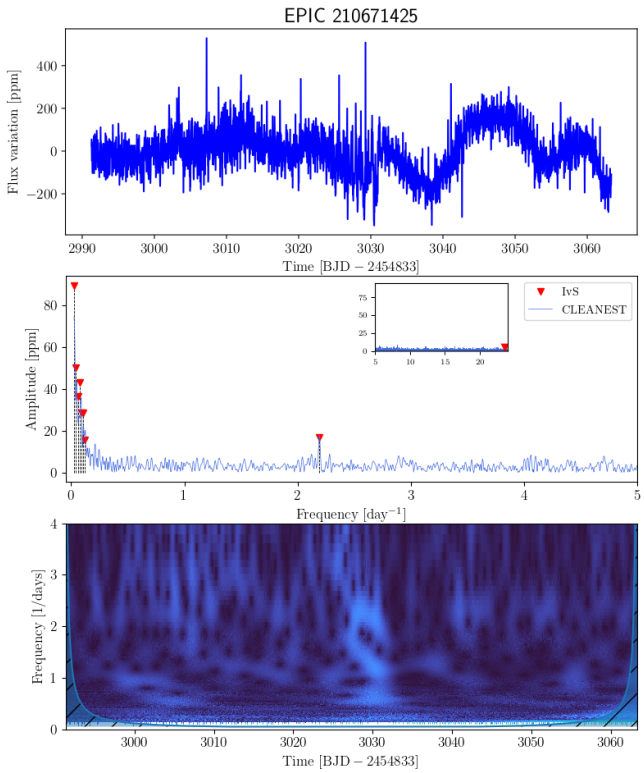


Figure A44. K2 light curve and frequency spectrum of EPIC 210671425 observed during Campaign 13. We classify this star as "AP".

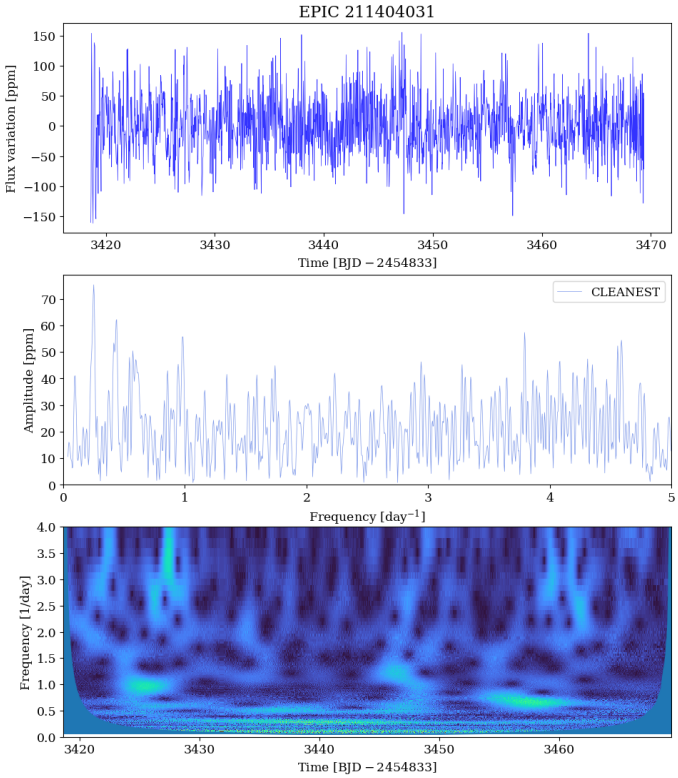


Figure A45. K2 light curve and frequency spectrum of EPIC 211404031 observed during Campaign 18. We classify this star as "AP".

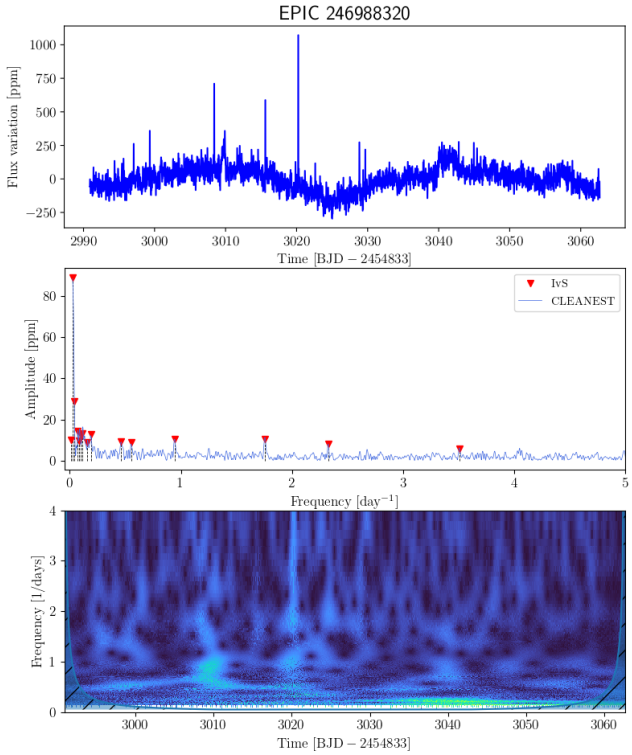


Figure A46. K2 light curve and frequency spectrum of EPIC 246988320 observed during Campaign 13. We classify this star as "AP".

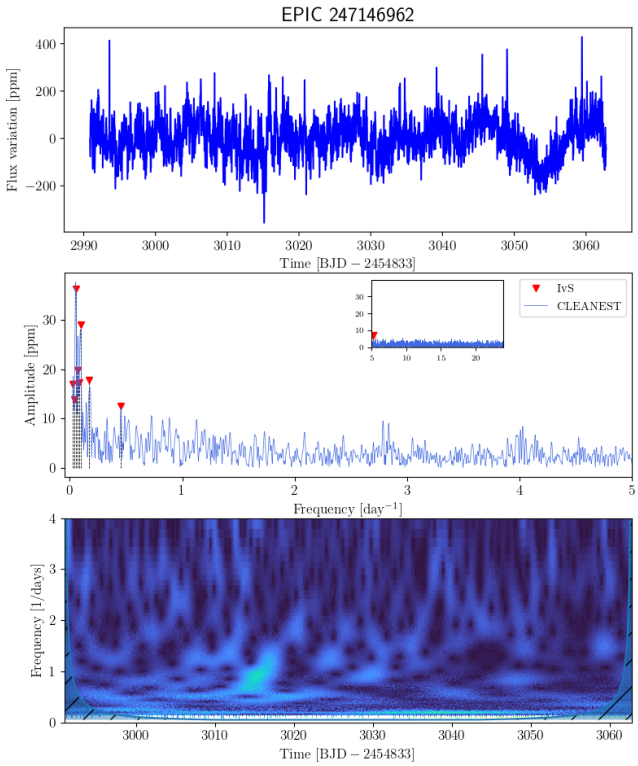


Figure A47. K2 light curve and frequency spectrum of EPIC 247146962 observed during Campaign 13. We classify this star as "AP".

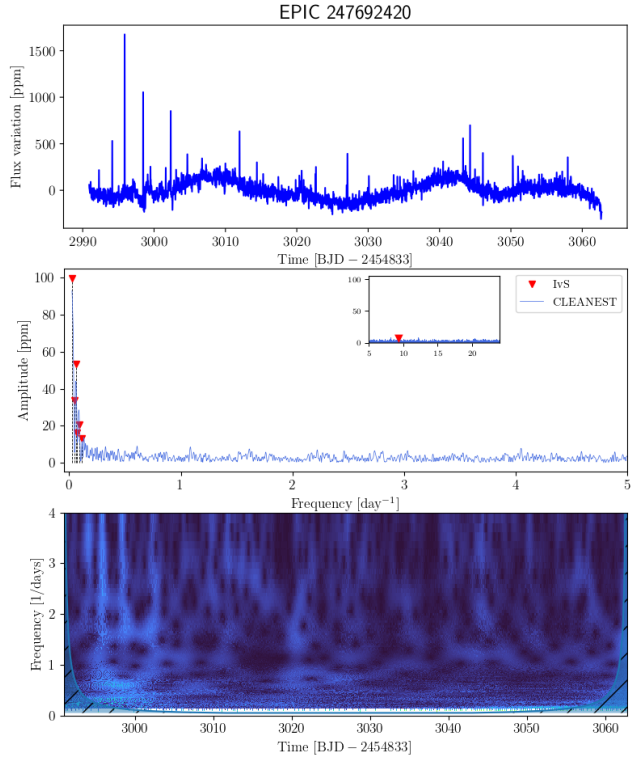


Figure A48. K2 light curve and frequency spectrum of EPIC 247692420 observed during Campaign 13. We classify this star as "AP".

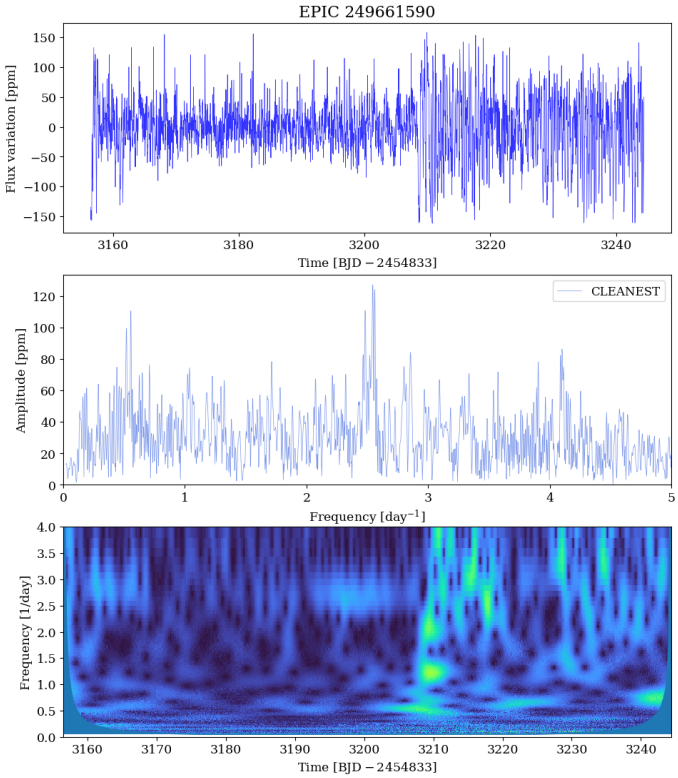


Figure A49. K2 light curve and frequency spectrum of EPIC 249661590 observed during Campaign 15. We classify this star as "AP".

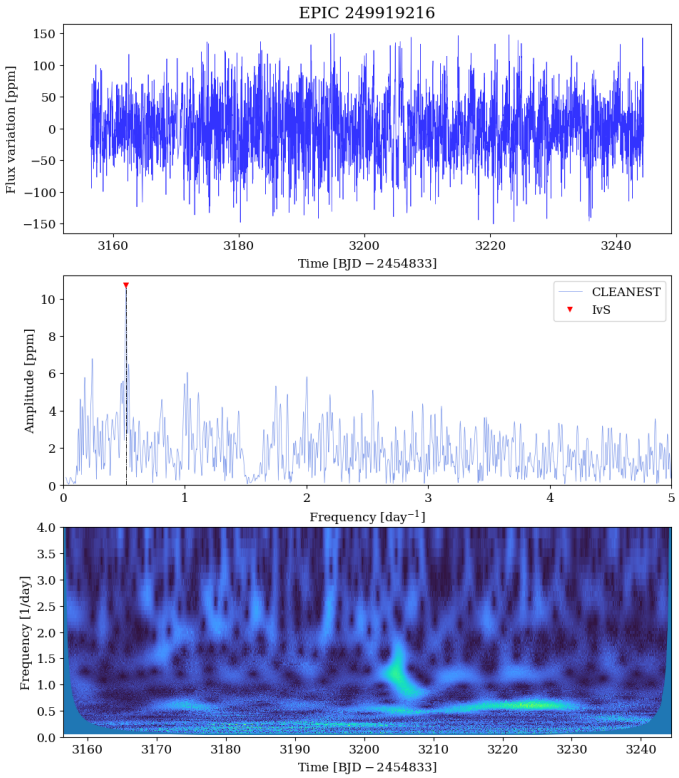


Figure A50. K2 light curve and frequency spectrum of EPIC 249919216 observed during Campaign 15. We classify this star as "AP".

Appendix D.4. SLF

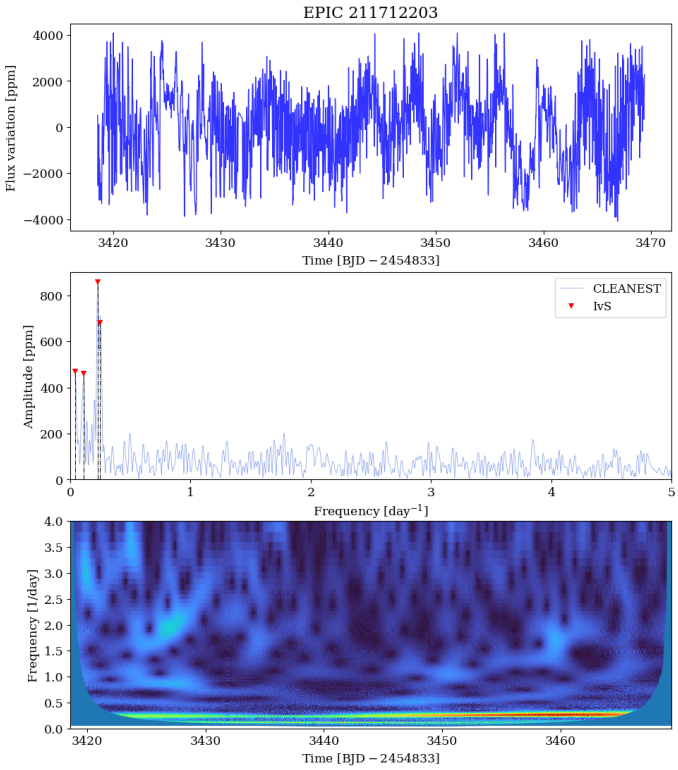


Figure A51. K2 light curve and frequency spectrum of EPIC 211712203 observed during Campaign 18. We classify this star as "SLF".

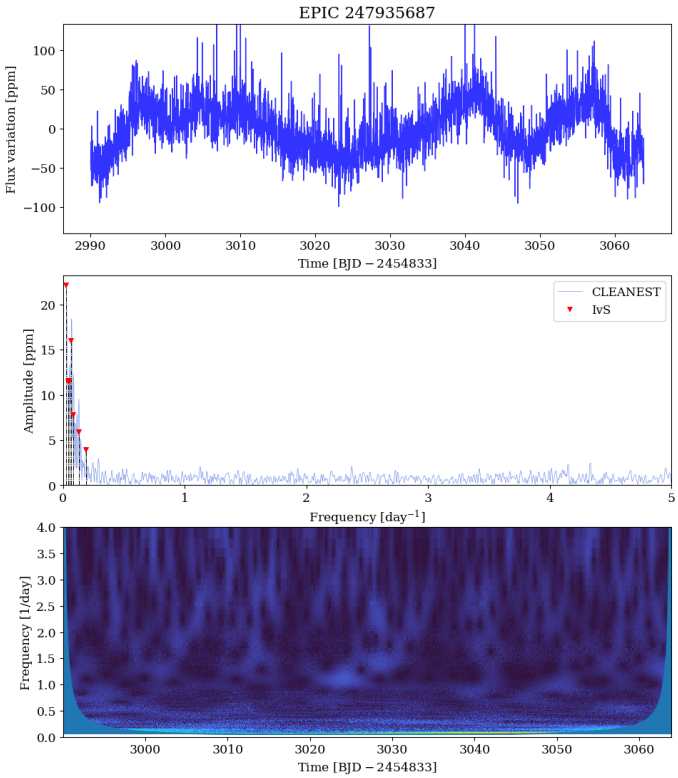


Figure A52. K2 light curve and frequency spectrum of EPIC 247935687 observed during Campaign 13. We classify this star as "SLF".

Appendix D.5. HYB

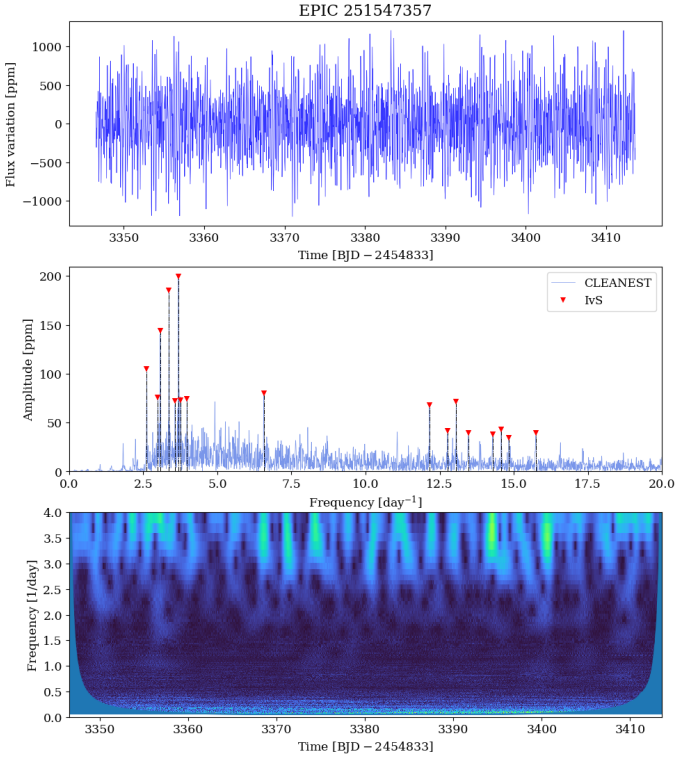


Figure A53. K2 light curve and frequency spectrum of EPIC 251547357 observed during Campaign 17. We classify this star as "HYB".

Appendix D.6. ROT/BIN and EBIN

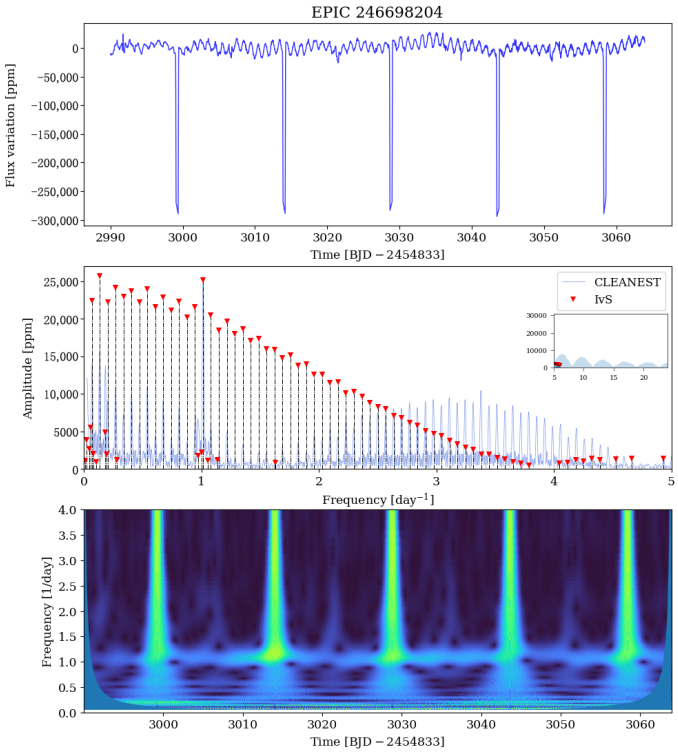


Figure A54. K2 light curve and frequency spectrum of EPIC 246698204 observed during Campaign 13. We classify this star as "EBIN".

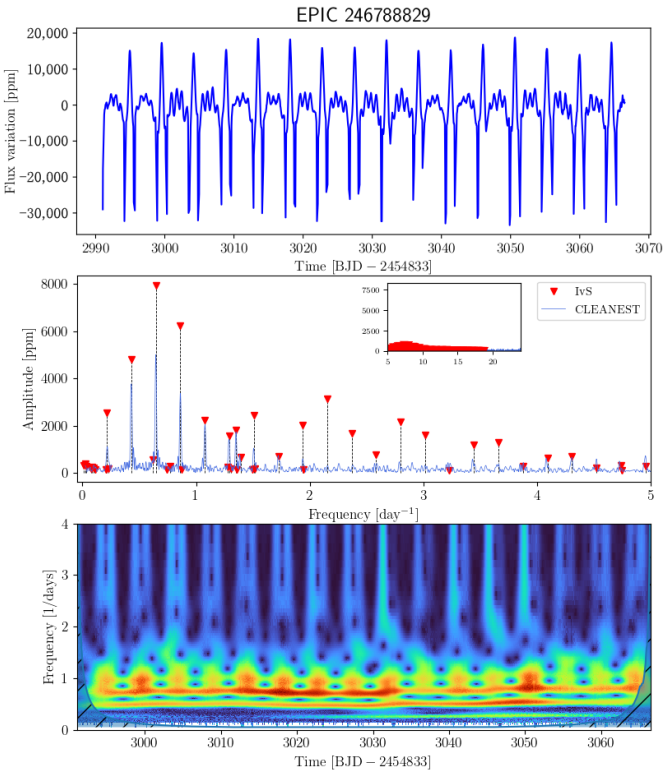


Figure A55. K2 light curve and frequency spectrum of EPIC 246788829 observed during Campaign 13. We classify this star as "ROT/BIN".

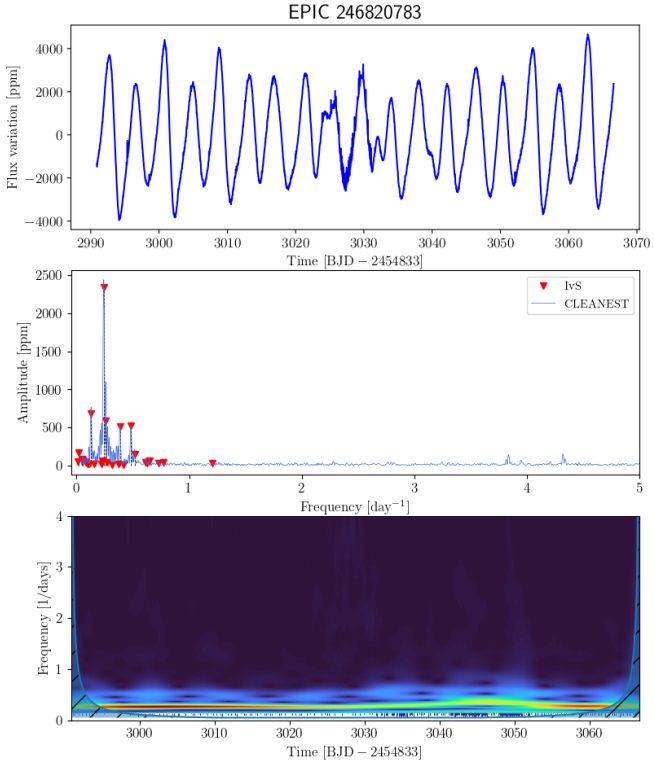


Figure A56. K2 light curve and frequency spectrum of EPIC 246820783 observed during Campaign 13. We classify this star as "ROT/BIN".

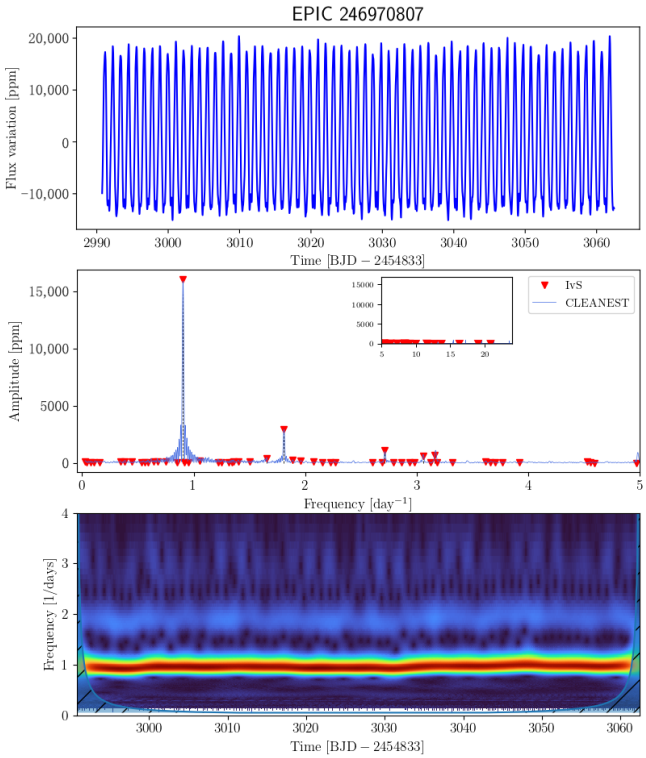


Figure A57. K2 light curve and frequency spectrum of EPIC 246970807 observed during Campaign 13. We classify this star as "ROT/BIN".

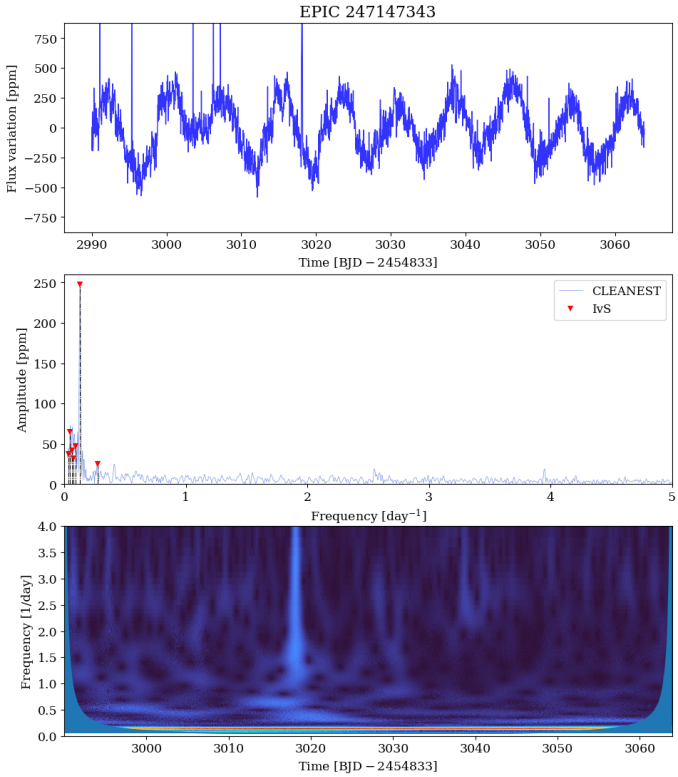


Figure A58. K2 light curve and frequency spectrum of EPIC 247147343 observed during Campaign 13. We classify this star as "ROT/BIN".

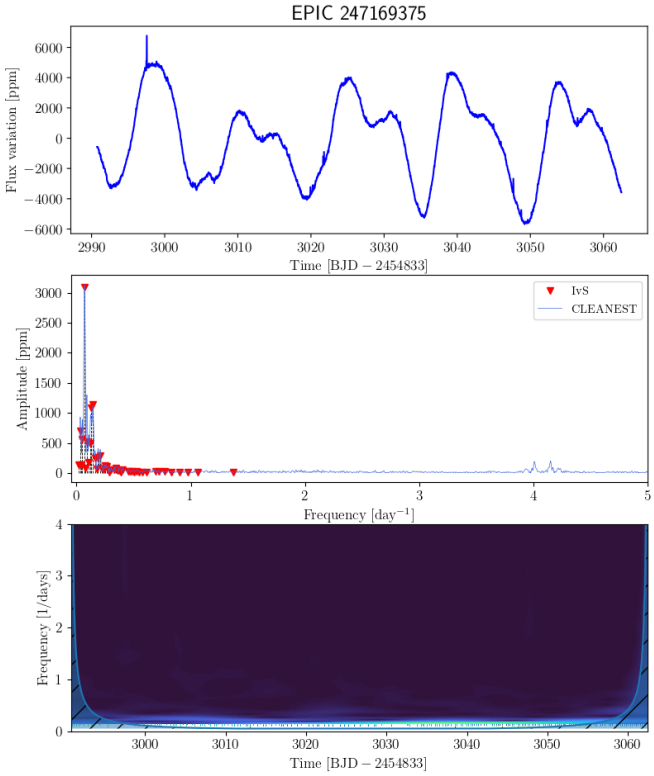


Figure A59. K2 light curve and frequency spectrum of EPIC 247169375 observed during Campaign 13. We classify this star as "ROT/BIN".

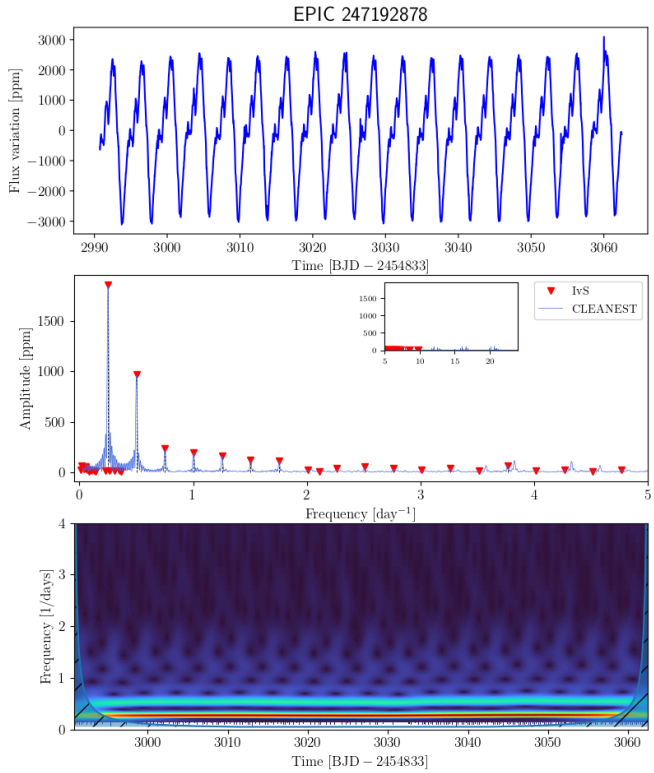


Figure A60. K2 light curve and frequency spectrum of EPIC 247192878 observed during Campaign 13. We classify this star as "ROT/BIN".

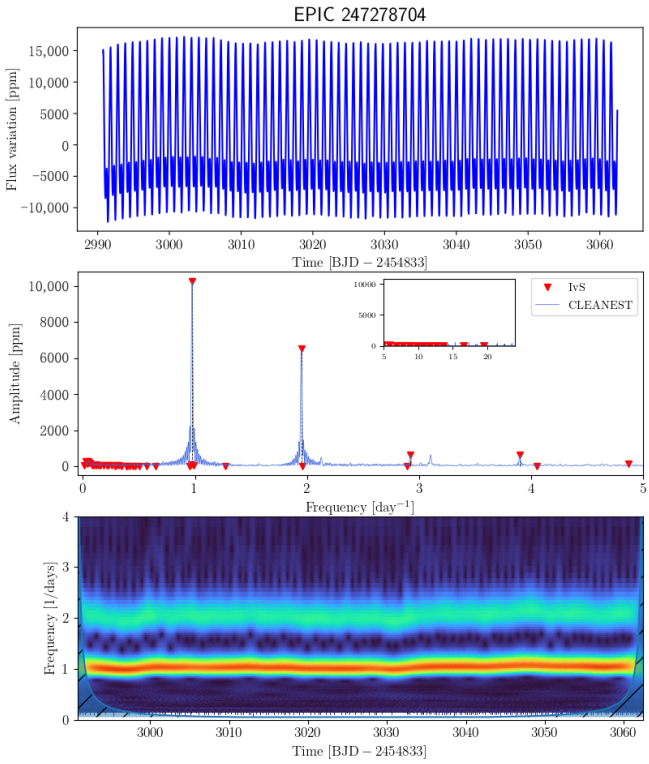


Figure A61. K2 light curve and frequency spectrum of EPIC 247278704 observed during Campaign 13. We classify this star as "ROT/BIN".

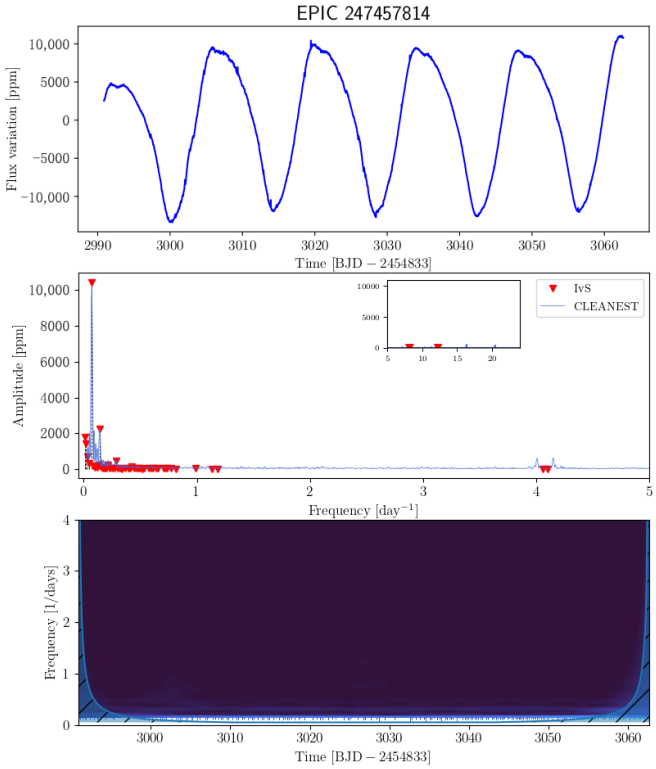


Figure A62. K2 light curve and frequency spectrum of EPIC 247457814 observed during Campaign 13. We classify this star as "ROT/BIN".

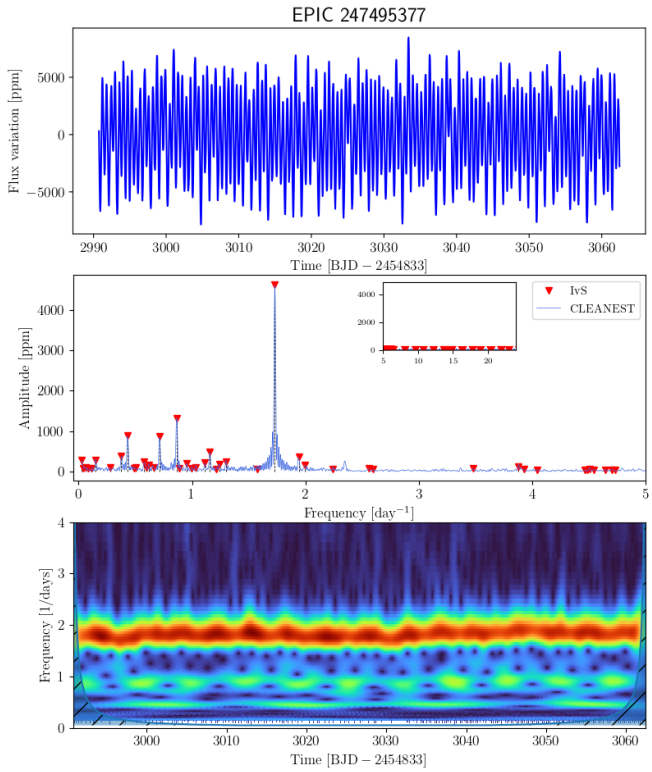


Figure A63. K2 light curve and frequency spectrum of EPIC 247495377 observed during Campaign 13. We classify this star as "ROT/BIN".

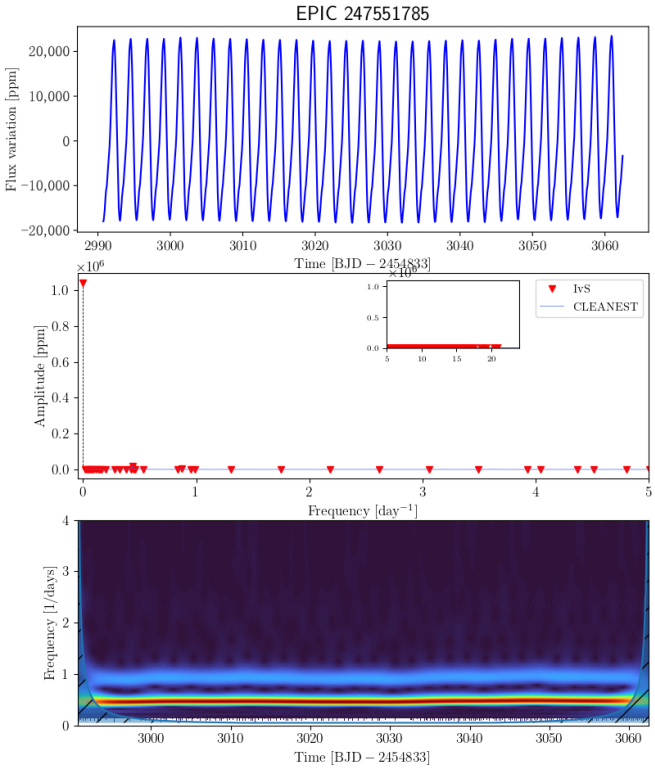


Figure A64. K2 light curve and frequency spectrum of EPIC 247551785 observed during Campaign 13. We classify this star as "ROT/BIN".

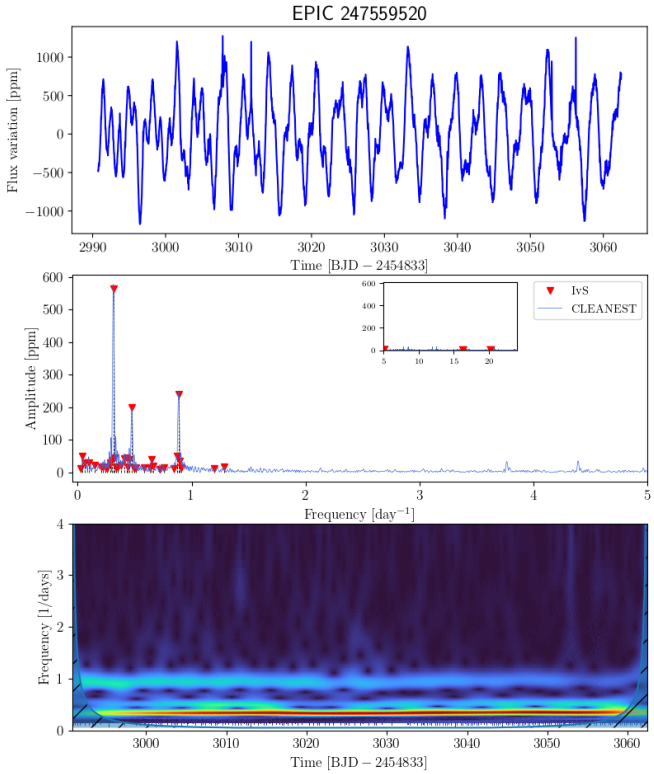


Figure A65. K2 light curve and frequency spectrum of EPIC 247559520 observed during Campaign 13. We classify this star as "ROT/BIN".

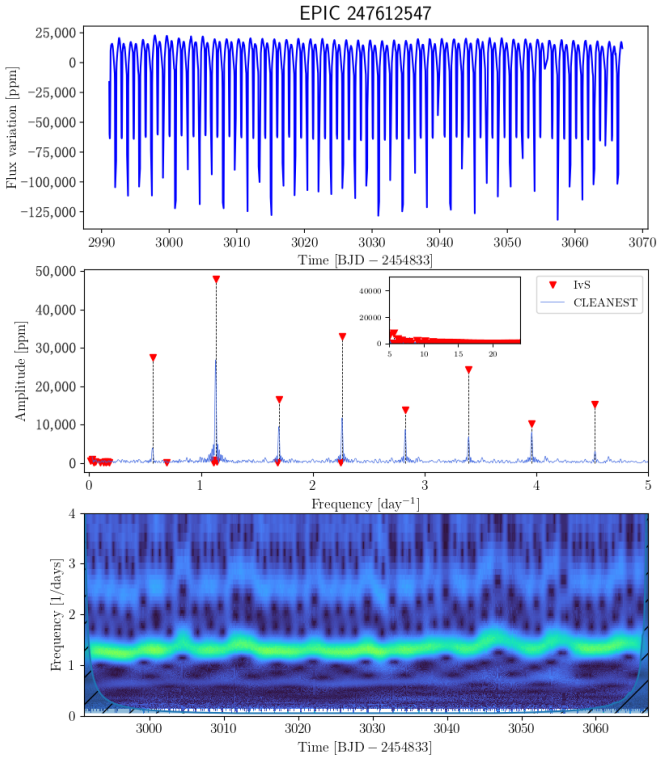


Figure A66. K2 light curve and frequency spectrum of EPIC 247612547 observed during Campaign 13. We classify this star as "EBIN".

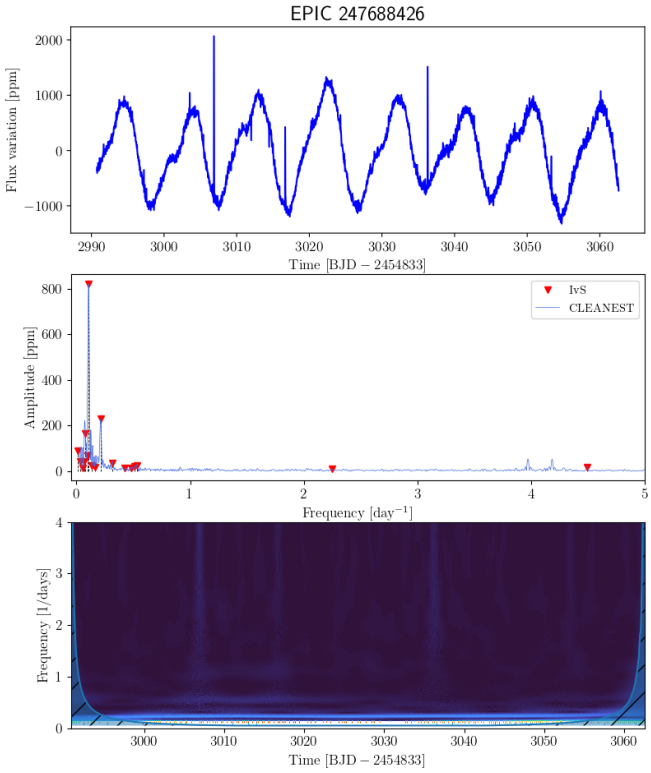


Figure A67. K2 light curve and frequency spectrum of EPIC 247688426 observed during Campaign 13. We classify this star as "ROT/BIN".

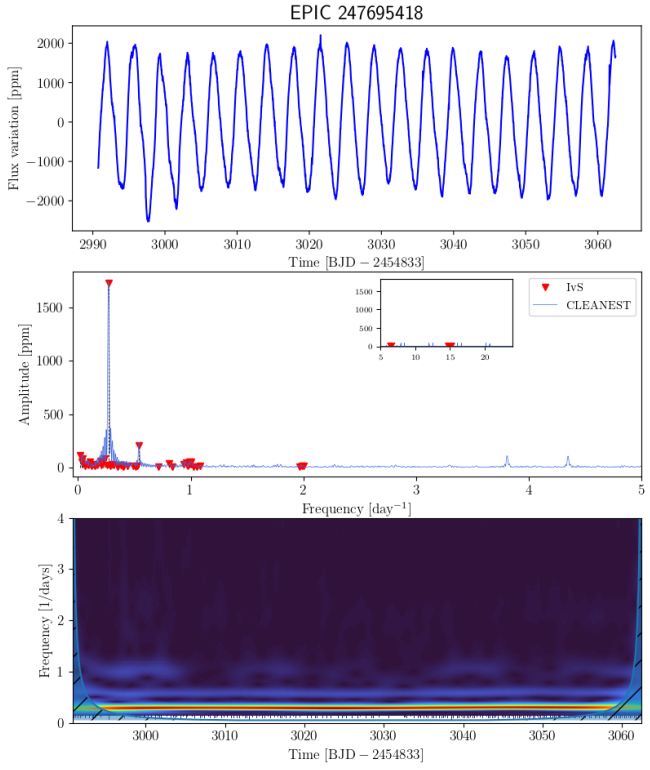


Figure A68. K2 light curve and frequency spectrum of EPIC 247695418 observed during Campaign 13. We classify this star as "ROT/BIN".

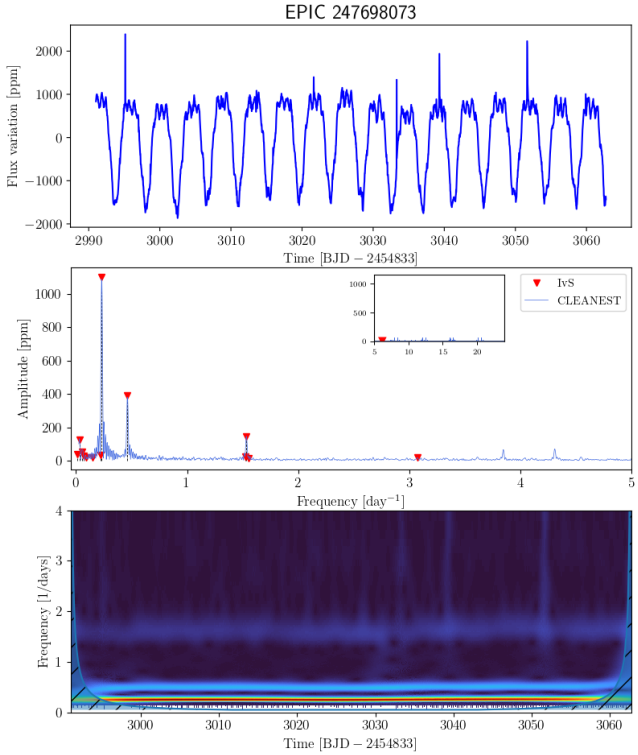


Figure A69. K2 light curve and frequency spectrum of EPIC 247698073 observed during Campaign 13. We classify this star as "ROT/BIN".

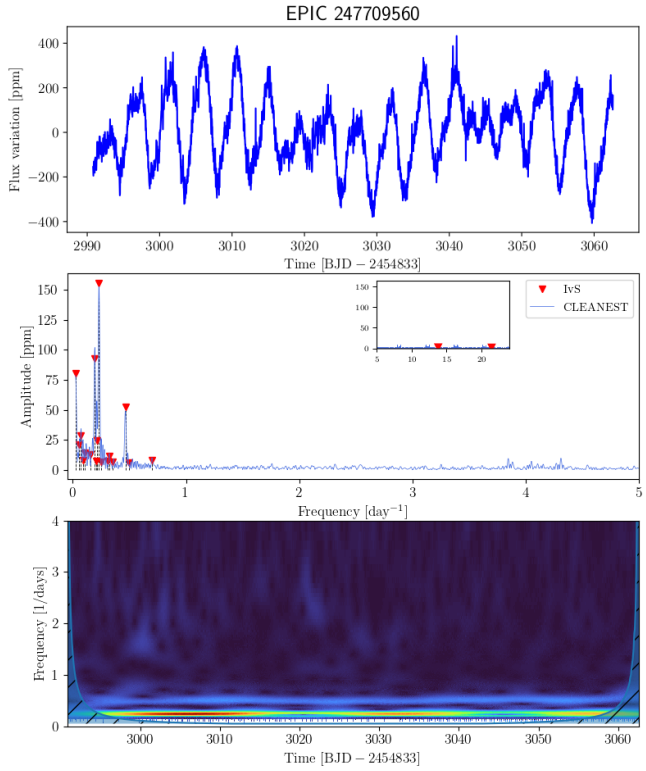


Figure A70. K2 light curve and frequency spectrum of EPIC 247709560 observed during Campaign 13. We classify this star as "ROT/BIN/SLF".

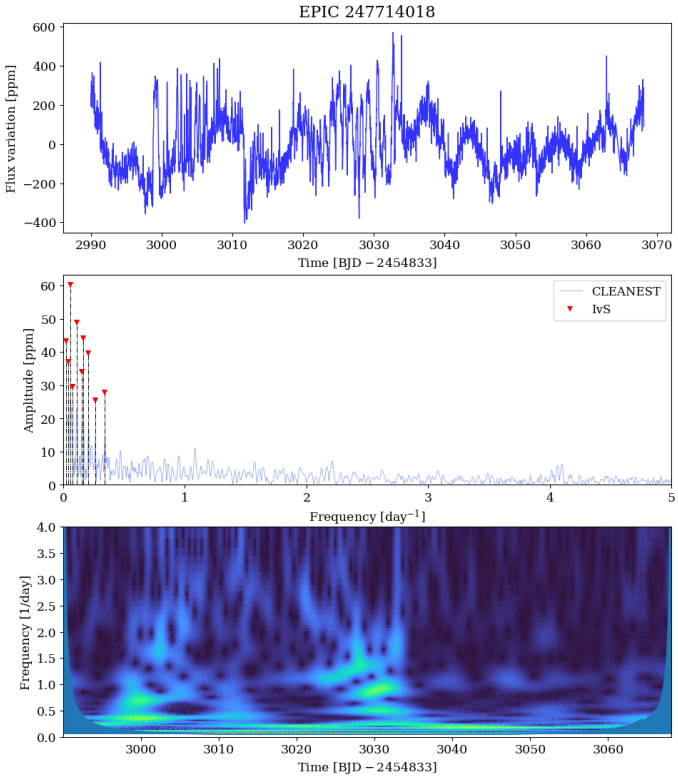


Figure A71. K2 light curve and frequency spectrum of EPIC 247714018 observed during Campaign 13. We classify this star as "ROT/BIN/SLF".

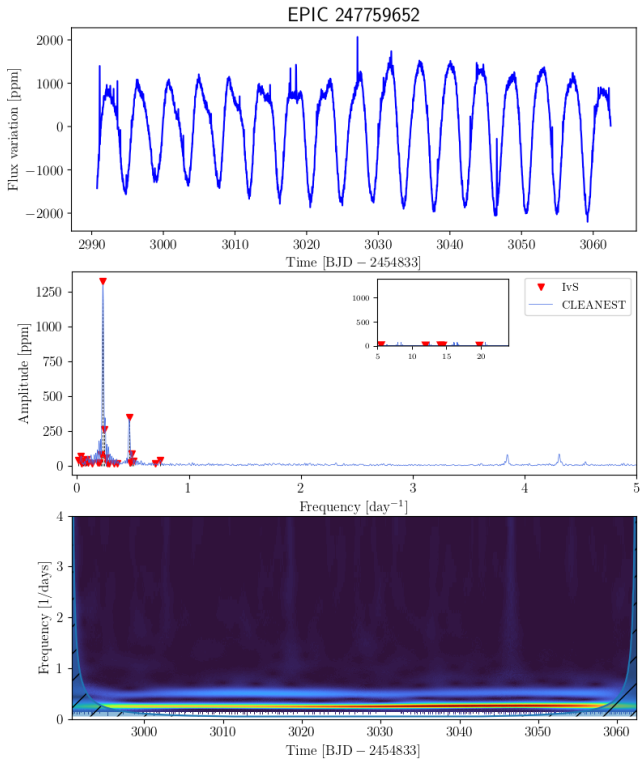


Figure A72. K2 light curve and frequency spectrum of EPIC 247759652 observed during Campaign 13. We classify this star as "ROT/BIN".

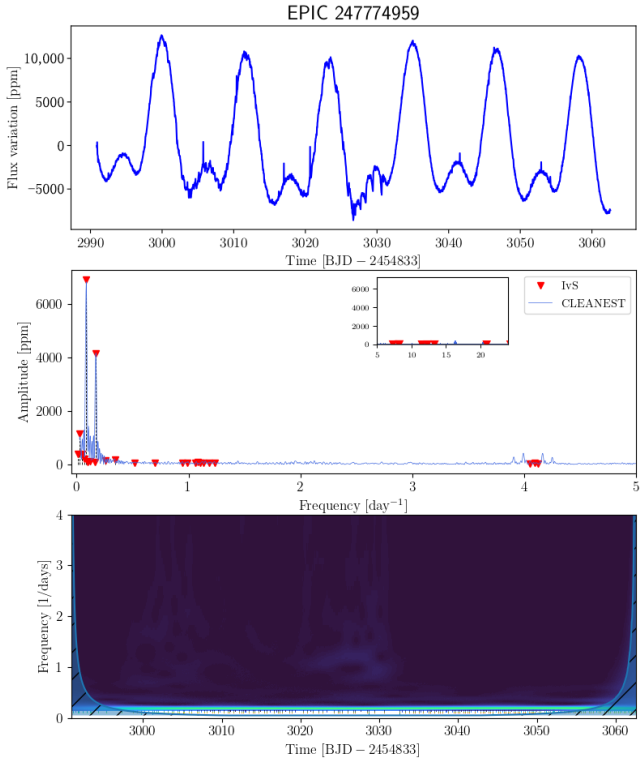


Figure A73. K2 light curve and frequency spectrum of EPIC 247774959 observed during Campaign 13. We classify this star as "ROT/BIN".

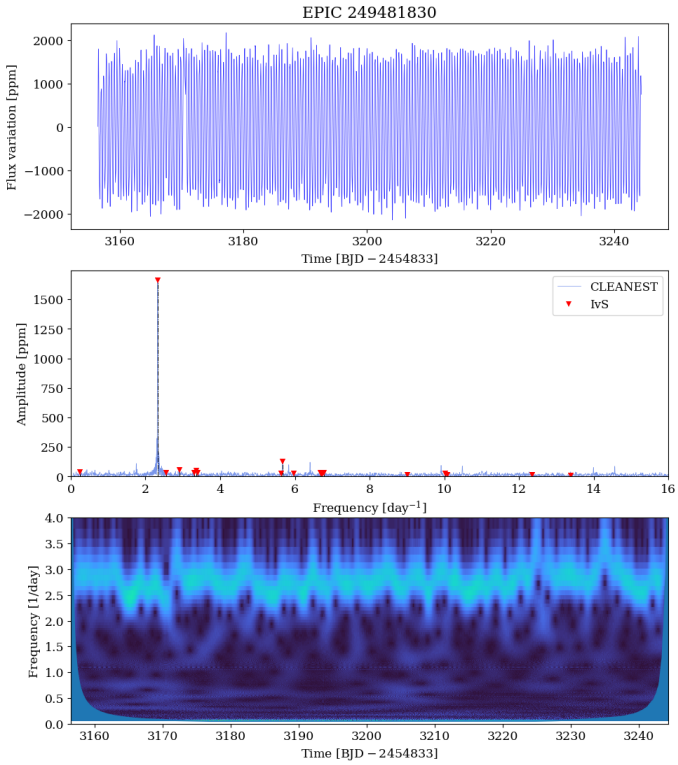


Figure A74. K2 light curve and frequency spectrum of EPIC 249481830 observed during Campaign 15. We classify this star as "ROT/BIN".

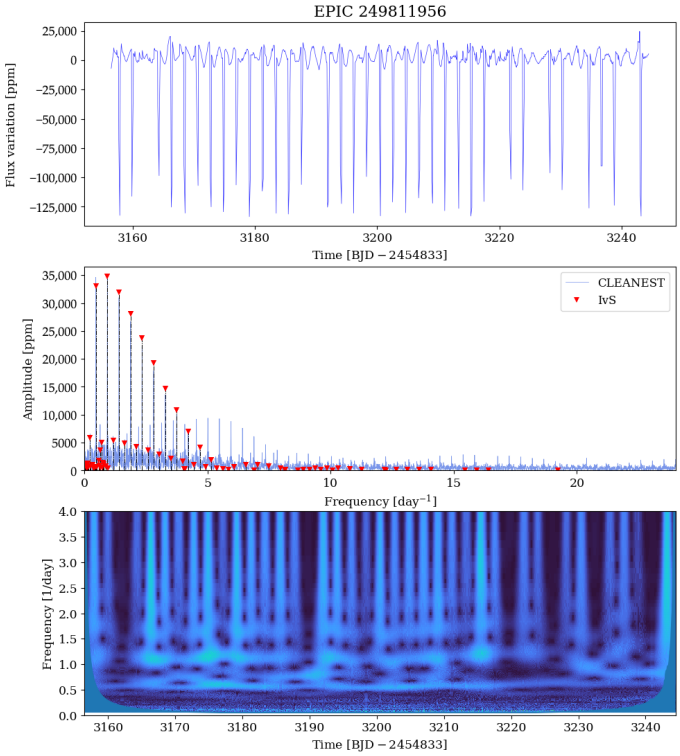


Figure A75. K2 light curve and frequency spectrum of EPIC 249811956 observed during Campaign 15. We classify this star as "EBIN".

Appendix E. Spectroscopic Data and Spectral Model Adjustment

Spectral data used for characterization: This plot contains the blue spectra of 34 stars obtained at Pico dos Dias Observatory and from LAMOST. The main spectral lines are signaled. The red line represents the spectral model from the `sme`, with the parameters shown in Table 2. The target selection and formatting follow the methodology presented in the doctoral theses of Silva (Campaign 13) [89] and Eidam (Campaigns 15–18) [90].

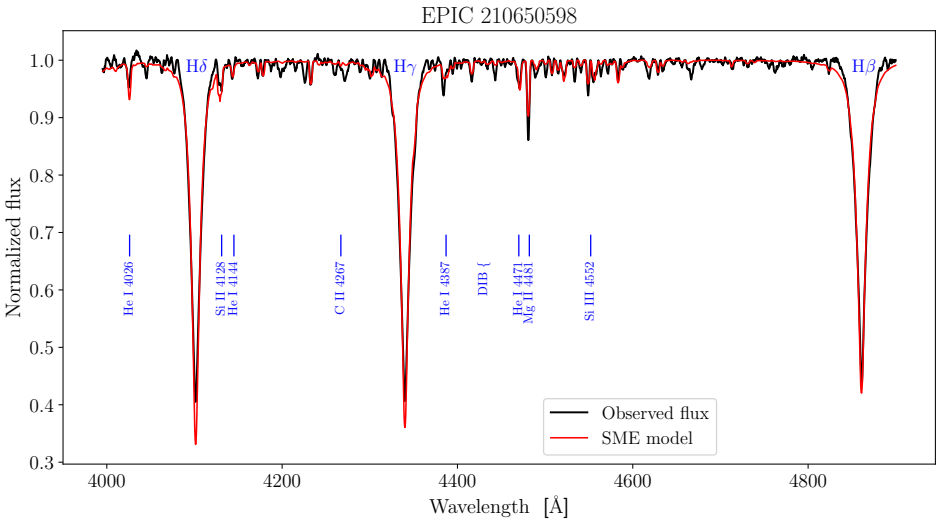


Figure A76. Spectrum of EPIC 210650598 (HD 28436) observed during Campaign 13.

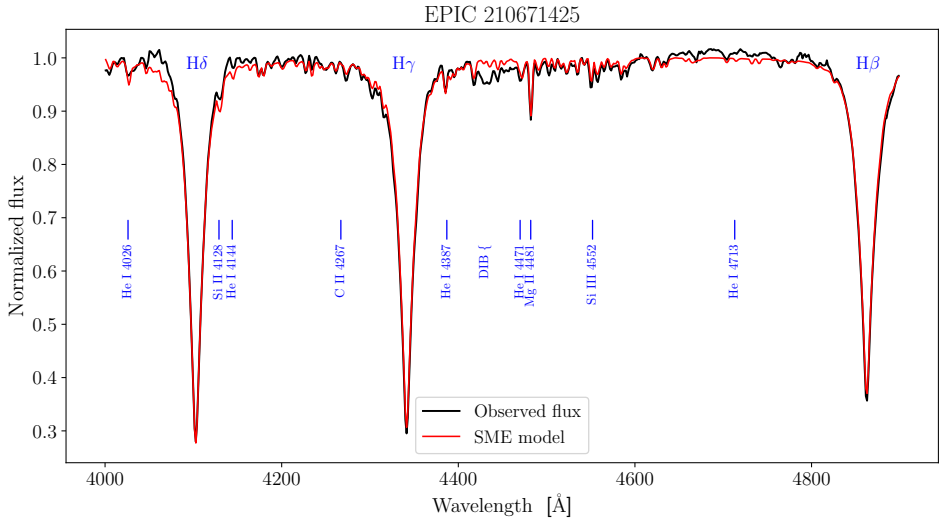


Figure A77. Spectrum of EPIC 210671425 (HD 285777) observed during Campaign 13.

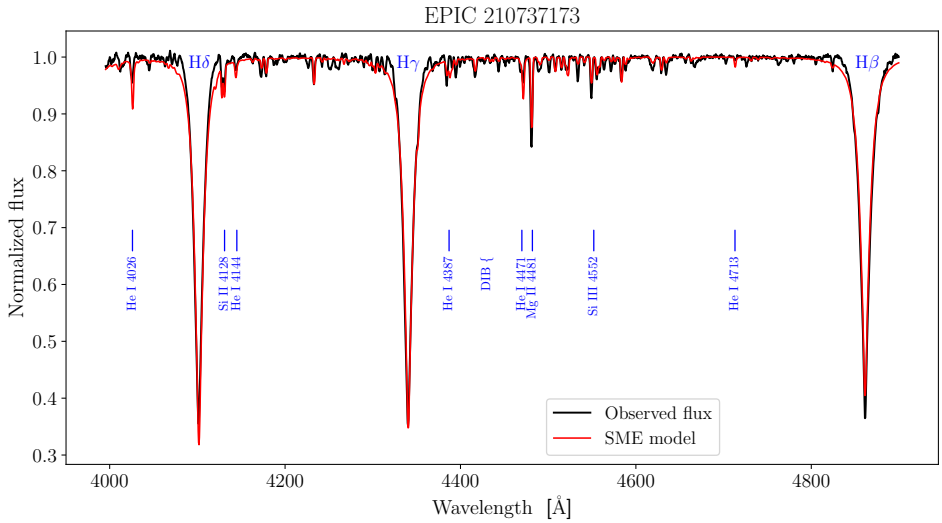


Figure A78. Spectrum of EPIC 210737173 (HD 27877) observed during Campaign 13.

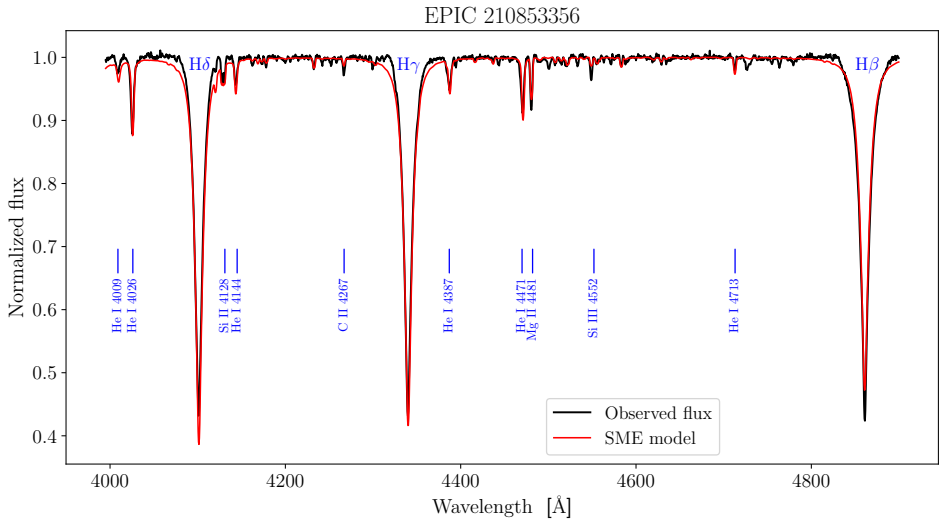


Figure A79. Spectrum of EPIC 210853356 (HD 28304) observed during Campaign 13.

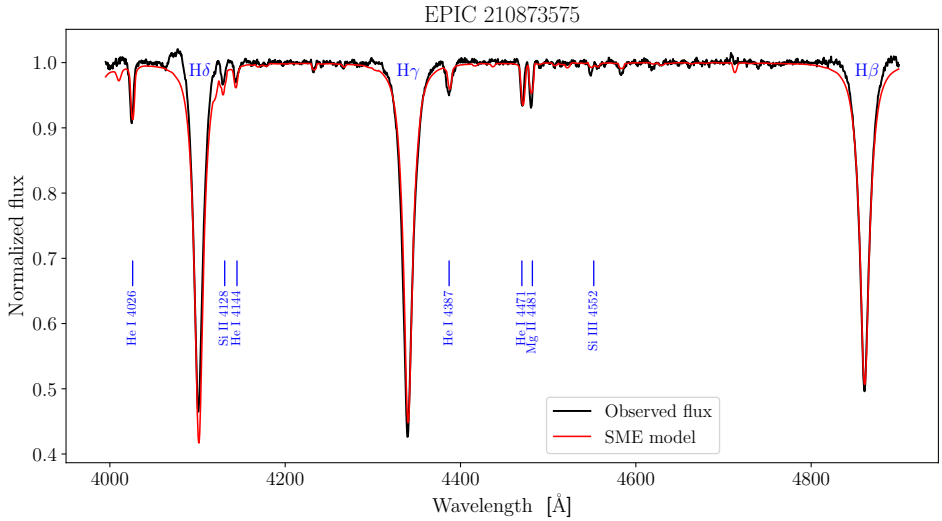


Figure A80. Spectrum of EPIC 210873575 (HD 27742) observed during Campaign 13.

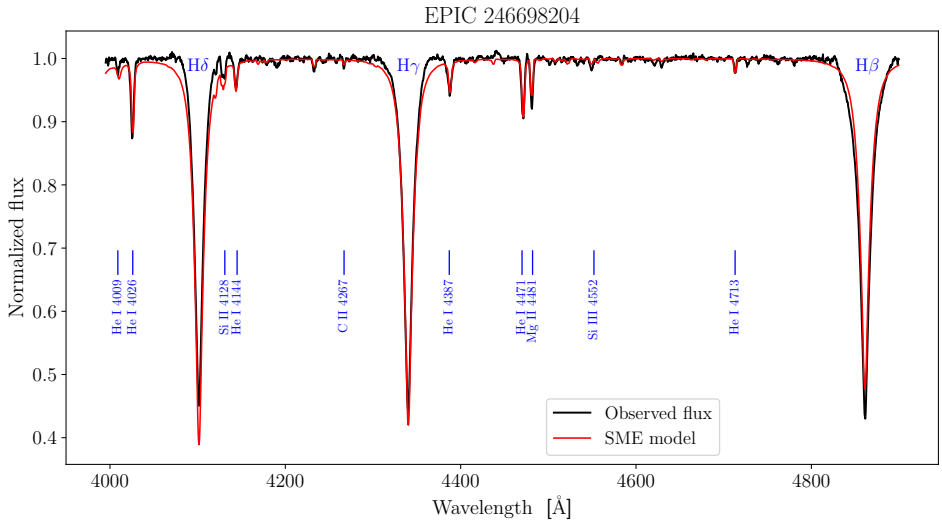


Figure A81. Spectrum of EPIC 246698204 (HD 31747) observed during Campaign 13.

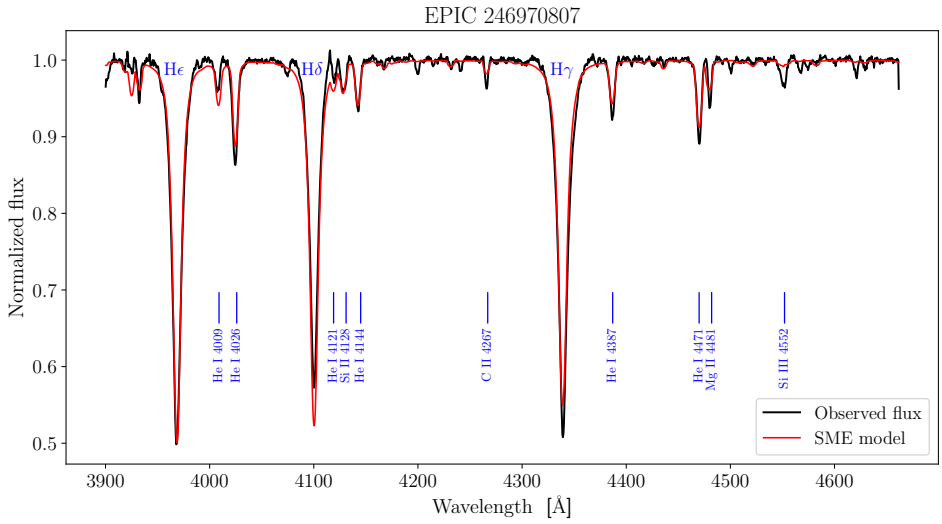


Figure A82. Spectrum of EPIC 246970807 (HD 33402) observed during Campaign 13.

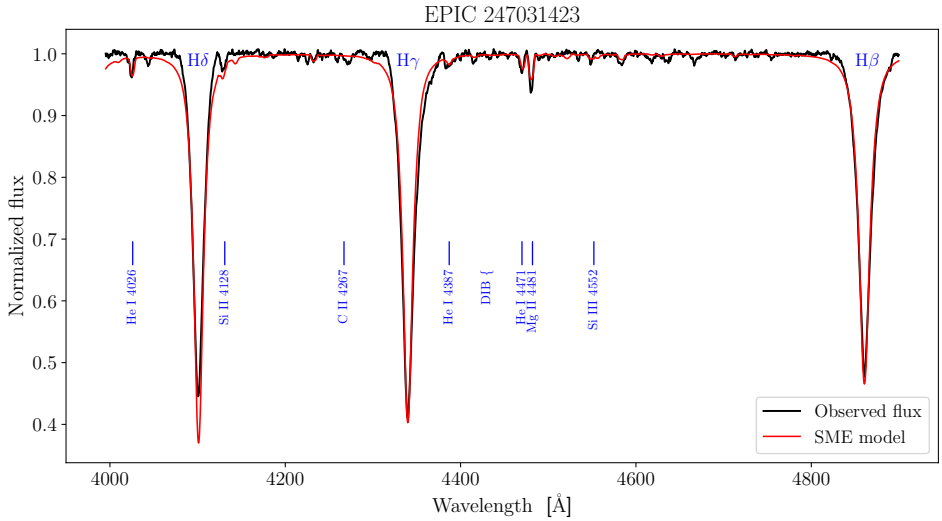


Figure A83. Spectrum of EPIC 247031423 (HD 28867) observed during Campaign 13.

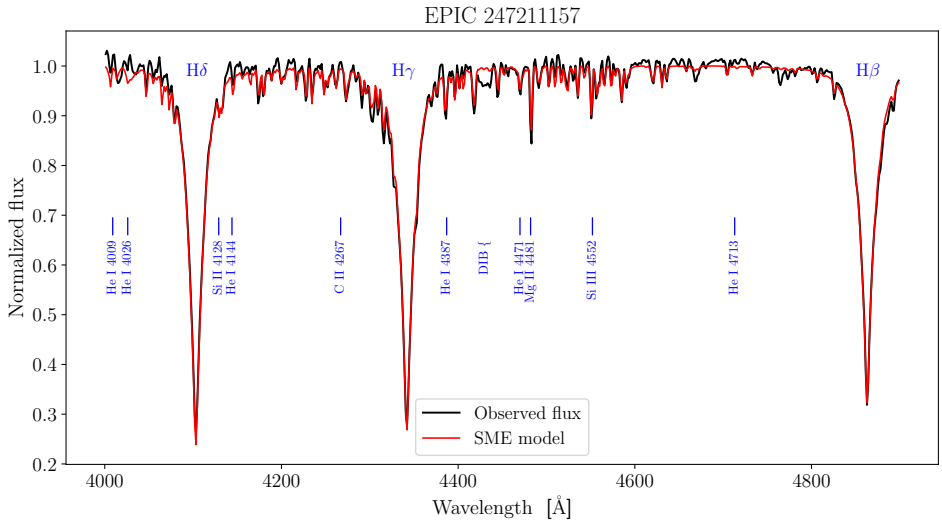


Figure A84. Spectrum of EPIC 247211157 (HD 284634) observed during Campaign 13.

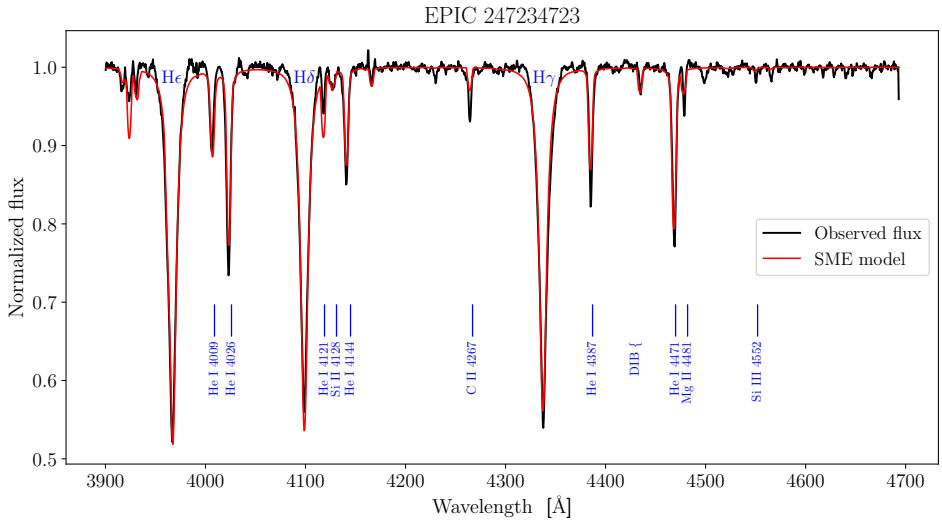


Figure A85. Spectrum of EPIC 247234723 (HD 34133) observed during Campaign 13.

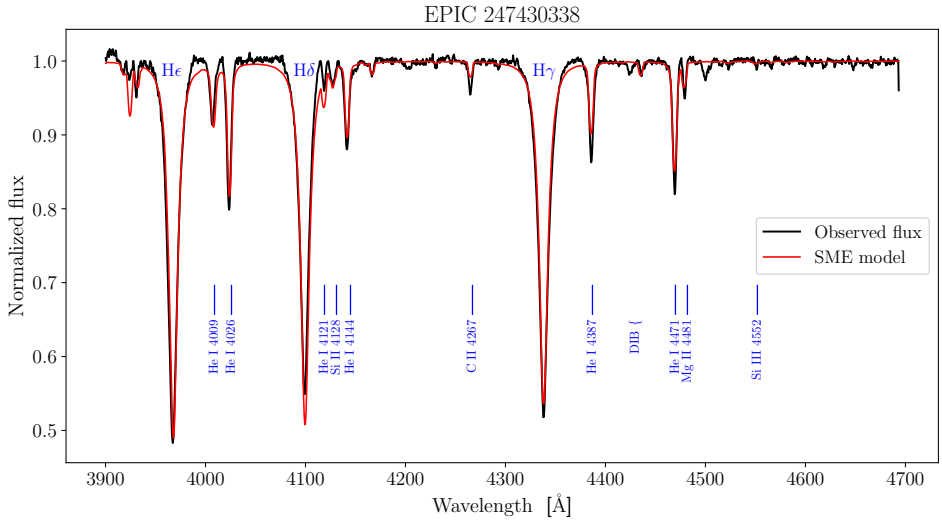


Figure A86. Spectrum of EPIC 247430338 (HD 32481) observed during Campaign 13.

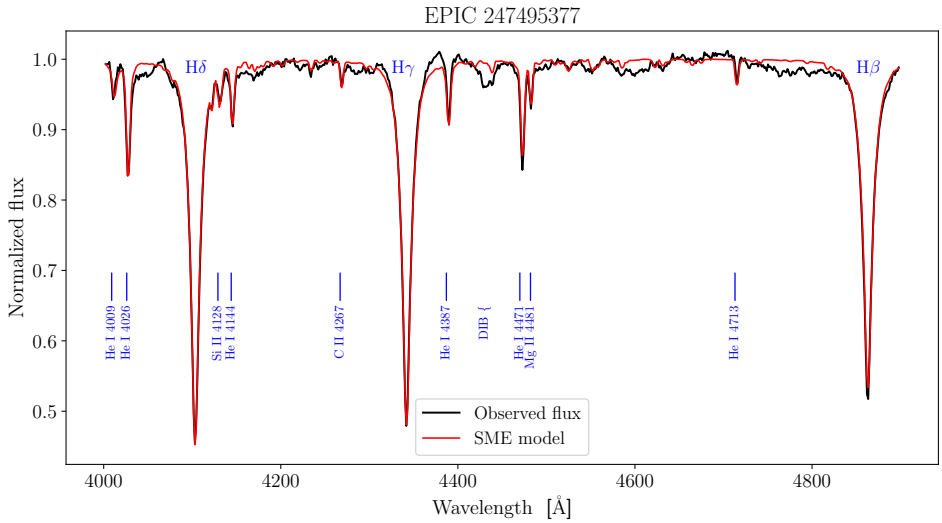


Figure A87. Spectrum of EPIC 247495377 (HD 284993) observed during Campaign 13.

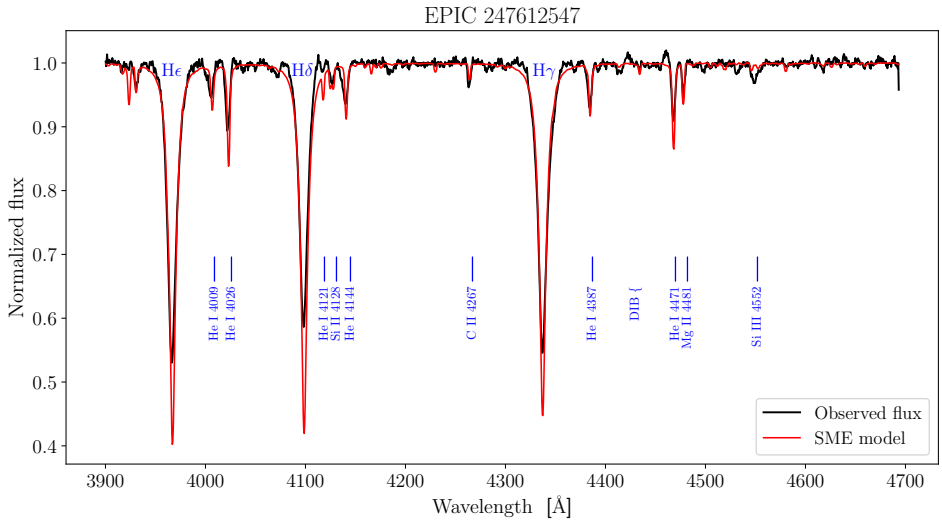


Figure A88. Spectrum of EPIC 247612547 (HD 32641) observed during Campaign 13.

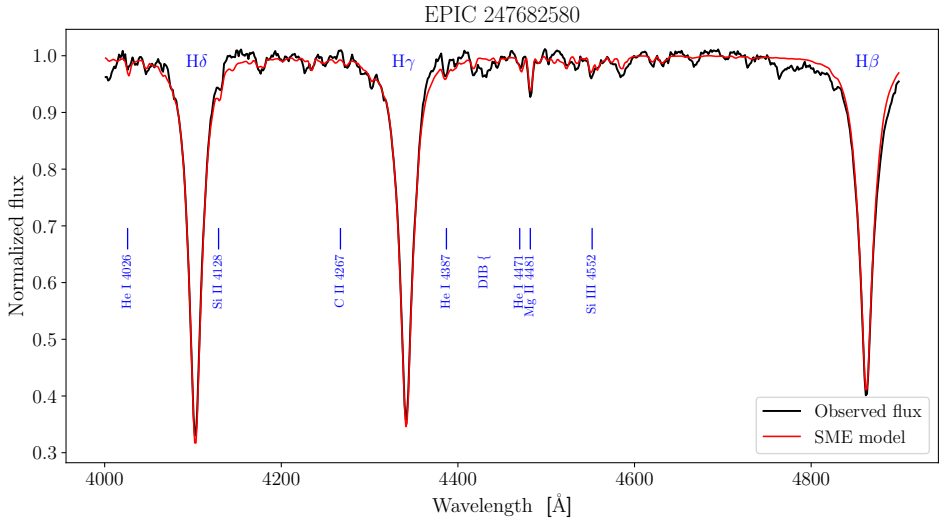


Figure A89. Spectrum of EPIC 247682580 (HD 284941) observed during Campaign 13.

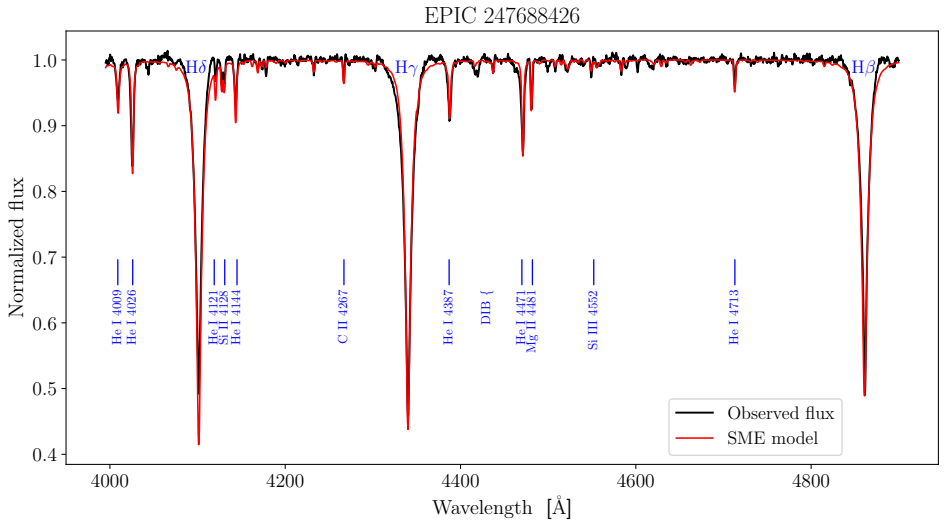


Figure A90. Spectrum of EPIC 247688426 (HD 30122) observed during Campaign 13.

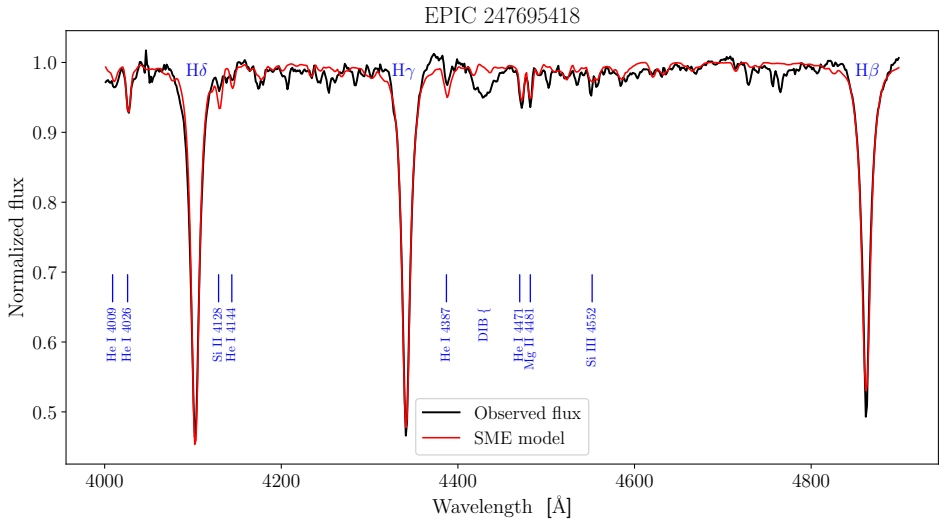


Figure A91. Spectrum of EPIC 247695418 (HD 285127) observed during Campaign 13.

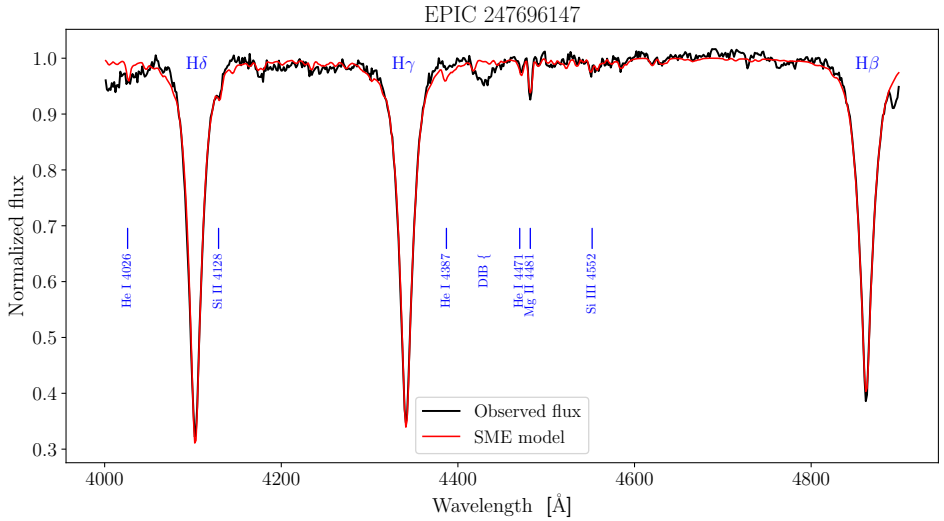


Figure A92. Spectrum of EPIC 247696147 (HD 285124) observed during Campaign 13.

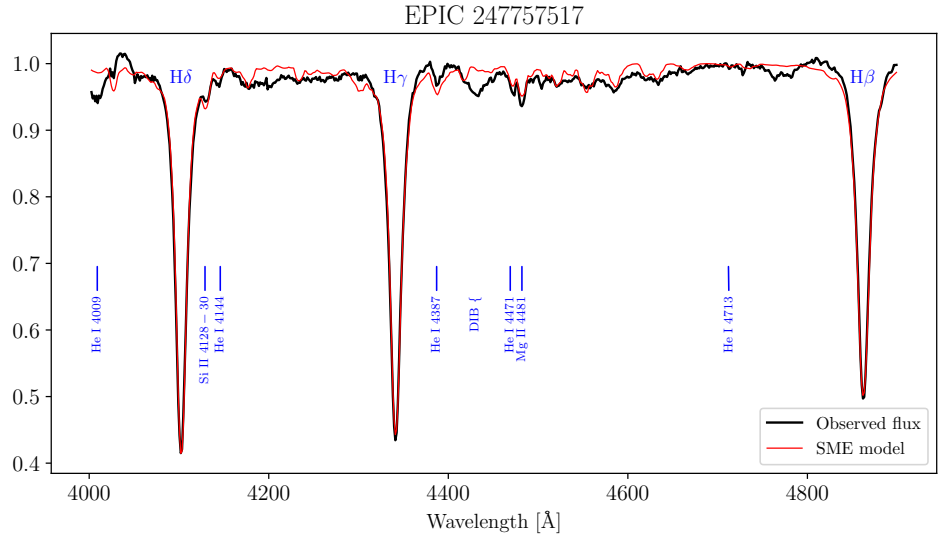


Figure A93. Spectrum of EPIC 247757517 (HD 284119) observed during Campaign 13.

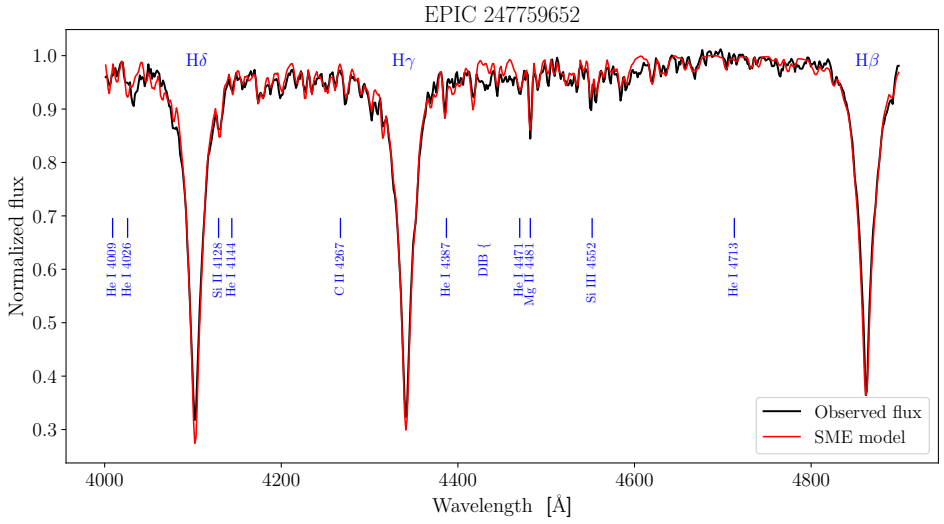


Figure A94. Spectrum of EPIC 247759652 (HD 284045) observed during Campaign 13.

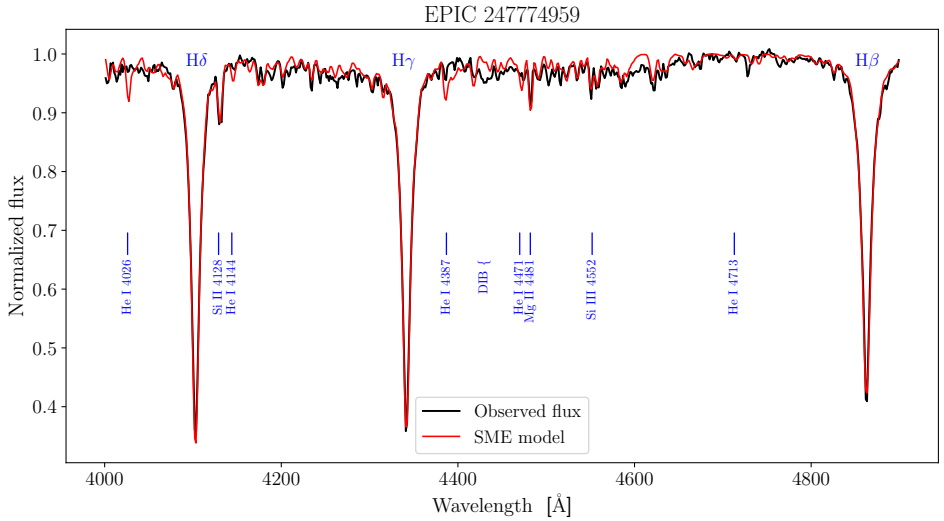


Figure A95. Spectrum of EPIC 247774959 (GSC 01829-00022) observed during Campaign 13.

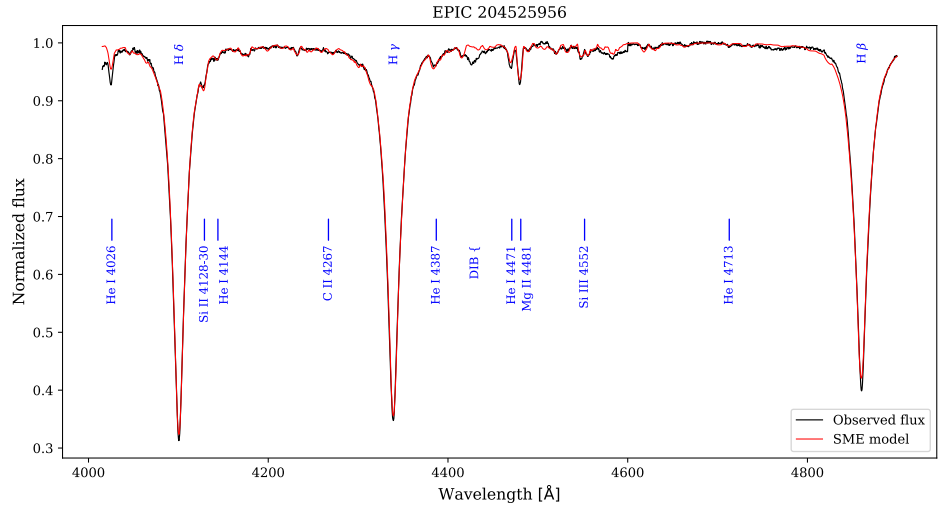


Figure A96. Spectrum of EPIC 204525956 (HD 143567) observed during Campaign 15.

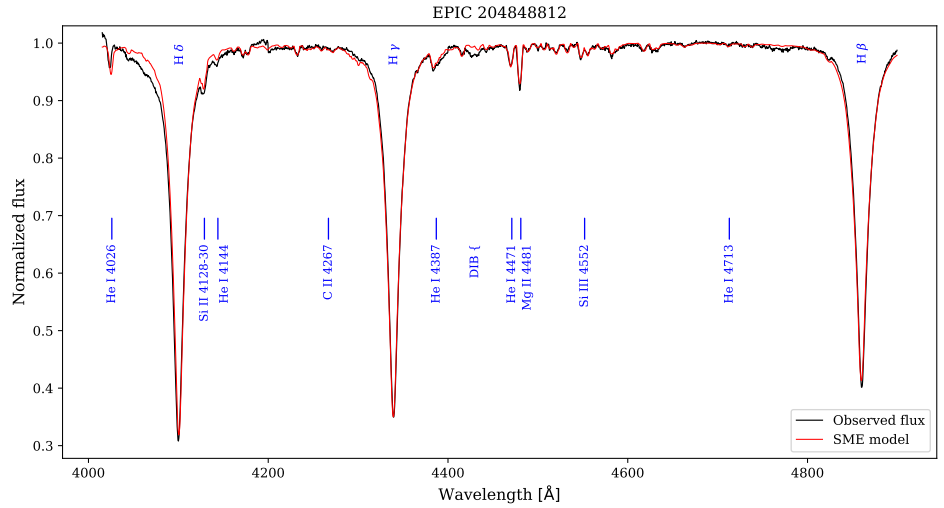


Figure A97. Spectrum of EPIC 204848812 (HD 141774) observed during Campaign 15.

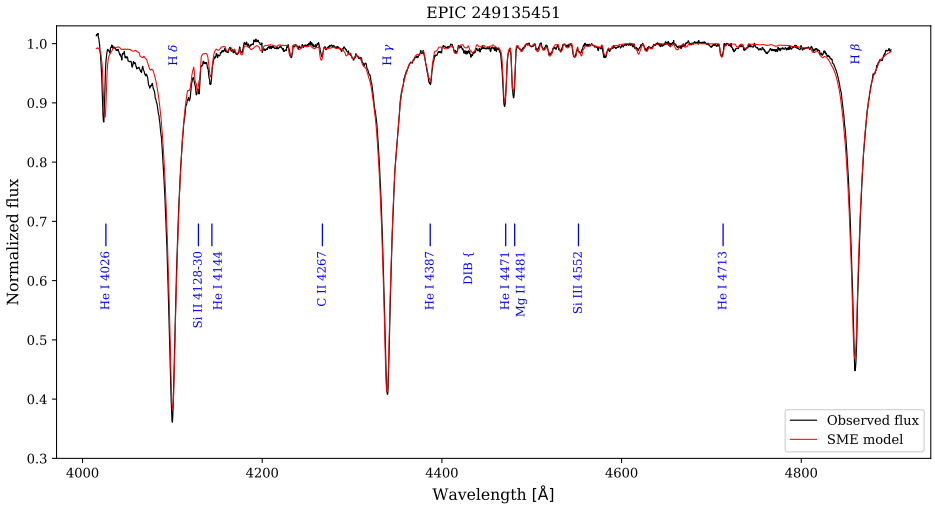


Figure A98. Spectrum of EPIC 249135451 (HD 139094) observed during Campaign 15.

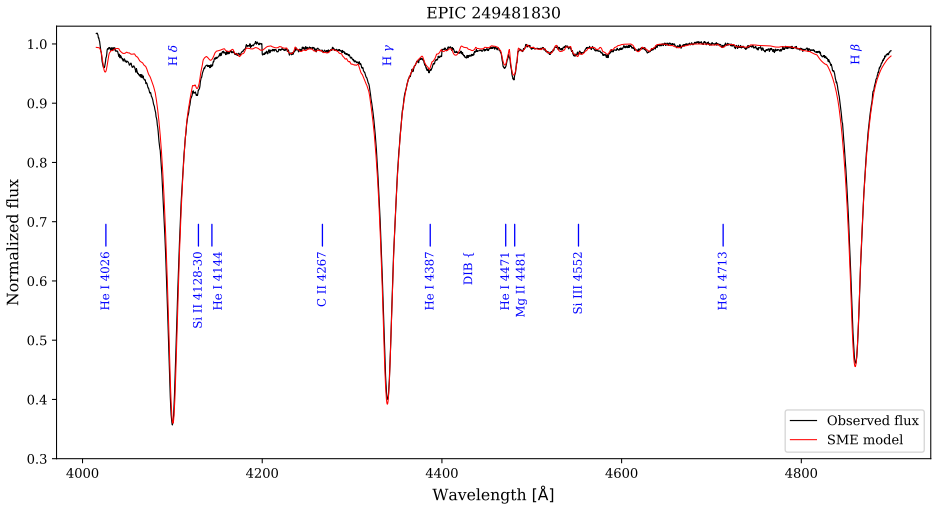


Figure A99. Spectrum of EPIC 249481830 (HD 138343) observed during Campaign 15.

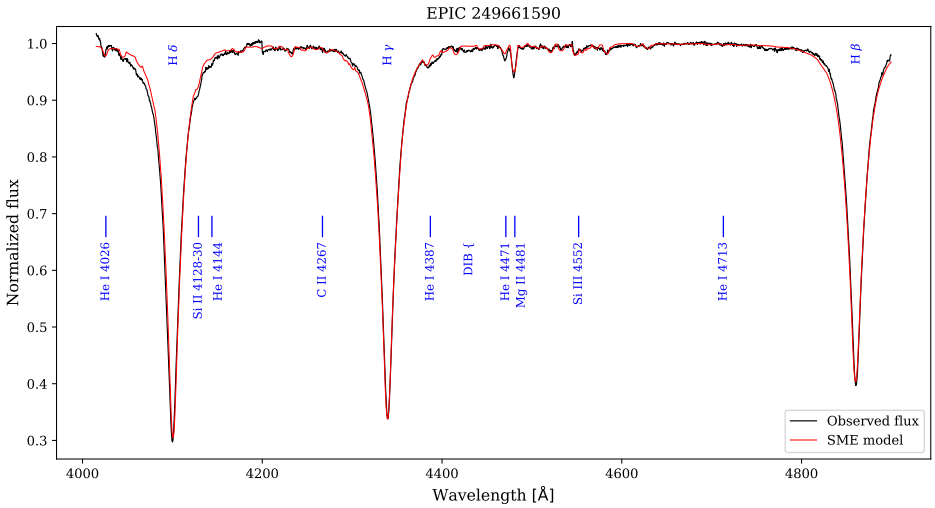


Figure A100. Spectrum of EPIC 249661590 (HD 139486) observed during Campaign 15.

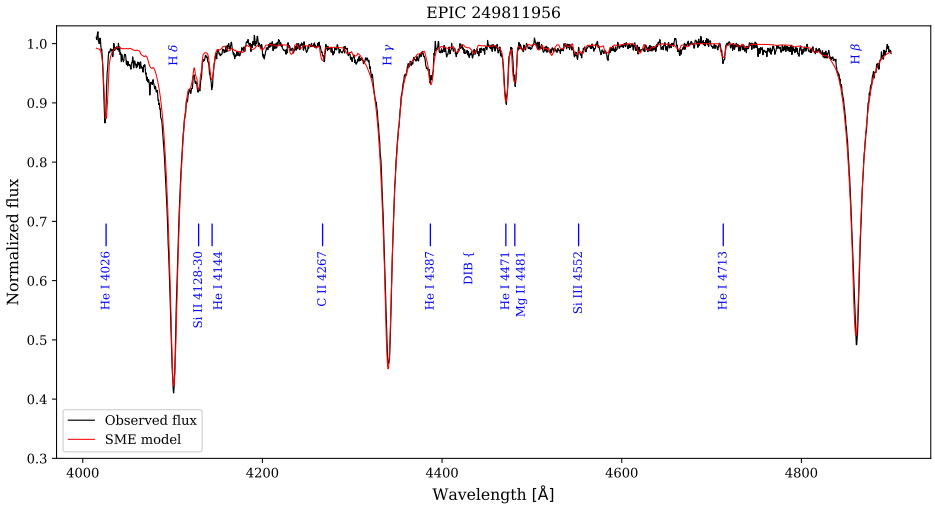


Figure A101. Spectrum of EPIC 249811956 (V* HQ Lib) observed during Campaign 15.

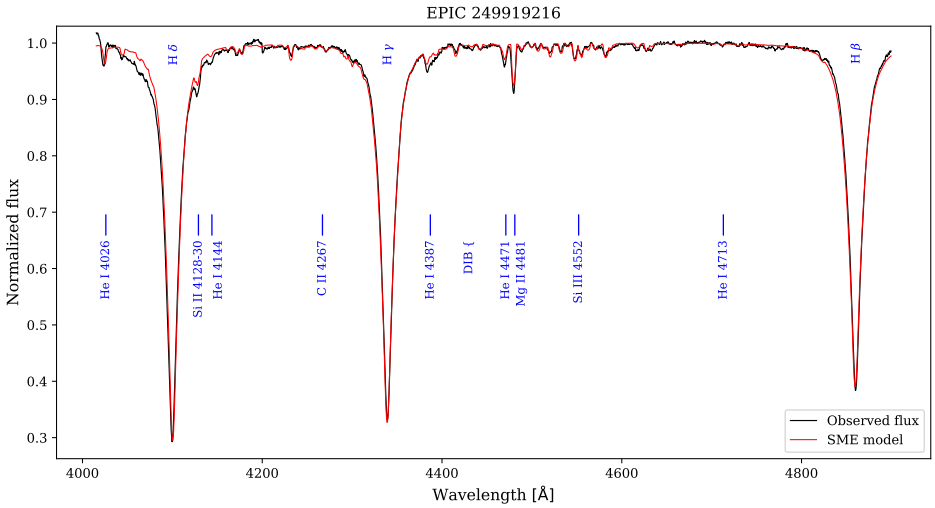


Figure A102. Spectrum of EPIC 249919216 (HD 134796) observed during Campaign 15.

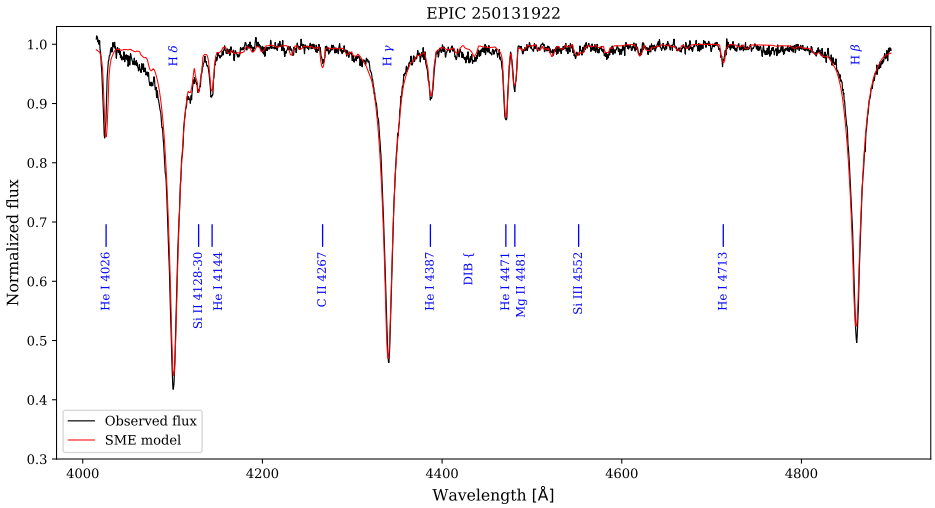


Figure A103. Spectrum of EPIC 250131922 (BD-13 4202) observed during Campaign 15.

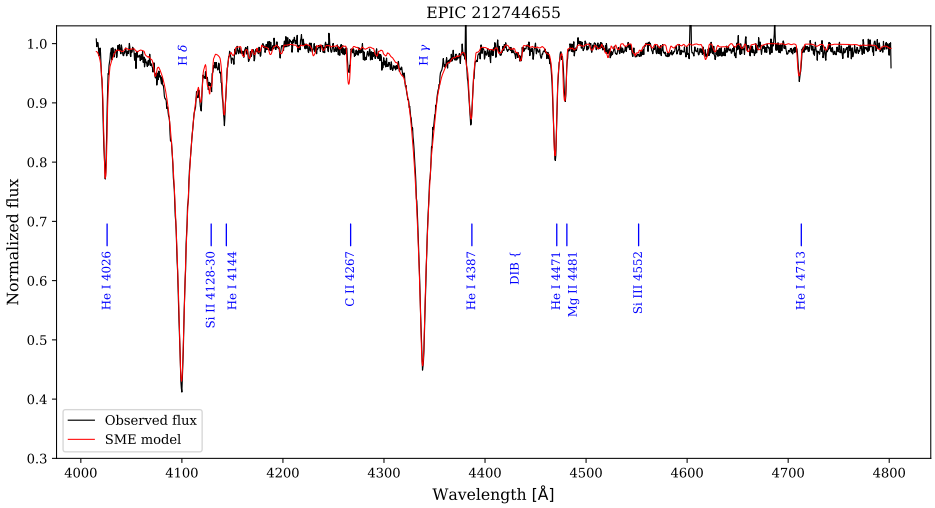


Figure A104. Spectrum of EPIC 212744655 (EC 15103-1557) observed during Campaign 17.

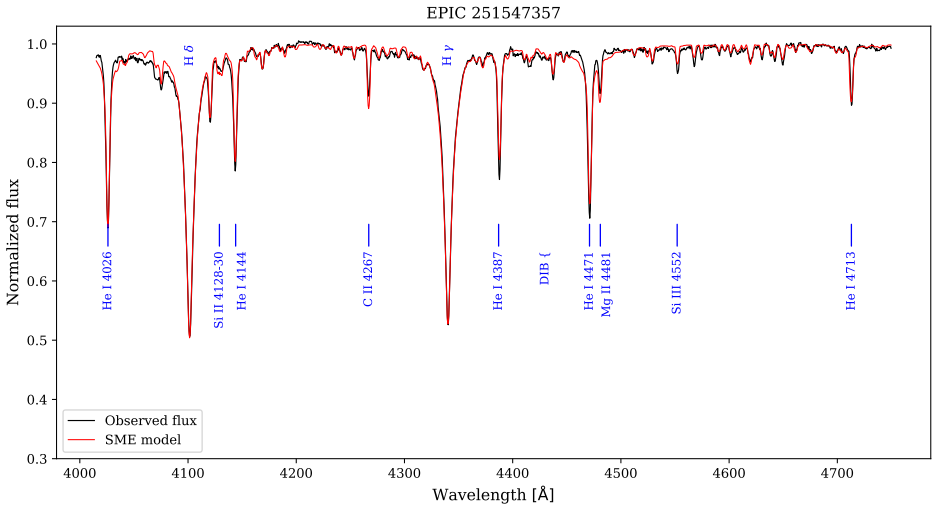


Figure A105. Spectrum of EPIC 251547357 (HD 118246) observed during Campaign 17.

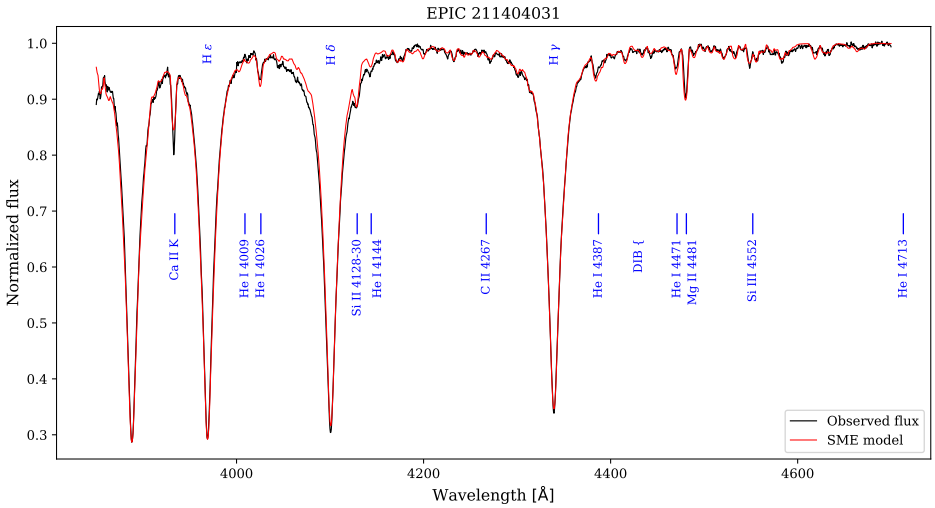


Figure A106. Spectrum of EPIC 211404031 (HD 120086) observed during Campaign 18.

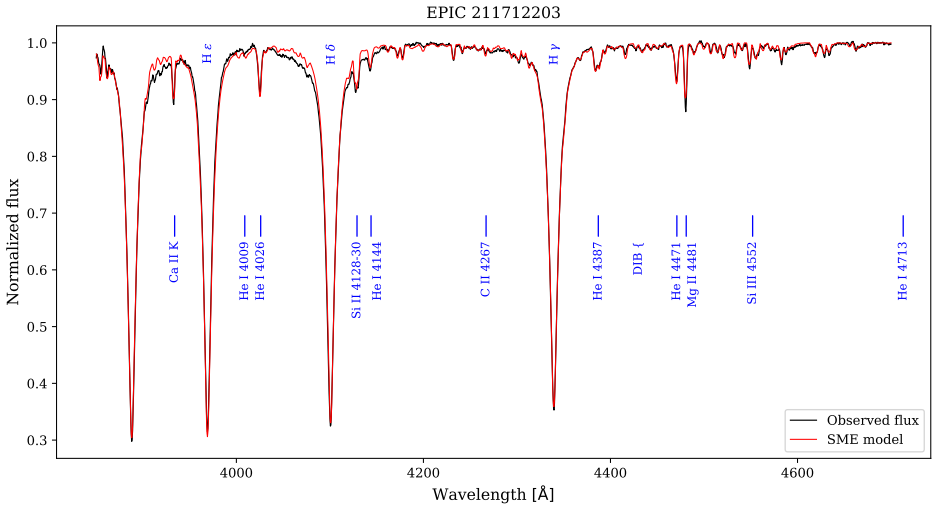


Figure A107. Spectrum of EPIC 211712203 (HD 73046) observed during Campaign 18.

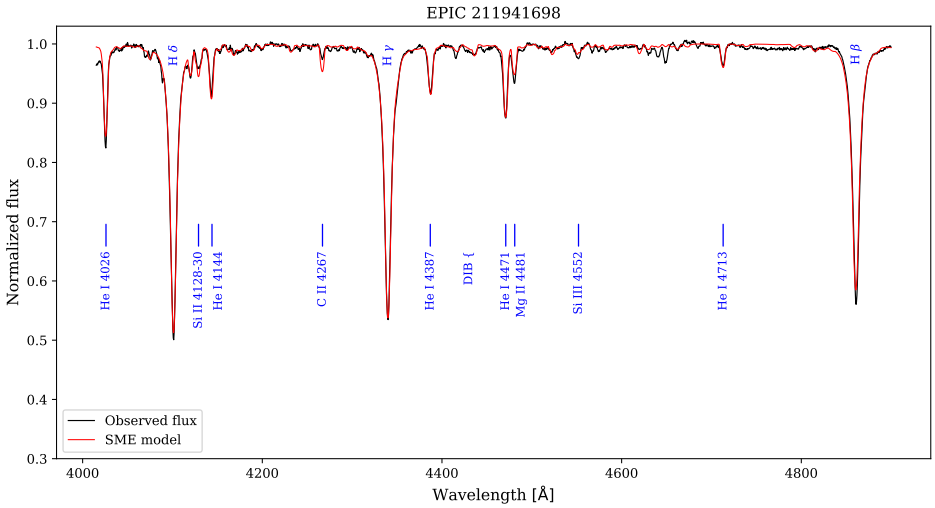


Figure A108. Spectrum of EPIC 211941698 (HD 75750) observed during Campaign 18.

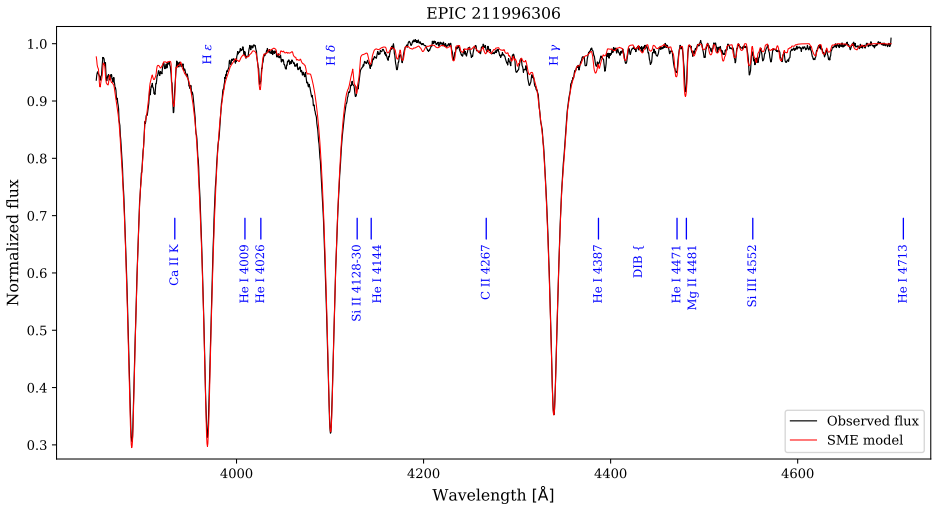


Figure A109. Spectrum of EPIC 211996306 (HD 75750) observed during Campaign 18.

References

1. Langer, N. Presupernova Evolution of Massive Single and Binary Stars. *Annu. Rev. Astron. Astrophys.* **2012**, *50*, 107–164. [CrossRef]
2. Ekström, S.; Georgy, C.; Eggenberger, P.; Meynet, G.; Mowlavi, N.; Wyttenbach, A.; Granada, A.; Decressin, T.; Hirschi, R.; Frischknecht, U.; et al. Grids of stellar models with rotation. I. Models from 0.8 to 120 $M_{\odot}$ at solar metallicity (Z = 0.014). *Astron. Astrophys.* **2012**, *537*, A146. [CrossRef]
3. Kuschnig, R. Space observations of O and B stars with MOST. *Commun. Asteroseismol.* **2009**, *158*, 162.
4. Auvergne, M.; Bodin, P.; Boisnard, L.; Buey, J.T.; Chaintreuil, S.; Epstein, G.; Jouret, M.; Lam-Trong, T.; Levacher, P.; Magnan, A.; et al. The CoRoT satellite in flight: Description and performance. *Astron. Astrophys.* **2009**, *506*, 411–424. [CrossRef]
5. Caldwell, D.A.; van Cleve, J.E.; Jenkins, J.M.; Argabright, V.S.; Kolodziejczak, J.J.; Dunham, E.W.; Geary, J.C.; Tenenbaum, P.; Chandrasekaran, H.; Li, J.; et al. Kepler instrument performance: An in-flight update. In *Space Telescopes and Instrumentation 2010: Optical, Infrared, and Millimeter Wave*; Society of Photo-Optical Instrumentation Engineers (SPIE) Conference Series; Oschmann, J.M., Jr., Clampin, M.C., MacEwen, H.A., Eds.; SPIE: Bellingham, WA, USA, 2010; Volume 7731, p. 773117. [CrossRef]
6. Howell, S.B.; Sobeck, C.; Haas, M.; Still, M.; Barclay, T.; Mullally, F.; Troeltzsch, J.; Aigrain, S.; Bryson, S.T.; Caldwell, D.; et al. The K2 Mission: Characterization and Early Results. *Publ. Astron. Soc. Pac.* **2014**, *126*, 398. [CrossRef]
7. Ricker, G.R.; Latham, D.W.; Vanderspek, R.K.; Ennico, K.A.; Bakos, G.; Brown, T.M.; Burgasser, A.J.; Charbonneau, D.; Deming, L.D.; Doty, J.P.; et al. The Transiting Exoplanet Survey Satellite (TESS). In Proceedings of the 213th Meeting of the American Astronomical Society, Long Beach, CA, USA, 4–8 January 2009.
8. Bowman, D.M. Asteroseismology of high-mass stars: New insights of stellar interiors with space telescopes. *Front. Astron. Space Sci.* **2020**, *7*, 70. [CrossRef]
9. Emilio, M.; Andrade, L.; Janot-Pacheco, E.; Baglin, A.; Gutiérrez-Soto, J.; Suárez, J.C.; de Batz, B.; Diago, P.; Fabregat, J.; Floquet, M.; et al. Photometric variability of the Be star CoRoT-ID 102761769. *Astron. Astrophys.* **2010**, *522*, A43. [CrossRef]
10. Andrade, L.; Janot-Pacheco, E.; Emilio, M.; Frémat, Y. Photometric and spectroscopic variability of the B5IIIe star HD171219. *Eur. Phys. J. Web Conf.* **2017**, *152*, 04004. [CrossRef]
11. Eidam, J.M.; Andrade, L.; Emilio, M.; Rabello-Soares, M.C.; Pereira, A.W.; Janot-Pacheco, E.; Armstrong, J.D. Photometry and spectroscopy of massive stars observed during K2 Campaign 8. *Mon. Not. R. Astron. Soc.* **2020**, *491*, 302–312. [CrossRef]
12. Pereira, A.W.; Janot-Pacheco, E.; Emilio, M.; Andrade, L.; Armstrong, J.D.; Eidam, J.M.; Rabello-Soares, M.C.; da Silva, B.V.H.V. Characterizing B stars from Kepler/K2 Campaign 11. Optical analysis and seismic diagnostics. *Astron. Astrophys.* **2024**, *686*, A20. [CrossRef]
13. Eyer, L. et al. [Gaia Collaboration]. Gaia Data Release 2. Variable stars in the colour-absolute magnitude diagram. *Astron. Astrophys.* **2019**, *623*, A110. [CrossRef]
14. Brown, A.G.A. et al. [Gaia Collaboration]. Gaia Early Data Release 3. Summary of the contents and survey properties. *Astron. Astrophys.* **2021**, *649*, A1. [CrossRef]
15. Bailer-Jones, C.A.L.; Rybizki, J.; Fouesneau, M.; Demleitner, M.; Andrae, R. VizieR Online Data Catalog: Distances to 1.47 Billion Stars in Gaia EDR3: I/352. 2021. Available online: https://cdsarc.cds.unistra.fr/viz-bin/cat/I/352 (accessed on 27 August 2025).
16. Amôres, E.B.; Jesus, R.M.; Moitinho, A.; Arsenijevic, V.; Levenhagen, R.S.; marshall, D.J.; Kerber, L.O.; Künzel, R.; Moura, R.A. GALExtin: An alternative online tool to determine the interstellar extinction in the Milky Way. *Mon. Not. R. Astron. Soc.* **2021**, *508*, 1788–1797. [CrossRef]
17. Chen, B.Q.; Huang, Y.; Yuan, H.B.; Wang, C.; Fan, D.W.; Xiang, M.S.; Zhang, H.W.; Tian, Z.J.; Liu, X.W. Three-dimensional interstellar dust reddening maps of the Galactic plane. *Mon. Not. R. Astron. Soc.* **2019**, *483*, 4277–4289. [CrossRef]
18. Green, G.M.; Schlafly, E.; Zucker, C.; Speagle, J.S.; Finkbeiner, D. A 3D Dust Map Based on Gaia, Pan-STARRS 1, and 2MASS. *Astrophys. J.* **2019**, *887*, 93. [CrossRef]
19. Dotter, A. MESA Isochrones and Stellar Tracks (MIST) 0: Methods for the Construction of Stellar Isochrones. *Astrophys. J. Suppl. Ser.* **2016**, *222*, 8. [CrossRef]
20. Brown, A.G.A. et al. [Gaia Collaboration]. Gaia Data Release 2. Summary of the contents and survey properties. *Astron. Astrophys.* **2018**, *616*, A1. [CrossRef]
21. Casagrande, L.; VandenBerg, D.A. On the use of Gaia magnitudes and new tables of bolometric corrections. *Mon. Not. R. Astron. Soc.* **2018**, *479*, L102–L107. [CrossRef]
22. Cui, X.Q.; Zhao, Y.H.; Chu, Y.Q.; Li, G.P.; Li, Q.; Zhang, L.P.; Su, H.J.; Yao, Z.Q.; Wang, Y.N.; Xing, X.Z.; et al. The Large Sky Area Multi-Object Fiber Spectroscopic Telescope (LAMOST). *Res. Astron. Astrophys.* **2012**, *12*, 1197–1242. [CrossRef]
23. Jenkins, J.M.; Caldwell, D.A.; Chandrasekaran, H.; Twicken, J.D.; Bryson, S.T.; Quintana, E.V.; Clarke, B.D.; Li, J.; Allen, C.; Tenenbaum, P.; et al. Initial Characteristics of Kepler Long Cadence Data for Detecting Transiting Planets. *Astrophys. J. Lett.* **2010**, *713*, L120–L125. [CrossRef]

24. Clarke, B.D.; Caldwell, D.A.; Quintana, E.V.; Chandrasekaran, H.; Twicken, J.D.; Jenkins, J.M.; Cote, M.T.; McCauliff, S.D.; Klaus, T.C.; Allen, C.; et al. Pixel Level Calibrations. In *Kepler Data Processing Handbook*; KSCI-19081-002; NASA Ames Research Center: Moffett Field, CA, USA, 2017; Chapter 3. Available online: https://archive.stsci.edu/kepler/manuals/KSCI-19081-002-KDPH.pdf (accessed on 27 August 2025).
25. Smith, J.C.; Stumpe, M.C.; Jenkins, J.M.; Van Cleve, J.E.; Girouard, F.R.; Kolodziejczak, J.J.; McCauliff, S.D.; Morris, R.L.; Twicken, J.D. Presearch Data Conditioning. In *Kepler Data Processing Handbook*; KSCI-19081-002; NASA Ames Research Center: Moffett Field, CA, USA, 2017; Chapter 7. Available online: https://archive.stsci.edu/kepler/manuals/KSCI-19081-002-KDPH.pdf (accessed on 27 August 2025).
26. Aigrain, S.; Parviainen, H.; Pope, B.J.S. K2SC: Flexible systematics correction and detrending of K2 light curves using Gaussian process regression. *Mon. Not. R. Astron. Soc.* **2016**, *459*, 2408–2419. [CrossRef]
27. Foster, G. The cleanest Fourier spectrum. *Astron. J.* **1995**, *109*, 1889–1902. [CrossRef]
28. Degroote, P.; Briquet, M.; Catala, C.; Uytterhoeven, K.; Lefever, K.; Morel, T.; Aerts, C.; Carrier, F.; Auvergne, M.; Baglin, A.; et al. Evidence for nonlinear resonant mode coupling in the β Cephei star HD 180642 (V1449 Aquilae) from CoRoT photometry. *Astron. Astrophys.* **2009**, *506*, 111–123. [CrossRef]
29. Baran, A.S.; Koen, C.; Pokrzywka, B. A detection threshold in the amplitude spectra calculated from Kepler data obtained during K2 mission. *Mon. Not. R. Astron. Soc.* **2015**, *448*, L16–L19. [CrossRef]
30. Lee, G.; Gommers, R.; Waselewski, F.; Wohlfahrt, K.; O'Leary, A. PyWavelets: A Python package for wavelet analysis. *J. Open Source Softw.* **2019**, *4*, 1237. [CrossRef]
31. Tody, D. The IRAF Data Reduction and Analysis System. In Proceedings of the Instrumentation in Astronomy VI, Tucson, AZ, USA, 2–8 March 1986 ; Crawford, D.L., Ed.; Society of Photo-Optical Instrumentation Engineers (SPIE) Conference Series; Volume 627, p. 733. [CrossRef]
32. Valenti, J.A.; Piskunov, N. Spectroscopy made easy: A new tool for fitting observations with synthetic spectra. *Astron. Astrophys. Suppl. Ser.* **1996**, *118*, 595–603. [CrossRef]
33. Castelli, F. ATLAS12: How to use it. *Mem. Della Soc. Astron. Ital. Suppl.* **2005**, *8*, 25.
34. Heiter, U.; Barklem, P.; Fossati, L.; Kildiyarova, R.; Kochukhov, O.; Kupka, F.; Obbrugger, M.; Piskunov, N.; Plez, B.; Ryabchikova, T.; et al. VALD — An atomic and molecular database for astrophysics. *J. Phys. Conf. Ser.* **2008**, *130*, 012011. [CrossRef]
35. Simón-Díaz, S.; Godart, M.; Castro, N.; Herrero, A.; Aerts, C.; Puls, J.; Telting, J.; Grassitelli, L. The IACOB project. III. New observational clues to understand macroturbulent broadening in massive O- and B-type stars. *Astron. Astrophys.* **2017**, *597*, A22. [CrossRef]
36. Paxton, B.; Bildsten, L.; Dotter, A.; Herwig, F.; Lesaffre, P.; Timmes, F. Modules for Experiments in Stellar Astrophysics (MESA). *Astrophys. J. Suppl. Ser.* **2011**, *192*, 3. [CrossRef]
37. Iglesias, C.A.; Rogers, F.J. Radiative Opacities for Carbon- and Oxygen-rich Mixtures. *Astrophys. J.* **1993**, *412*, 752. [CrossRef]
38. Balona, L.A.; Pigulski, A.; De Cat, P.; Handler, G.; Gutiérrez-Soto, J.; Engelbrecht, C.A.; Frescura, F.; Briquet, M.; Cuypers, J.; Daszyńska-Daszkiewicz, J.; et al. Kepler observations of the variability in B-type stars. *Mon. Not. R. Astron. Soc.* **2011**, *413*, 2403–2420. [CrossRef]
39. McNamara, B.J.; Jackiewicz, J.; McKeever, J. The Classification of Kepler B-star Variables. *Astron. J.* **2012**, *143*, 101. [CrossRef]
40. Samus', N.N.; Kazarovets, E.V.; Durlevich, O.V.; Kireeva, N.N.; Pastukhova, E.N. General catalogue of variable stars: Version GCVS 5.1. *Astron. Rep.* **2017**, *61*, 80–88. [CrossRef]
41. Waelkens, C. Slowly pulsating B stars. *Astron. Astrophys.* **1991**, *246*, 453–468. [CrossRef]
42. Miglio, A.; Montalbán, J.; Noels, A.; Eggenberger, P. Probing the properties of convective cores through g modes: High-order g modes in SPB and γ Doradus stars. *Mon. Not. R. Astron. Soc.* **2008**, *386*, 1487–1502. [CrossRef]
43. Moravveji, E.; Aerts, C.; Pápics, P.I.; Triana, S.A.; Vandoren, B. Tight asteroseismic constraints on core overshooting and diffusive mixing in the slowly rotating pulsating B8.3V star KIC 10526294. *Astron. Astrophys.* **2015**, *580*, A27. [CrossRef]
44. Pedersen; Aerts, C..; Pápics, P. I..; Rogers, T. M.. The shape of convective core overshooting from gravity-mode period spacings. *Astron. Astrophys.* **2018**, *614*, A128. [CrossRef]
45. Wu, T.; Li, Y.; Deng, Z.m. A New C-D-like Diagram for SPB Stars: The Variations of Period Spacing as a Signature of Evolutionary Status. *Astrophys. J.* **2018**, *867*, 47. [CrossRef]
46. Wu, T.; Li, Y. High-precision Asteroseismology in a Slowly Pulsating B Star: HD 50230. *Astrophys. J.* **2019**, *881*, 86. [CrossRef]
47. Wu, T.; Li, Y.; Deng, Z.m.; Lin, G.f.; Song, H.f.; Jiang, C. Asteroseismic Analyses of Slowly Pulsating B Star KIC 8324482: Ultraweak Element Mixing beyond the Central Convective Core. *Astrophys. J.* **2020**, *899*, 38. [CrossRef]
48. Rivinius, T.; Carciofi, A.C.; martayan, C. Classical Be stars. Rapidly rotating B stars with viscous Keplerian decretion disks. *Astron. Astrophys. Rev.* **2013**, *21*, 69. [CrossRef]
49. Kiriakidis, M.; El Eid, M.F.; Glatzel, W. Heavy element opacities and the pulsations of beta cepheid stars. *Mon. Not. R. Astron. Soc.* **1992**, *255*, 1P–5P. [CrossRef]

50. Dziembowski, W.A.; Moskalik, P.; Pamyatnykh, A.A. The opacity mechanism in B-type stars - II. Excitation of high-order g-modes in main-sequence stars. *Mon. Not. R. Astron. Soc.* **1993**, *265*, 588–600. [CrossRef]
51. De Cat, P. Observational Asteroseismology of slowly pulsating B stars. *Commun. Asteroseismol.* **2007**, *150*, 167. [CrossRef]
52. Degroote, P.; Acke, B.; Samadi, R.; Aerts, C.; Kurtz, D.W.; Noels, A.; Miglio, A.; Montalbán, J.; Bloemen, S.; Baglin, A.; et al. CoRoT's view on variable B8/9 stars: Spots versus pulsations. Evidence for differential rotation in HD 174648. *Astron. Astrophys.* **2011**, *536*, A82. [CrossRef]
53. Pápics, P.I.; Moravveji, E.; Aerts, C.; Tkachenko, A.; Triana, S.A.; Bloemen, S.; Southworth, J. KIC 10526294: A slowly rotating B star with rotationally split, quasi-equally spaced gravity modes. *Astron. Astrophys.* **2014**, *570*, A8. [CrossRef]
54. Pápics, P.I.; Tkachenko, A.; Aerts, C.; Van Reeth, T.; De Smedt, K.; Hillen, M.; Østensen, R.; Moravveji, E. Asteroseismic Fingerprints of Rotation and Mixing in the Slowly Pulsating B8 V Star KIC 7760680. *Astrophys. J. Lett.* **2015**, *803*, L25. [CrossRef]
55. Pápics, P.I.; Tkachenko, A.; Van Reeth, T.; Aerts, C.; Moravveji, E.; Van de Sande, M.; De Smedt, K.; Bloemen, S.; Southworth, J.; Debosscher, J.; et al. Signatures of internal rotation discovered in the Kepler data of five slowly pulsating B stars. *Astron. Astrophys.* **2017**, *598*, A74. [CrossRef]
56. Pedersen, M.G.; Aerts, C.; Pápics, P.I.; Michielsen, M.; Gebruers, S.; Rogers, T.M.; Molenberghs, G.; Burssens, S.; Garcia, S.; Bowman, D.M. Internal mixing of rotating stars inferred from dipole gravity modes. *Nat. Astron.* **2021**, *5*, 715–722. [CrossRef]
57. Kilkenny, D.; O'Donoghue, D.; Koen, C.; Stobie, R.S.; Chen, A. The Edinburgh-Cape Blue Object Survey—II. Zone 1—The North Galactic CAP. *Mon. Not. R. Astron. Soc.* **1997**, *287*, 867–893. [CrossRef]
58. Stankov, A.; Handler, G. Catalog of Galactic β Cephei Stars. *Astrophys. J. Suppl. Ser.* **2005**, *158*, 193–216. [CrossRef]
59. Lesh, J.R.; Aizenman, M.L. The observational status of the beta Cephei stars. *Annu. Rev. Astron. Astrophys.* **1978**, *16*, 215. [CrossRef]
60. LeBlanc, F. *An Introduction to Stellar Astrophysics*; John Wiley & Sons: Hoboken, NJ, USA, 2010.
61. Chapellier, E.; Le Contel, D.; Le Contel, J.M.; Mathias, P.; Valtier, J.C. A hybrid β Cephei-SPB star in a binary system: γ Pegasi. *Astron. Astrophys.* **2006**, *448*, 697–701. [CrossRef]
62. De Cat, P.; Briquet, M.; Aerts, C.; Goossens, K.; Saesen, S.; Cuypers, J.; Yakut, K.; Scuflaire, R.; Dupret, M.A.; Uytterhoeven, K.; et al. Long term photometric monitoring with the Mercator telescope. Frequencies and mode identification of variable O-B stars. *Astron. Astrophys.* **2007**, *463*, 243–249. [CrossRef]
63. Pamyatnykh, A.A. Pulsational Instability Domains in the Upper Main Sequence. *Acta Astron.* **1999**, *49*, 119–148.
64. Houk, N.; Swift, C. *Michigan Catalogue of Two-Dimensional Spectral Types for the HD Stars*; Department of Astronomy, University of Michigan: Ann Arbor, MI, USA, 1999; Volume 5.
65. Blomme, R.; Mahy, L.; Catala, C.; Cuypers, J.; Gosset, E.; Godart, M.; Montalban, J.; Ventura, P.; Rauw, G.; Morel, T.; et al. Variability in the CoRoT photometry of three hot O-type stars. HD 46223, HD 46150, and HD 46966. *Astron. Astrophys.* **2011**, *533*, A4. [CrossRef]
66. Bowman, D.M.; Aerts, C.; Johnston, C.; Pedersen, M.G.; Rogers, T.M.; Edelmann, P.V.F.; Simón-Díaz, S.; Van Reeth, T.; Buysschaert, B.; Tkachenko, A.; et al. Photometric detection of internal gravity waves in upper main-sequence stars. I. Methodology and application to CoRoT targets. *Astron. Astrophys.* **2019**, *621*, A135. [CrossRef]
67. Rogers, T.M.; Lin, D.N.C.; McElwaine, J.N.; Lau, H.H.B. Internal Gravity Waves in Massive Stars: Angular Momentum Transport. *Astrophys. J.* **2013**, *772*, 21. [CrossRef]
68. Cantiello, M.; Langer, N.; Brott, I.; de Koter, A.; Shore, S.N.; Vink, J.S.; Voegler, A.; Lennon, D.J.; Yoon, S.C. Sub-surface convection zones in hot massive stars and their observable consequences. *Astron. Astrophys.* **2009**, *499*, 279–290. [CrossRef]
69. Struve, O. Some Unusual Short-period Variables. *Sky Telesc.* **1955**, *14*, 461.
70. Struve, O.; Sahade, J.; Lynds, C.R.; Huang, S.S. On the Spectrum and Brightness of Maia (20 C Tauri). *Astrophys. J.* **1957**, *125*, 115. [CrossRef]
71. McNamara, B.J. Maia variables and upper-main-sequence phenomena. *Astrophys. J.* **1985**, *289*, 213–219. [CrossRef]
72. Aerts, C.; Kolenberg, K. HD 121190: A cool multiperiodic slowly pulsating B star with moderate rotation. *Astron. Astrophys.* **2005**, *431*, 615–622. [CrossRef]
73. Townsend, R.H.D. A semi-analytical formula for the light variations due to low-frequency g modes in rotating stars. *Mon. Not. R. Astron. Soc.* **2003**, *343*, 125–136. [CrossRef]
74. Savonije, G.J. Unstable quasi g-modes in rotating main-sequence stars. *Astron. Astrophys.* **2005**, *443*, 557–570. [CrossRef]
75. White, T.R.; Pope, B.J.S.; Antoci, V.; Pápics, P.I.; Aerts, C.; Gies, D.R.; Gordon, K.; Huber, D.; Schaefer, G.H.; Aigrain, S.; et al. Beyond the Kepler/K2 bright limit: Variability in the seven brightest members of the Pleiades. *Mon. Not. R. Astron. Soc.* **2017**, *471*, 2882–2901. [CrossRef]
76. Monier, R. The Rapid Far-ultraviolet Variability of Maia Recorded by IUE. *Res. Notes AAS* **2021**, *5*, 81. [CrossRef]
77. Degroote, P.; Aerts, C.; Ollivier, M.; Miglio, A.; Debosscher, J.; Cuypers, J.; Briquet, M.; Montalbán, J.; Thoul, A.; Noels, A.; et al. CoRoT's view of newly discovered B-star pulsators: Results for 358 candidate B pulsators from the initial run's exoplanet field data. *Astron. Astrophys.* **2009**, *506*, 471–489. [CrossRef]

78. Mowlavi, N.; Barblan, F.; Saesen, S.; Eyer, L. Stellar variability in open clusters. I. A new class of variable stars in NGC 3766. *Astron. Astrophys.* **2013**, *554*, A108. [CrossRef]
79. Mowlavi, N.; Saesen, S.; Semaan, T.; Eggenberger, P.; Barblan, F.; Eyer, L.; Ekström, S.; Georgy, C. Stellar variability in open clusters . II. Discovery of a new period-luminosity relation in a class of fast-rotating pulsating stars in NGC 3766. *Astron. Astrophys.* **2016**, *595*, L1. [CrossRef]
80. Balona, L.A. Maia variables and other anomalies among pulsating stars. *arXiv* **2023**, arXiv:2301.09280. [CrossRef]
81. Balona, L.A.; Baran, A.S.; Daszyńska-Daszkiewicz, J.; De Cat, P. Analysis of Kepler B stars: Rotational modulation and Maia variables. *Mon. Not. R. Astron. Soc.* **2015**, *451*, 1445–1459. [CrossRef]
82. Balona, L.A.; Ozuyar, D. Pulsation among TESS A and B stars and the Maia variables. *Mon. Not. R. Astron. Soc.* **2020**, *493*, 5871–5879. [CrossRef]
83. De Ridder, J. et al. [Gaia Collaboration]. Gaia Data Release 3. Pulsations in main sequence OBAF-type stars. *Astron. Astrophys.* **2023**, *674*, A36. [CrossRef]
84. Southworth, J.; Bowman, D.M.; Tkachenko, A.; Pavlovski, K. Discovery of β Cep pulsations in the eclipsing binary V453 Cygni. *Mon. Not. R. Astron. Soc.* **2020**, *497*, L19–L23. [CrossRef]
85. Pedersen, M.G.; Chowdhury, S.; Johnston, C.; Bowman, D.M.; Aerts, C.; Handler, G.; De Cat, P.; Neiner, C.; David-Uraz, A.; Buzasi, D.; et al. Diverse Variability of O and B Stars Revealed from 2-minute Cadence Light Curves in Sectors 1 and 2 of the TESS Mission: Selection of an Asteroseismic Sample. *Astrophys. J. Lett.* **2019**, *872*, L9. [CrossRef]
86. Bowman, D.M.; Burssens, S.; Pedersen, M.G.; Johnston, C.; Aerts, C.; Buysschaert, B.; Michielsen, M.; Tkachenko, A.; Rogers, T.M.; Edelmann, P.V.F.; et al. Low-frequency gravity waves in blue supergiants revealed by high-precision space photometry. *Nat. Astron.* **2019**, *3*, 760–765. [CrossRef]
87. Burssens, S.; Simón-Díaz, S.; Bowman, D.M.; Holgado, G.; Michielsen, M.; de Burgos, A.; Castro, N.; Barbá, R.H.; Aerts, C. Variability of OB stars from TESS southern Sectors 1-13 and high-resolution IACOB and OWN spectroscopy. *Astron. Astrophys.* **2020**, *639*, A81. [CrossRef]
88. Miglio, A.; Montalbán, J.; Dupret, M.A. Revised instability domains of SPB and β Cephei stars. *Commun. Asteroseismol.* **2007**, *151*, 48–56. [CrossRef]
89. Silva, B.V.H.V. Estudo de estrelas B do campo 13 da missão Kepler K2. Ph.D. Thesis, State University of Ponta Grossa, Ponta Grossa, PR, Brazil, 2023. Available online: http://tede2.uepg.br/jspui/handle/prefix/4066 (accessed on 27 August 2025).
90. Eidam, J.M. Estrelas A e B de Campanhas da Missão Kepler K2 [A and B Stars from Kepler K2 Mission Campaigns]. Ph.D. Thesis, National Observatory (Observatório Nacional), Rio de Janeiro, Brazil, 19 September 2024; p. 181. Available online: https://sucupira-legado.capes.gov.br/sucupira/public/consultas/coleta/trabalhoConclusao/viewTrabalhoConclusao.jsf?popup=true&id_trabalho=16095795 (accessed on 27 August 2025).

Disclaimer/Publisher's Note: The statements, opinions and data contained in all publications are solely those of the individual author(s) and contributor(s) and not of MDPI and/or the editor(s). MDPI and/or the editor(s) disclaim responsibility for any injury to people or property resulting from any ideas, methods, instructions or products referred to in the content.